RADIOMETRIC STUDY OF BEACH SAND DEPOSITS ALONG THE COAST OF WESTERN CAPE PROVINCE, SOUTH AFRICA

Nkanyiso Bongumusa Mbatha

A thesis submitted in partial fulfilment of the requirements for the degree of Master of Science at the University of the Western Cape.

Supervisor: Dr. Atulya Kumar Mohanty
Environmental Radioactivity Laboratory
iThemba LABS

Co-supervisor: Prof. Robert Lindsay
Department of Physics
University of the Western Cape

January 2007

DECLARATION

I, Nkanyiso Bongumusa Mbatha the undersigned, hereby declare that the work contained in this thesis is my own original work and that I have not previously in its entirety or in part submitted it at any university for a degree.

Signature: ……

Date: ……...

Radiometric study of Beach Sand Deposits along the Coast of Western Cape Province, South Africa

Keywords

Natural radioactivity

Gamma-ray spectrometry

Radionuclides

Provenance investigation

Beach sand

Uranium fixation

West Coast

Activity concentration

Grain-size

Heavy minerals

Radiometric study of Beach Sand Deposits along the Coast of Western Cape Province, South Africa

Nkanyiso Bongumusa Mbatha

Dept. of Physics, University of the Western Cape, Private Bag X 17, Bellville, 7537, South Africa

ABSTRACT

Natural radioactivity studies have been carried out to study the textural characteristics, heavy mineral composition, provenance, sediment transport, and depositional environment of beach placer deposits. The naturally occurring radionuclides such as ^{232}Th, ^{238}U and ^{40}K are used as the tracers of the mineralogical properties of beach sands, which reflect the geological characteristics such as transport and sorting processes and the depositional environment. The present work focuses on the radiometric characteristics of beach sand deposits along the west coast of South Africa. Beach sands samples were collected at the Melkbosstrand (MBS) and Ouskip (OSK) beach. The activity concentrations of these radionuclides were determined by high-resolution gamma-ray spectrometry using a high-purity germanium (HPGe) detector in a low-background configuration.

Results shows higher levels of thorium and uranium and smaller ^{40}K concentrations found in Melkbosstrand (MBS) as compared to the Ouskip (OSK) beach. The higher levels of ^{232}Th and ^{238}U are due more heavy minerals present in the MBS beach as compared to the OSK beach. The higher level of ^{40}K concentrations observed in the OSK group shows more enrichment of lighter minerals such as potash feldspars and quartz sands. Based on the ^{40}K concentrations in the two beach zones, it can be inferred that the sand particles were derived from sedimentary provinces. The sedimentary provinces such as Cape Supergroup and the Table Mountain Group, occurring in close proximity to the West Coast, are the possible sources for these mineral sands. The above results show the strong evidence of sediments being originally derived from sedimentary and metasedimentary rocks. The radiometric analysis of grain size fractions shows that the ^{40}K content varies only slightly with the grain size fractions, while ^{232}Th increases with the decrease in grain size. Based on the cross plot of eTh/eU versus eTh/K, it is inferred that the sand samples were deposited

in a fixed uranium environment and an oxidizing environment. The OSK group falls under micas and feldspars, while the MBS group of samples falls under clay mineral groups. A high eTh/K ratio in the MBS beach sand samples signifies the presence of more heavy minerals and lesser lighter particles such as K-bearing feldspars and quartzes as compared to the OSK beach samples.

ACKNOWLEDGEMENTS

I am greatly indebted to the following for the role they played in making this thesis and my academic career possible:

- **Dr. Atulya K. Mohanty**[a]**,** supervisor, for guidance and support throughout the duration of this project. I wish that you will continue be a good and very friendly supervisor to your future students.
- **Prof. Robbie Lindsay**[b]**,** co-supervisor, for guidance and support throughout the duration of this project.
- **Dr. Richard T. Newman**[a]**,** for guidance, suggestions and support during the course of this investigation.
- **Prof. Rob J. de Meijer**[c]**,** for his suggestions during sampling, sample analyses and techniques used to achieve the hypothesis of this study. And I would like to thank him for always accommodating me on his very limited time.
- the Environmental Radioactivity Laboratory (ERL) group; **Israel Hlatshwayo, Nolasco Mlwilo, S. Talha** and **R.F. Manavhela,** for always supporting and giving me useful ideas though out the study period.
- the National Research Foundation for their financial support.
- **Prof. A. Rozendaal**, and **Mr. Stefan Kruger**, Department of Geology, University of Stellenbosch for their kind help in the grain size analyses.

This work is specifically dedicated to my family, **Mbatha** (Manyosi), **Ntombela** (Mpangazitha), **Mdluli** (S'khandzisa), **Ngubane** (Somahhashi) and **Lesala**. Nonke niyisibani kimi, futhi ngiyanithanda kakhulu. Lena imiphumela yokungesekela kwenu kuyoyonke impilo yami, ngakhoke lomsebenzi ungowenu. Ukuba ngiyazenzela ngabe lomsebenzi nguwubhale nangolimi lwesiZulu, ukuze nesinedolo sikwazi ukuwufunda. Ngibonga noMvelinqangi ngongigada nokungesekela kuyoyonke lempilo yalapha emhlabeni engelula nenzeneze. Ngiyabonga.

Nkanyiso Bongumusa Mbatha (Manyosi), January, 2007

---

[a]*iThemba LABS*
[b]*University of the Western Cape*
[c]*Stichting EARTH, 9321 XS Peize, The Netherlands*

CONTENTS

LIST OF FIGURES

LIST OF TABLES

CHAPTER 1

INTRODUCTION

Naturally occurring radionuclides of terrestrial origin were present in the earth's crust since its origin. These naturally occurring radionuclides are namely ^{232}Th, ^{238}U and ^{40}K, and are mainly found in minerals, rocks and soils. Natural radionuclide parents have sufficiently long half-lives that they have persisted since their creation and their half-lives are at least comparable to the age of the earth. The origin and distribution of naturally occurring radionuclides depend on the distribution of rocks from which they originate and the geological processes which concentrate them.

In general, beach sands are weathering-resistant remainders of geological formations, transported by rivers, wind and glaciers to the coast, and deposited on the beaches by action of waves and coastal currents. These weathered materials derived from continental rocks of mostly volcanic, plutonic, metamorphic and sedimentary origin, have a broad compositional range. Their concentration depends on the hydrodynamic conditions like sediment influx from the hinterland, wave energy and its velocity, longshore current and wind speed, which control the littoral transport, sorting and deposition of placer minerals in suitable locales. Consequently, mineralogical properties of beach sand reflect the geological history of the original rock. Sand particles have a diameter that varies between 0.063 and 2.000 mm, and mineral sands are divided into light and heavy mineral (> 2.89 g.cm^{-3}) fractions based on their density. Beach sand deposits are the main source of minerals like monazite, zircon, ilmenite, rutile, garnet and sillimanite.

In beach sand deposits, heavy mineral sands constitute an important source of the radioactive elements (^{232}Th, ^{238}U and ^{40}K) and others like Rare Earth Elements,

Y, Zr, Hf and Ti. Several studies have shown that heavy mineral sand tends to have higher concentrations of naturally occurring radionuclides of the uranium and thorium decay series in their crystal structure. For minerals such as monazite, thorium content varies from grain to grain, depending on the condition of the geological environment in which it forms.

Light minerals such as quartz and feldspars are low in uranium and thorium concentrations. Overall, naturally occurring radionuclides constitute the bulk of natural radioactivity in the environment, which is the major source of background radiation we experience throughout our lives. These radionuclides radiate terrestrial radiation. Some of these naturally accruing radionuclides (^{232}Th and ^{238}U) have long transition series and are long half-lived parents which control the decays of the daughters all of which have shorter half-lives. A non-series naturally occurring radionuclide is ^{40}K, because it decays directly to stable daughters (^{40}Ar or ^{40}C a). Potassium (^{40}K) is very import for radiation protection studies because of its presence in the environment media and the contribution it makes to human exposure.

This study presents a method in which the gamma-ray spectroscopy is used to measure the activity concentration of naturally occurring radionuclides in beach sands collected from two beach zones (Melkbosstrand and Ouskip beach) located along the west coast of Western Cape Province, South Africa. This technique can be broadly applied to sedimentological studies of e.g. texture and mineralogy, provenance, sediment transport history studies and characteristics of depositional environments for the beach sediments based on the correlation between ^{232}Th, ^{238}U, ^{40}K activity concentrations and Th/U and Th/K ratios.

1.1 Overview of the study

Several natural radioactivity studies have been carried out on beach placer deposits to study the textural characteristics, heavy mineral composition, provenance, sediment transportation, deposition environment, mineral distribution, delineation of new placer deposits, qualitative and quantitative assessment of heavy minerals (De Meijer et al., 1997; De Meijer, 1998; Jones et al., 2001; Asadov et al., 2001 and Anjos et al., 2006). These studies employ naturally occurring (^{232}Th, ^{238}U and ^{40}K) as tracers

of the mineralogical properties of beach sands, which indicates geological characteristics such as the transport and sorting processes (Anjos et al., 2006).

A method called radiometric fingerprinting was proven to be very useful in studying provenance of beach placer deposits. De Meijer (De Meijer et al., 1990) first demonstrated this method for the sand samples collected from beach and dunes of the North Sea Coast in the Netherlands. A sample was separated into heavy and light fractions using the heavy liquid (bromoform) method. Specific activity concentrations of each fraction were determined using gamma-ray spectroscopy. The results then were used as a calibration for a radiometric method to determine the heavy-mineral mass percentage (α). For each sample the radiometric value of α, α_{rad}, follows from a linear interpolation of the measured activity concentration (A), between values for the specific activity of light and heavy-mineral fraction, A_L and A_H respectively (De Meijer et al., 1995).

$$A = \alpha A_H + (1-\alpha) A_L . \qquad (1.1)$$

With the results obtained, it was concluded that the origin (provenance) of beach sands can be determined from the radiometric fingerprint of two suites of minerals in the sand.

According to Kogan (Kogan et al., 1969), radioactive potassium ^{40}K is uniformly spread throughout the principal rock-forming minerals, such as quartz and feldspar, as well as in accessory heavy minerals. These quartz and feldspars are light minerals that usually form the bulk of sand deposits. Therefore, potassium (^{40}K) activity of sands having the same origin (parent rock) should have equal concentration regardless of their mineralogical composition. Thus, potassium concentration provides a kind of radioactive reference, which reflects the source of the parent rocks such as granitic or basaltic rocks. The distribution of potassium concentrations in beach placers can be used as an important tool for the correlation of the provenance and the geological terrain from which it derives and the source rock characteristics.

It is well known that in the parent materials for siliclastic sediments, a significant part of radioactive uranium and thorium are bound in dark-coloured,

ferromagnesian minerals (Kogan et al., 1969). This typically occurs as small highly brittle particles, and when source rocks disintegrate through weathering and erosion, they are released to accumulate as the dark coloured population in sands and other fine-grained deposits (Kogan et al., 1969). The dark coloured minerals possess higher (by 20-100%) specific weight than the rock-forming minerals (such as quartz and feldspars) and are known as heavy minerals, whose specific gravity is greater than 2.89 $g.cm^3$. Consequently, the transport of these heavy minerals is affected by gravitational separation during the process of deposition in the beach environment. This implies that the concentration of radionuclides of the sands should be a function of grain size and density. Since wave and current activity separates grains according to size, shape and density (Komar, 1998), there should be corresponding distinguishable levels of radionuclide by the γ-ray activities. This being so, γ-ray spectrometry could be potentially very sensitive to any changes in size or density of sand grains as function of distance from source or substrate depth. So, the γ-ray technique can be broadly applied to sedimetological studies such as textural, mineralogical, provenance investigations, transport history and depositional environments based on the concentrations of ^{232}Th, ^{238}U, ^{40}K and Th/U and Th/K ratios in sediments.

The thorium-to-uranium ratio has also proved to be useful in the recognition of "geochemical facies" (Macfarlane et al., 1989). Based on the analyses of numerous rock samples Adams and Weaver (1958) demonstrated the usefulness of the thorium to uranium ratio as an indicator of relatively oxidizing or reducing conditions. Thorium is unaffected by the redox conditions and remains insoluble as Th^{4+}. Uranium, however, exists as insoluble U^{4+} under highly reducing conditions, which leads to U enrichment in sediments, where it exists as soluble U^{6+} under oxidizing conditions, leading to U loss from sediments. The eTh/eU ratios[1], therefore, vary from 0 – 2 in anoxic environments to 7 in a strongly oxidizing environment. Thus, the eTh/eU ratio can be used as a proxy for the redox conditions of the depositional environment, suggesting that a relationship with mean sea level may exist. Following Adams and Weaver (Adams and Weaver, 1958), when the ratio was computed to be

[1] eTh and eU represents ^{232}Th and ^{238}U expressed in parts per million , so that the specific parent activity of a sample containing 1 ppm of ^{232}Th and 1 ppm of natural U is 4.08 Bq/kg and 12.3 Bq/kg, respectively.

less than 2, the depositional environment of sediments had promoted uranium fixation under probable reducing conditions, and was most commonly marine. By contrast, the ratio values greater than seven implied uranium mobilization through weathering and/or leaching, and therefore indicated an oxidizing, possibly terrestrial environment (Anjos et al., 2006).

An example is the cross plot of eTh/eU and eTh/K (Figure 1.1), which summarizes the compositional changes related to potassium as well as implication concerning the redox potential (adapted from Anjos et al., 2006). In this figure, data from sand samples collected from 35 sites in the Brazilian southeast coast are represented. Using this diagram Anjos (Anjos et al., 2006) was able to confirm the main features of the geological mapping of coastal deposits, showing that the gamma-ray spectroscopy can be used as a tool in the understanding of the origin and transport of sediments (Anjos et al., 2006). And it also proves that eTh/eU ratios are useful when used as a proxy for redox condition of the depositional environment.

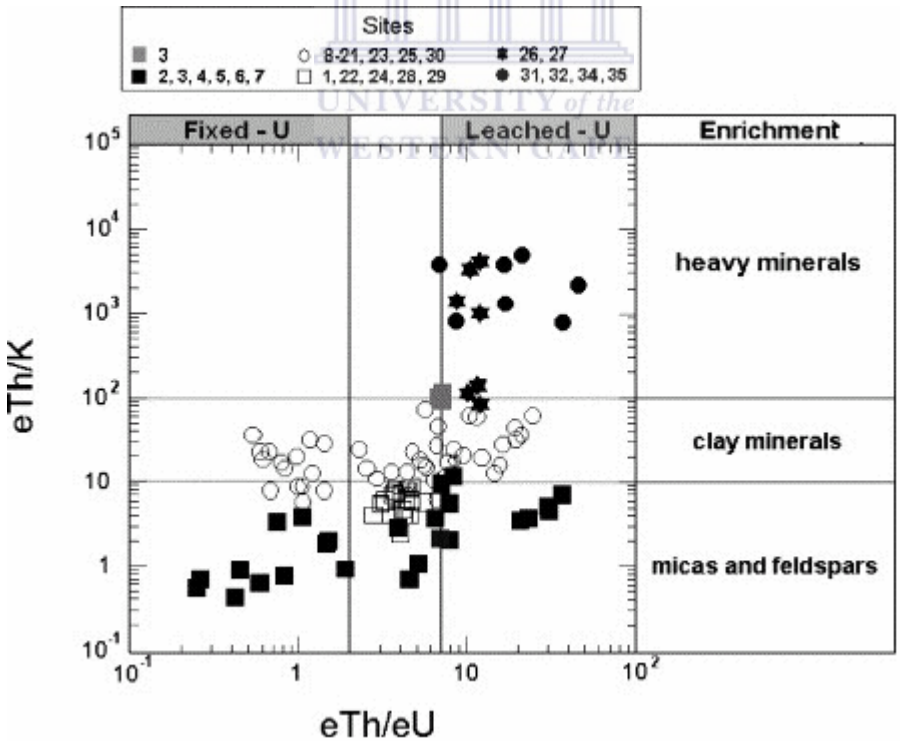

Figure 1.1: Figure showing the cross plot of eTh/eU and eTh/K (adapted from Anjos et al., 2006).

1.2 Previous beach sands investigations along the West Coast of South Africa

The coastline of South Africa is endowed with a number of multi-mineral placer deposits of beach and dune sands origin. The heavy mineral placer deposits along the west coast were first reported by Haughton (Haughton, 1931) and followed by the Geological Survey of South Africa (Coetzee 1957 and Toerien and Groeneveld, 1957). A major exploration program by Anglo American Corporation, initially for monazites, but later also titanium-bearing coastal beach and dune sands, located major recourses during the period 1985-1990 (Macdonald et al., 1997). Heavy minerals are widely distributed along the entire west coast, and relatively low concentrations to higher concentrations are found at the Namaqualand coast and are mainly concentrated in Mesozoic fluvial, Cenozoic marine and recent Aeolian unconsolidated placers (Macdonald et al., 1997). The light fractions such as quartz and potash feldspar and heavy mineral fractions are deposited by fluvial, marine and Aeolian processes along the entire coast. The heavy mineral fraction consists of garnet (locally up to 40%), clinopyroxene, magnetite, amphibole, tourmaline, spinel, kyanite, epidote and chromite as non-economic minerals. The economic fraction consists of ilmenite, and their alteration products such as hydrated ilmenite, pseudo-rutile and leucoxene and minor amounts of zircon, rutile and traces of monazite (Macdonald and Rozendaal 1995; Macdonald et al., 1997).

Radiometric techniques were used to study the radiometric characteristics of heavy mineral deposits and the provenance of mineral sands which were derived from different geological terrains along the West Coast of South Africa by Macdonald (Macdonald et al., 1997). Along the Western Cape coast, mineralogy of the hinterland is modified by the effects of rivers and ocean currents (De Meijer, 1998). Figure 1.2 shows an example of a radiometric study in the Western Coast of South Africa which was carried out by De Meijer (De Meijer, 1998). This figure shows ^{214}Bi activity concentrations in the heavy-mineral fraction of the samples. It shows that ^{214}Bi activity concentration values vary over almost two orders of magnitude for this stretch of the coast. De Meijer (De Meijer, 1998) showed that along the smaller stretch of the western coast the variation in ^{214}B values are related to the variation in zircon content. There is a considerable variation in mineralogy and radiometric characteristics that

were discovered by Macdonald (Macdonald et al., 1997) within the region of Ouskip, Melkbosstrand and other upper regions such as Yzerfontein and Silwerstroomstrand (see Figure 1.2). These variations are due to influxes of local streams, local coastal outcrops of radionuclide-rich rocks and variations in mineral composition within the heavy-mineral suite (Macdonald et al., 1997).

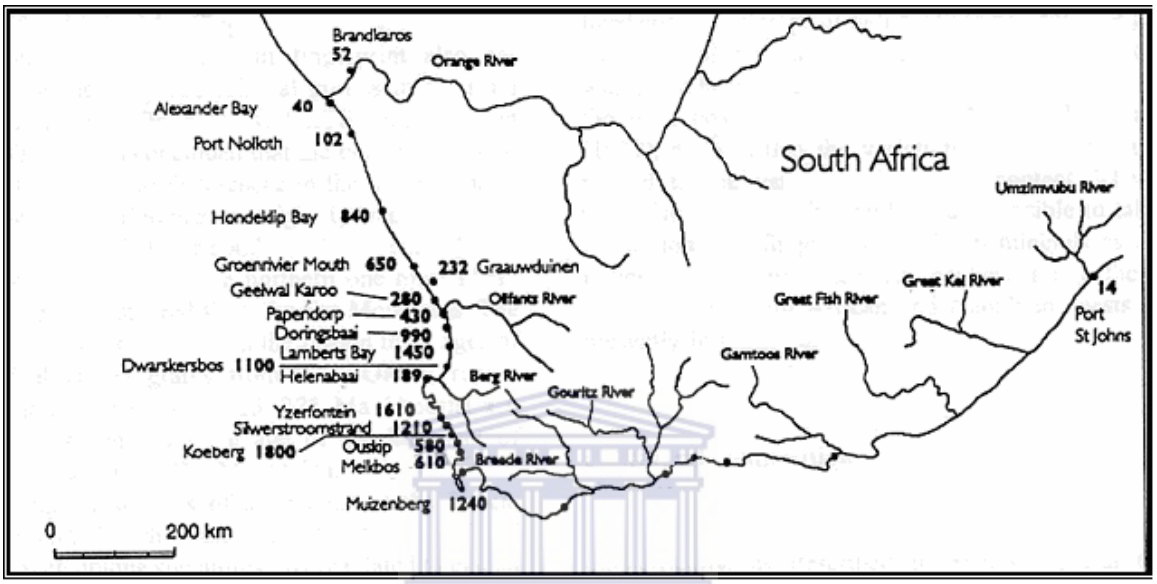

Figure 1.2: Variations of activity concentration (Bq.kg^{-1}) of ^{214}Bi in the heavy-mineral fraction of sand samples collected in Western Cape coast, South Africa (De Meijer, 1998).

Table 1.1 shows a list of radionuclide concentration results from a study of radiometric fingerprints of minerals associated with heavy minerals deposits conducted in South African (De Meijer, 1998). These results indicate a clear difference in concentrations with high ^{40}K and low ^{214}Bi and ^{232}Th values in light minerals (quartz and clay minerals) and the opposite trend for heavy minerals. Values of Bi and Th concentration in monazite are very high. With these results, De Meijer (De Meijer, 1998) indicated a clear correlation between radionuclide concentrations and a specific mineral type.

Table 1.1: Table showing the results of a study on radiometric fingerprint of minerals associated with heavy mineral deposits, conducted along the western coast of South Africa (De Meijer, 1998).

Mineral	^{40}K (Bq/kg)	^{214}Bi (Bq/kg)	^{232}Th (Bq/kg)
Quartz	116(8)	2(2)	<9
Silt/clay minerals	218(10)	49.4(1.1)	127(3)
Ferricrete	95(7)	130(3)	160(4)
Magnetite	<10	120(120)	200(200)
Ilmenite	2.8(0.5)	18(2)	27(9)
Rutile	13(3)	460(70)	<60
Zircon	<18	3280(120)	444(16)
Monazite	1600(600)	42000(2000)	181000(2000)

1.3 Objectives of the present work

The present work will investigate the radiometric characteristics of beach sand deposits (from Melkbosstrand and Ouskip beaches) along the West Coast of South Africa, in terms of radionuclide (^{232}Th, ^{238}U and ^{40}K) concentrations of mineral sands, grain-size distributions, provenance, transport and depositional history. The naturally occurring radionuclide correlations are used as tracers of the mineralogical properties of the beach placers, which reflect the sediment composition of the different coastal segments and are also used to establish its geological provenance. There is also an aim to distinguish between various fractions of sand grains on the basis of grain-size distribution and based on radionuclide concentrations from two different segments of the beach zones. In order to achieve the objectives, the following were included in the study:

- radiometric analysis of beach sands from the two beaches (in terms of ^{232}Th, ^{238}U and ^{40}K activity concentrations);
- grain-size analyses of selected sand samples, followed by the radiometric analysis of the grain-size fractions;
- investigation of the mineral proportion and the provenance of the beach placer deposits based on the correlations between concentrations of ^{232}Th, ^{238}U, ^{40}K and Th/U and Th/K ratios;
- a study of depositional environment by means of constructing a Th/K versus Th/U cross-plot in order to determine whether sediments were deposited under redox or oxidizing conditions, and to study the mineralogical associations;

1.4 Research plan

1.4.1 Location of the study area

The study areas selected for the above-mentioned study included (i) Melkbosstrand and (ii) Ouskip beach, situated along the west coast, Western Cape Province, South Africa. The beach placer deposits are in an area that forms the part of Cape Flats region along the coastal plain between Cape Town and Saldanha Bay. The area is characterized by wide, flat plains bordering the rugged, steep Atlantic coastline. At several localities, the modern beaches host significant concentrations of heavy minerals, but large, economically viable deposits are normally associated with poorly consolidated, raised marine palaeoterraces, Aeolian sands and minor fluvial sediments. These occur at different elevations that correspond to diamondiferous terraces and are linked to Miocene, Pliocene and Quaternary transgressions (Dingle et al., 1983). The Quaternary sedimentary deposits that comprise the beach sands were possibly derived from the Proterzoic meta-sediments and Silurian Table Mountain Group.

1.4.2 Sample collection and preparation

Ten samples were collected at a distance of 20 meters apart (at both beaches), along the two beach zones parallel to the shoreline, and five sets of samples were collected across (transect) the beach, from the landward side to the sea coast of the

two beach zones (from lower to upper beach). This was done in order to evaluate how the natural radionuclide concentrations vary with distance from the shoreline for each beach. The sample analyses allowed for evaluating the mean behavior of the natural radionuclides distribution for each beach zone and it also allowed evaluating the mean distribution along coastal zone.

The sand samples were subjected to washing, cleaning and drying. Each sample was separated into two parts. One part of the sample was subjected to bulk radiometric analysis. The other parts were separated into various factions using mechanical sieves for the grain size analysis and the subsequent radiometric analysis. These analyses allowed evaluating the distributions of radionuclide concentrations in coarse, medium and fine grain sediments of the beach sands. The radiometric analyses of the samples were carried out using an HPGe gamma-ray detector.

1.5 Plan of the thesis

This thesis contains five chapters. The next chapter (chapter 2) presents a review of the geological setting of the study area, sampling strategy, sample collection, sample preparation and grain-size separation of sand samples. Chapter 3 describes radiometric measurements, with the main focus on gamma-rays emitted in the decay series of ^{232}Th, ^{238}U and ^{40}K, their interaction with matter, experimental set-up and method followed. Results and discussions are presented in chapter 4. A summary and conclusion is presented in the last chapter.

CHAPTER 2

GEOLOGICAL SETTING AND SAMPLING

2.1 Introduction

The mineralogical composition of the beach placer deposits reflects characteristics of its hinterland geology. In this chapter, general geology of the hinterland area, geological setting of the study area and the location of the sampling site will be discussed. Sampling, sample preparation and grain size separation of sand samples are also discussed in this chapter.

2.2 Physiographic setting

The two beach zones selected for the present study are Melkbosstrand (MBS) and Ouskip (OSK) beach, situated approximately 25 km to the north of Cape Town, Western Province (see Figure: 2.1). MBS beach (Lat. 33º 43. 579', long. 18º26. 491') and OSK beach (Lat. 33º 42. 890', Long. 18º 26. 563') are separated by a distance of approximately 1.2 km. Both of these beaches have an average width of more than 500 meters, mostly exposed during the low tide, trending NW-SE with gentle slope towards the sea, bounded by Atlantic Ocean in the northwest and coastal plains in the southeast side. A major feature of the drainage pattern of the area is the Salt River which intersects the coast of the OSK beach and flows to the ocean.

2.3 Geology of the study area

The Palaeozoic Cape Super Group, Sillurian sandstones and quartzites of the Table Mountain Group of rocks dominate the major part of the Western Cape. The Strata of the Cape Supergroup consists of clastic metasedimentary rocks, predominantly quartzites and phyllites, most of which have undergone low grade metamorphism (De Swardt and Rowsell, 1974). The thickness of the whole Cape succession may vary up to 3300 m, although it appears to thicken considerably in the

eastern parts of the fold belt (Theron, 1992). The age of the Cape succession as inferred from its stratigraphic relationships with underlying and older rocks, interpretations of Cape sedimentary sequences in terms of world-wide sea-level curves and the body- and trace-fossil content of the Cape strata, is generally believed to range from earliest Ordovician to Mid-Carboniferous (Broquet, 1992). The basement rock consists of Late Precambrian low-grade metamorphic rocks of the Malmesbury and Kango Group and ~540 Ma plutons (Theron, 1992) of the Cape Granite Suite. The Table Mountain Group forms the lower part of the Cape Supergroup, above which lies the shale and sandstone formations of the Bokkeveld and Witteberg Groups. The Cape Supergroup is overlain by the varied sedimentary succession of the Karoo Supergroup. The great thickness and well-cemented character of the Table Mountain Group sandstones and quartzites have varied up to 2000 meters in high relief areas of the Cape Fold belt. Metamorphic conditions during the Cape Orogeny reached green-schist facies grade, and much of the sandstones in the Table Mountain Group recrystallised to quartzite. Multiphase deformation of the basement Kango and Malmesbury Groups occurred during Pan-African orogenesis between 600 and 500 Ma. Many of the structures were reactivated during the Cape Orogeny (250 Ma) and during the break-up of the Gondwana during the Mesozoic period. During the break-up of Gondwana land, Cape Supergroup strata were subjected to tensional stresses resulting in complex horst, graben and half-graben structures. These are readily recognized wherever younger (Mesozoic) sediments are preserved in fault-bounded basins (De Beer, 1992).

2.4 Climate of the Area

The Western Cape Province is situated in the southwestern part of South Africa. This South African province experiences a Mediterranean-type climate (warm dry summer and cold wet winter). As you go towards the north this climate regime grades into semi-desert and towards the east, the climate becomes less seasonal and tends towards subtropical on the coast (Theron, 1992).

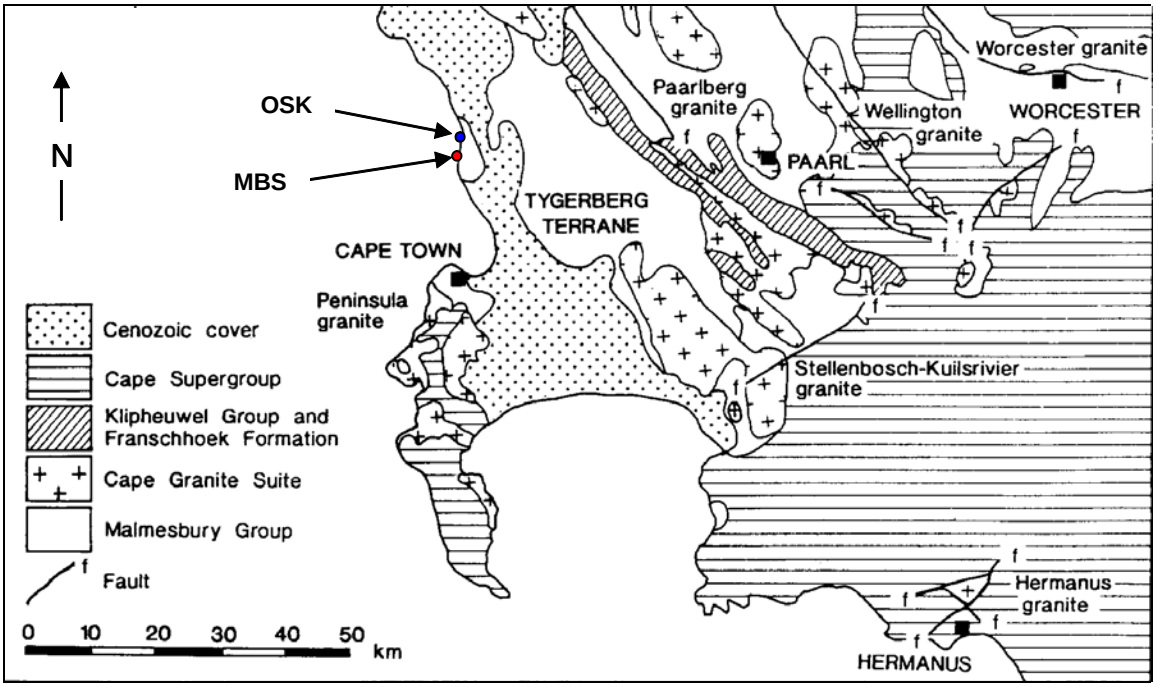

Figure 2.1: Geological map of the Western Cape coast, South Africa (adapted from Rozendaal et al., 1995).

The Western Cape summer season is dry and sunny with a maximum temperature around 28ºC, whilst the winter season is cold with an average minimum temperature of around 5ºC and a maximum temperature around 17ºC (Theron, 1992). However, in the areas that are near the coast, winds dominate very much (southerly and south-westerly in summer). Rainfall is highly variable with low summer (December-March) monthly means of ±50 mm and winter (June-August) over 200 mm, respectively. In the Western Cape there are rapid changes in weather due to the mountainous nature of the Cape Fold Belt, and it also occasionally snows on the higher peaks. The cold Atlantic Ocean has a moderate effect on the temperature of this area. Most of the rainfall occurs as a result of cold fronts moving in from the South Atlantic Ocean.

2.5 Sample collection

Beach sands samples were collected along the coast in two different beach zones (Melkbosstrand and Ouskip Beach, respectively). Both these beaches are easily

accessible, which makes it easy to perform any sampling. In the present study, a partial grid sampling method was selected.

Sample locations were chosen by searching for concentrated heavy mineral sand deposits on the basis of visual inspection (colour). All samples were taken by first removing a few millimeters of the sand surface and taking the sample at the depth of 20 centimeters. At Melkbosstrand beach, dark coloured sands were observed on the surface, while at Ouskip there was no such evidence. At Melkbosstrand, 10 samples were collected along the coast with spacing of 20 meters (from lower beach to upper beach) each in a direction parallel to the shoreline. Five transect samples were collected in a direction perpendicular to the shoreline, with 10 meter spacing. These 5 transect samples were collected to study the radionuclide concentration as a function of the distance from the shoreline towards the coast. At Ouskip 15 samples were collected using the same sampling method as used in Melkbosstrand beach. Ten of the 15 samples were collected along the coast with a spacing of 20 meters in a direction perpendicular to the shoreline. At this beach, the 5 transect samples were collected in the river mouth (Salt River) which deposits some material at the beach. From the 10 samples collected parallel to the beach, 3 were sampled from the lower side of the river, 2 samples at the mouth of the river and 5 were collected from the upper side of the river.

Due to observation of dark sands at Melkbosstrand, one sample was taken at a depth of 50 cm. When digging deeper, heavy mineral layers of 1-5 cm thick were observed (see Figure 2.2). The figure showing sampling method is shown in Figure 2.4 (a) and (b).

Figure 2.2: Sequences of approximately 1-5 cm thick of heavy mineral laminae intercalated with light colour minerals.

Figure 2.3: Picture showing a Global Positioning System (GPS) tool used to record sample locations.

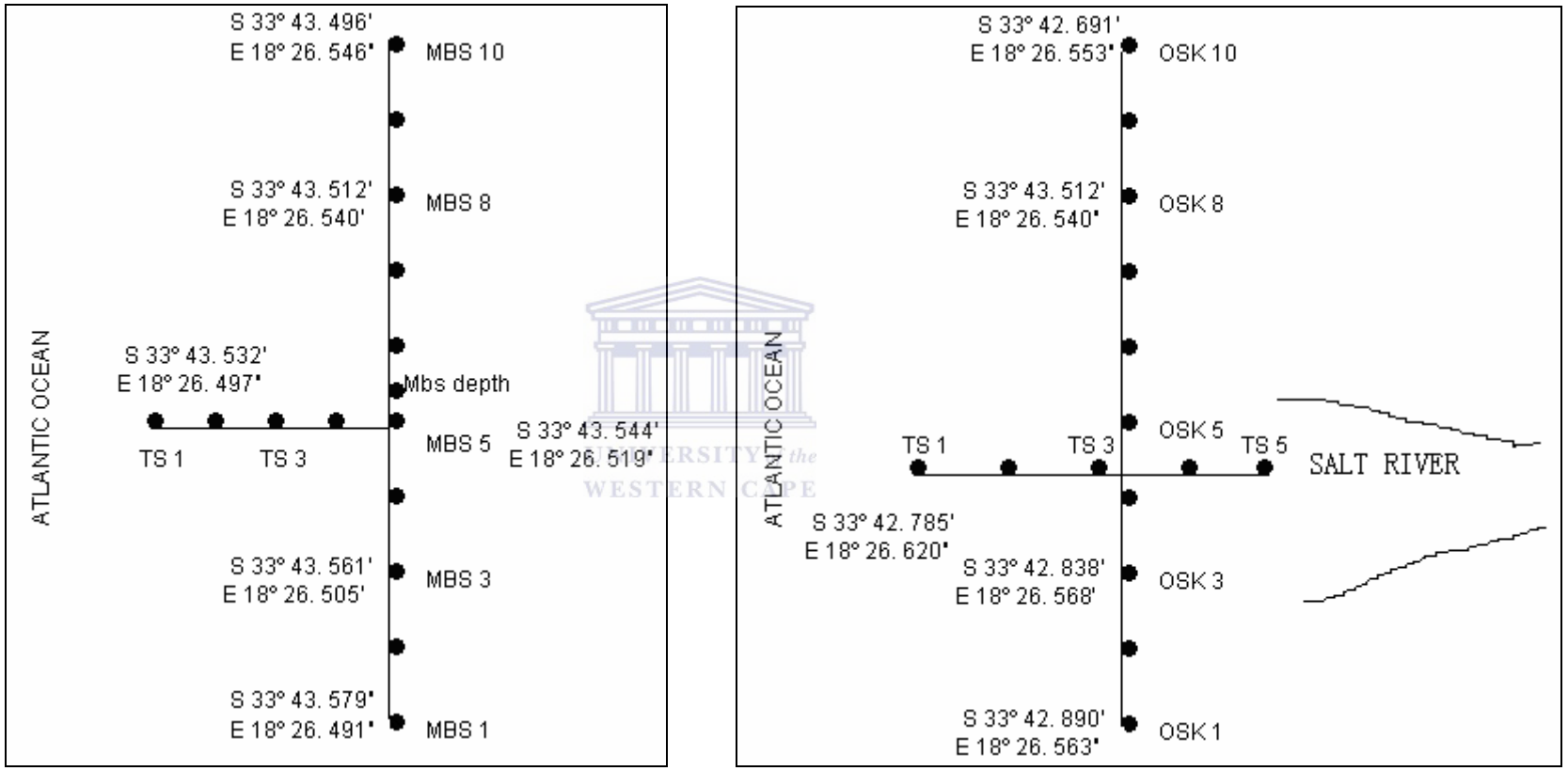

Figure 2.4: Schematic representation of sampling method at (a) Melkbosstrand (MBS), and (b) Ouskip (OSK) beach.

A Global Positioning System (GPS) tool was used to accurately locate (longitudinal and latitudinal) each sampling spot (see Figure 2.3). All the samples were packed in the plastic bags, and labeled.

2.6 Sample preparation

Sample preparation was performed at the Environmental Radioactivity Laboratory (ERL), iThemba LABS. Samples were washed with water to remove salt and other organic materials. After washing, samples were oven dried in an EcoTherm^{s} LABOTEC oven overnight at 105°C, and cooled to room temperature. After drying, sieving of sand samples was performed so as to remove sand grains with a diameter larger than 2 mm and other unneeded materials.

2.6.1 Coning and Quartering

The homogeneity of a sample is very important in laboratory analyses. A homogenous sample leads to data exhibition of minimal error attributable to sample heterogeneity. In this study the method used to homogenize the sample is the coning and quartering method. The coning and quartering technique involves pouring the sample into a cone shape and dividing the cone into four equal divisions (quartering). Then two-halves of the samples are taken for the proper representation of the total sample. The coning was achieved by pouring the sample into a funnel that allows sand to fall onto a sheet of paper, thereby forming a cone shape. Different grain-sizes are distributed in all directions (see Figure 2.5(a)). In this study, the sand cones were then separated into four quarters using a four corner Cu (copper) plate. After completing the quartering, the sand was then ready to be transferred to a Marinelli beaker. A figure showing a sand sample separated into four equal parts is shown in Figure 2.5(b).

Figure 2.5(a): Picture showing cone shaped sand.

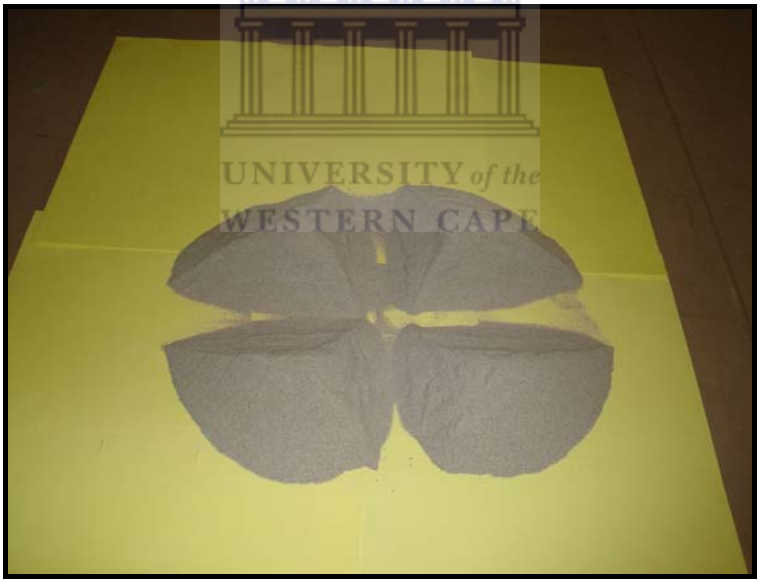

Figure 2.5(b): Picture showing the sand samples separated into four quarters (Quartering).

Quartering and coning is useful as it ensures that when transferring the sand samples into a Marinelli beaker, all grain sizes are represented. Marinelli beakers were first weighed on scale (Sartorius BP2100s). After quartering and coning was completed, sands were transferred into Marinelli beaker and filled to a 1-litre mark,

and this was done for all sand samples so that they all can have the same volume. The mass of the Marinelli beaker with a sample was weighed. Sample mass was then obtained by subtracting the mass of an empty Marinelli from a Marinelli filled with sample.

2.6.2 Marinelli beaker and sealing of the sample

When measuring soil samples it is advantageous to closely present a large quantity of a sample near the active volume of the detector, so as to optimize the gamma-ray detection efficiency (Sharshar et al., 1997). Thus, Marinelli beakers are used to measure soil samples. The Marinelli beaker used in this study is a 1-litre polypropylene beaker made by AEC-Amersham type (1W), and designed to have an annular bottom (85 mm annular bottom) so that it can slide over the HPGe detector (see Figure 2.6). This beaker was designed by L.D Marinelli in the early 1940s and was first used in 1943 specifically for biological applications (Oak Ridge, 1999).

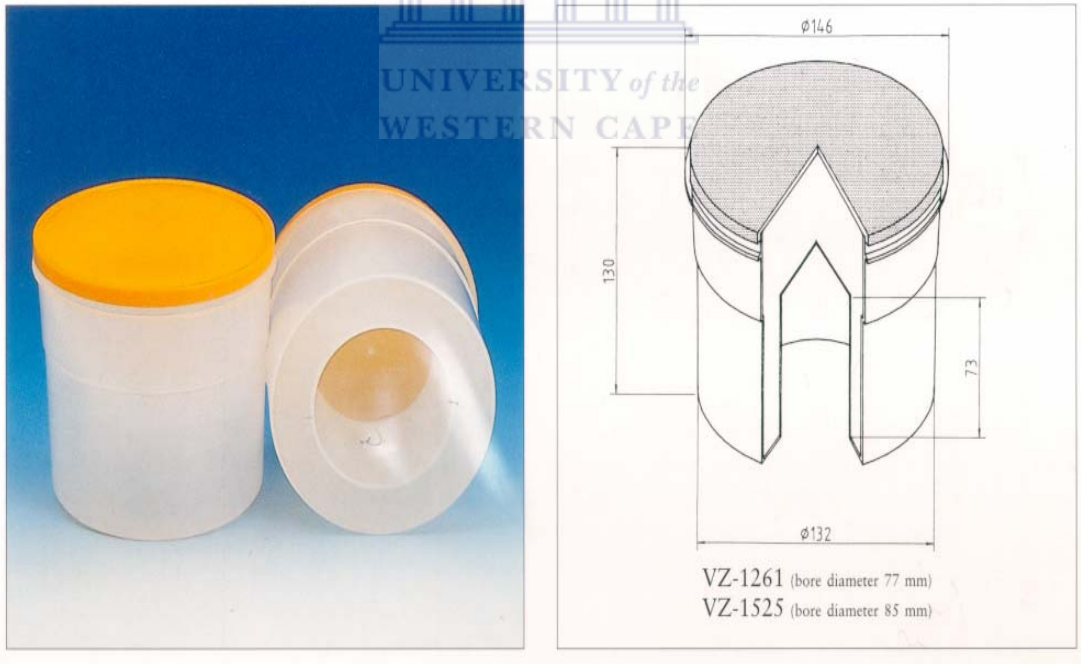

Figure 2.6: The geometry of the Marinelli beaker used for holding environmental samples for laboratory measurements with the Lead-shielded-HPGe detector.

Marinelli beakers reduce the effect of sample self-shielding and improve the detector's efficiency for counting the emitted radiation from the sample (Gehreke et al., 2005).

For each sample, a copper (Cu) lid of ~2 mm thickness was used as an extra lid by placing it on top of the sand sample inside the Marinelli and sealing it with a silicone sealant, so as to eliminate the leakage of radon(^{222}Rn produced in the ^{238}U decay series). Samples were also sealed outside the lid of the Marinelli beaker and kept for 21 days in order to achieve radioactive secular equilibrium between ^{238}U and ^{232}Th decay series and their respective progeny (by preventing the radiogenic gases ^{222}Rn and ^{220}Rn from escaping). The secular equilibrium is very important since it guarantees that the radioactivity of radon parent and radon daughter is equivalent (see Appendix A). An example of a sealed Marinelli beaker with a sand sample inside is shown in Figure 2.7. Table 2.1 shows all sample information including their masses after they were placed in Marinelli beakers. The depth sample (Mbs depth) which is dominated by dark sand has higher density then all other samples due to the presence of heavy minerals.

Figure 2.7: Picture of a sealed Marimelli beaker with a sample inside.

Table 2.1(a): Melkbosstrand sand samples collected parallel to the shoreline (see Figure 2.4(a)).

Sample Name	Sample Mass (kg)	Sample location	
		Latitude (South)	Longitude (East)
Mbs 1	1.54	33º 43. 579’	18º 26. 491’
Mbs 2	1.51	33º 43. 571’	18º 26. 498’
Mbs 3	1.57	33º 43. 561’	18º 26. 505’
Mbs 4	1.54	33º 43. 552’	18º 26. 513’
Mbs 5	1.51	33º 43. 544’	18º 26. 519’
Mbs 6	1.56	33º 43. 532’	18º 26. 526’
Mbs 7	1.55	33º 43. 523’	18º 26. 532’
Mbs 8	1.50	33º 43. 512’	18º 26. 540’
Mbs 9	1.55	33º 43. 504’	18º 26. 543’
Mbs 10	1.52	33º 43. 496’	18º 26. 546’
Mbs(depth)	1.73	33º 43. 544’	18º 26. 519’

Table 2.1(b): Melkbosstrand sand samples collected perpendicular to the shoreline (see Figure 2.4 (a)).

Sample Name	Sample Mass (kg)	Sample location	
		Latitude (South)	Longitude (East)
Mbs(TS) 1	1.50	33º 43. 532’	18º 26. 497’
Mbs(TS) 2	1.55	33º 43. 534’	18º 26. 502’
Mbs(TS) 3	1.51	33º 43. 537’	18º 26. 507’
Mbs(TS) 4	1.50	33º 43. 540’	18º 26. 513’
Mbs(TS) 5	1.51	33º 43. 544’	18º 26. 519’

Table 2.1(c): Ouskip sand samples collected parallel to the shoreline (see Figure 2.4(b)).

Sample Name	Sample Mass (kg)	Sample location	
		Latitude (South)	Longitude (East)
Osk 1	1.52	33º 42. 890’	18º 26. 563’
Osk 2	1.54	33º 42. 865’	18º 26. 565’
Osk 3	1.50	33º 42. 838’	18º 26. 568
Osk 4	1.52	33º 42. 812’	18º 26. 570’
Osk 5	1.51	33º 42. 787’	18º 26. 567’
Osk 6	1.52	33º 42. 762’	18º 26. 563’
Osk 7	1.52	33º 42. 736’	18º 26. 561’
Osk 8	1.51	33º 42. 722’	18º 26. 562’
Osk 9	1.53	33º 42. 705’	18º 26. 557’
Osk 10	1.50	33º 42. 691’	18º 26. 553’

Table 2.1(d): Ouskip sand samples collected perpendicular to the shoreline (see Figure 2.4(b)).

Sample Name	Sample Mass (kg)	Sample location	
		Latitude (South)	Longitude (East)
Osk(TS) 1	1.44	33º 42. 785’	18º 26. 620’
Osk(TS) 2	1.50	33º 42. 789’	18º 26. 537’
Osk(TS) 3	1.51	33º 42. 786’	18º 26. 598’
Osk(TS) 4	1.52	33º 42. 787’	18º 26. 574’
Osk(TS) 5	1.48	33º 42. 785’	18º 26. 559’

2.6.3 Grain-size separation

Sediment transport is a complex problem and therefore, in order to be approximately described by gamma-ray spectrometry, it is of value to use additional parameters such as grain-size distributions (De Meijer, 1998; Asadov et al., 2001 and

De Meijer et al., 2001). As in beaches heavy minerals are often concentrated in rather localized spots, usually in the swash zones or at eroding cliffs, a fraction of heavy minerals of beach sand may vary rapidly both in time and in location (Anjos et al., 2006). Thus, it is essential to separate sand samples into grain-size fractions where heavy minerals would be isolated into fine fractions and evaluate the effect of grain-size separation on the eTh/eU ratio, and verify whether the radiometric technique can be used as an alternative method to provide provenance information of the sand deposits.

The base two logarithmic ϕ (phi) scale is one useful and commonly used way to represent grain size information for a sediment distribution. The logarithmic phi values are calculated from particle diameter size measured in millimeters as follows:

$$\phi = -\log_2 d = -\left(\frac{\log_{10} d}{\log_{10} 2}\right) \qquad (2.1)$$

where ϕ is a particle size in ϕ units, and d is the diameter of the sand grain in mm. In this study, grain size separation was performed by passing sand samples through different sieves namely, 355 μm (1.5 ϕ), 250 μm (2.0 ϕ), 180 μm (2.5 ϕ), 125 μm (3.0 ϕ), 90 μm (3.5 ϕ) and 63 μm (4.0 ϕ).

In bulk sand, different grain-sizes contribute different percentages to the volume. Thus, if a smaller amount of sand is sampled it becomes impossible to fill the Marinelli beaker with other grain-sizes which contribute much less percentage wise to that sample. Examples are the grain-sizes between 90 and 63 μm (where heavy minerals are found). These grain-sizes contribute a far lower percentage in volume to the bulk of sand. For most log-scale coastal regions, heavy minerals occur with mass percentage of 1% (de Meijer, 1998). Figure 2.8 shows the variation of grain-sizes in mass percentage (Figure adapted from Asadov et al., 2001).

Due to the above reasons, 125 and 180 μm grain-sizes were transferred into medium plastic vial (of volume approximately 93.7 cm^3) and 90 μm into smaller plastic vial, and sealed properly to prevent radon gas from escaping (see Figure 2.9

(a), (b) and C). The procedure used to calculate the detection efficiencies of the samples measured with small vial is discussed in chapter three.

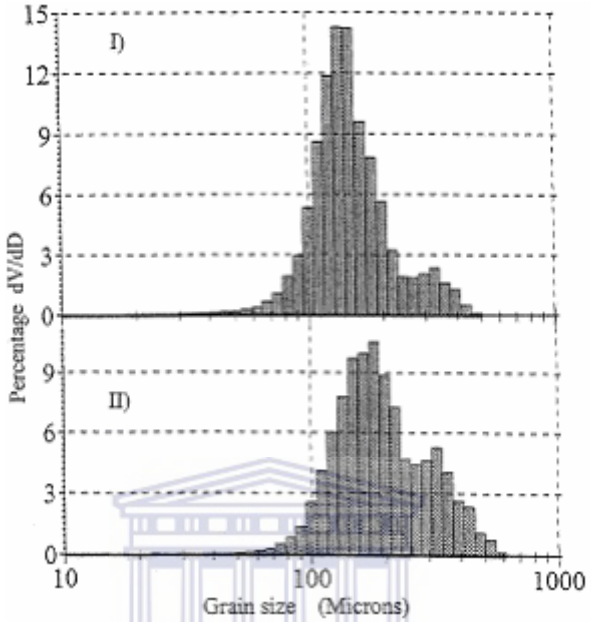

Figure 2.8: Percentage of the sample volume (dv/dD) contributed by each grain-size (D) to total volume (V). (I) represents white sands and (II) represents black sands (Asadov et al., 2001).

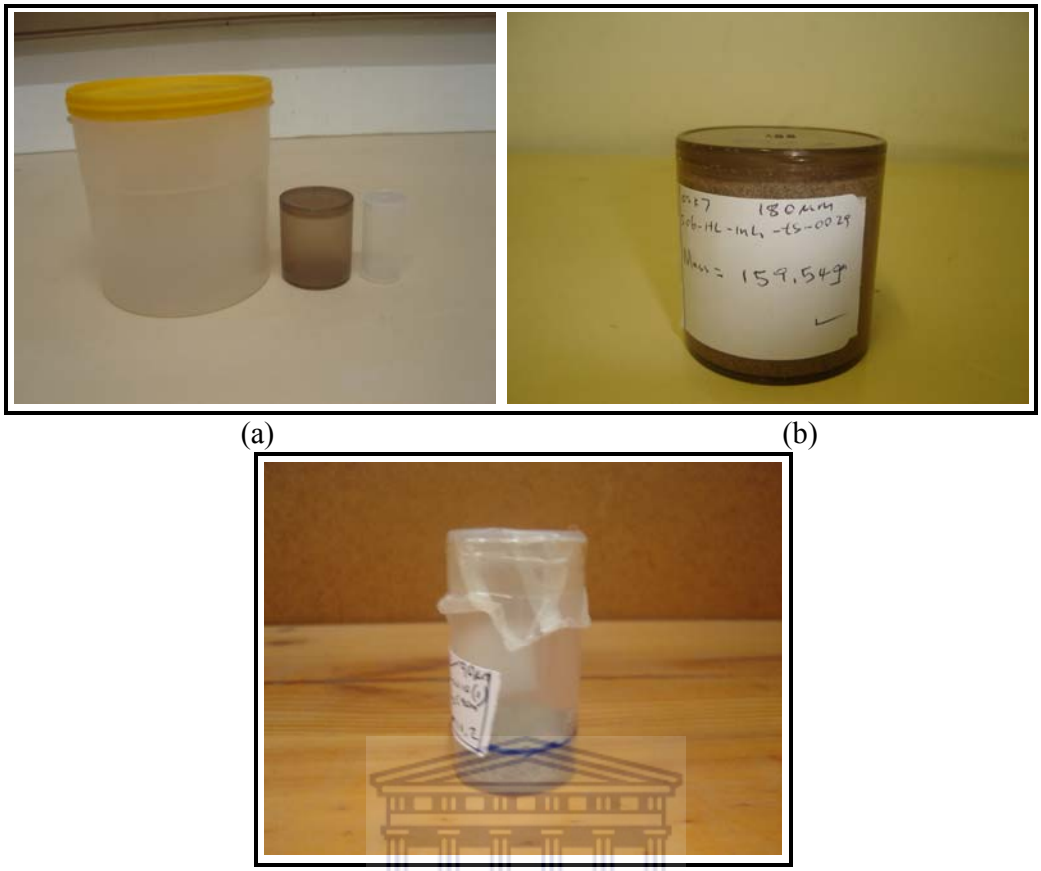

(a) (b)

(c)

Figure 2.9: (a) Picture showing the Marinelli beaker, a medium vial and small vial. (b) Picture showing a medium vial filled with a sand sample. (b) Picture showing small sample with a sand sample inside.

CHAPTER 3

RADIOMETRIC MEASUREMENTS

3.1 Introduction

In 1895, Wilhelm Roentgen measured penetrating radiation, which he named X-rays. In 1896, another physicist by the name of Henri Becquerel went further by observing fogging of photographic plates by an unknown radiation emanating from uranium-bearing rocks (Lilley, 2001). Becquerel's observations were further studied by Marie and Pierre Curie and by Ernest Rutherford. It was then discovered that there are three different types of radiation emitted by a radioactive source and they were classified as α, γ and β particles. Ever since the discovery of these radioactive particles, there have been many studies conducted to improve the understanding of these particles.

This chapter describes the background information on radioactivity and its measurements. The main focus is on γ-rays, since this study is based on measuring γ-rays emitted by primordial radionuclides (^{238}U, ^{232}Th and ^{40}K) contained in beach sands, using gamma-ray spectrometry (HPGe gamma-ray detector). This chapter also describes the interaction of gamma-rays with matter and the detector system used for gamma-ray spectrometry. The experimental procedure including energy and detector efficiency calibrations is also described.

3.2 Radioactivity and Radioactive decay

Radioactivity is the spontaneous process of disintegration of atomic nuclei. During this process alpha particle, beta particles or high frequency electromagnetic rays (γ-rays and X-rays) are emitted. Alpha particles are radiated by large, heavy radioactive nuclides, in particular those with $82 < Z \leq 92$ (Lilley, 2001). In α emission, the parent nucleus loses two positive units of electrical charge and also its

mass decreases because 4 nucleons are lost. A α (^{4}He-nucleus) emission can be symbolically represented as:

$$ {}^{A}_{Z}X \rightarrow {}^{A-4}_{Z-2}Y + {}^{4}_{2}\alpha + \gamma \qquad (3.1) $$

where X represents chemical symbol of a parent atom and Y is the daughter atom and a gamma-ray (γ). However, not all alpha emissions produce a gamma-ray (γ).

Beta (β) particle emission takes place due to nuclear transition modes that increase or decrease the atomic number Z of a nucleus by 1 while leaving the mass number A unaffected. Unstable nuclei, which are described as either proton rich or neutron rich, decay towards the line of stability into other isobaric nuclei by positive or negative β-particle emission or by the capture of an atomic electron (Lilley, 2001). During this particle emission, light particles called leptons are created leading to a more stable final product. The leptons (${}^{0}_{-1}\beta^{-}, \nu$) and anti-leptons (${}^{0}_{1}\beta^{+}, \bar{\nu}$) are created by the action of a weak nuclear force, which is why beta decay, generally, is a relatively slow process compared to transitions involving the strong force or the electromagnetic interaction (Lilley, 2001). Thus, the beta transition process can occur in three different ways which are namely *negative beta decay (β^-)*, *positive beta decay (β^+)* and *electron capture (EC)*.

In negative beta particle emission, a neutron-rich nuclide undergoes a process where-by a neutron is converted into a proton, (β^-) and anti-neutrino ($\bar{\nu}$). A β$^-$ particle is an electron (e$^-$) and when it is emitted, the charge on the nucleus increases by one unit. Symbolically, this can be represented as:

$$ {}^{A}_{Z}X \rightarrow {}^{A}_{Z+1}Y_{N-1} + \beta^{-} + \bar{\nu} \qquad (3.2) $$

Positive β particle emission occurs in proton-rich nuclides. During this transition, a proton is converted into a neutron, positron (β^+) and a neutrino (ν). A positron e$^+$ a positive β particle. This transition can be symbolically represented as:

$$ {}^{A}_{Z}X \rightarrow {}^{A}_{Z-1}Y_{N+1} + \beta^{+} + \nu \qquad (3.3) $$

In the case of electron capture (EC), a proton and an atomic electron are transformed into a neutron and neutrino. This transition occurs in proton rich nuclides. Symbolically, this can be represented as:

$$p + e^{-} \rightarrow n + \nu \qquad (3.4)$$

In the radioactive decay processes, both alpha particle emission and emission of negative beta particles might be followed by emission of one or more gamma-rays which are photons of electromagnetic radiation such as X-rays or visible light (Tykva, 1995). These gamma-rays are formed if the daughter nucleus is formed in an excited state (nuclear isomer). This daughter nuclide either falls directly to the ground state or descends in steps to lower energy states through emission of energy as gamma radiation. This type of emission is also called nuclear decay and takes place due to excess energy possessed by radioactive nuclides. For example, in the β^{-}-decay of $^{60}_{27}Co$ to $^{60}_{28}Ni$, two gamma-rays of 1.332 and 1.173 MeV, are emitted. The decay scheme illustrating this beta decay is shown in Figure 3.1.

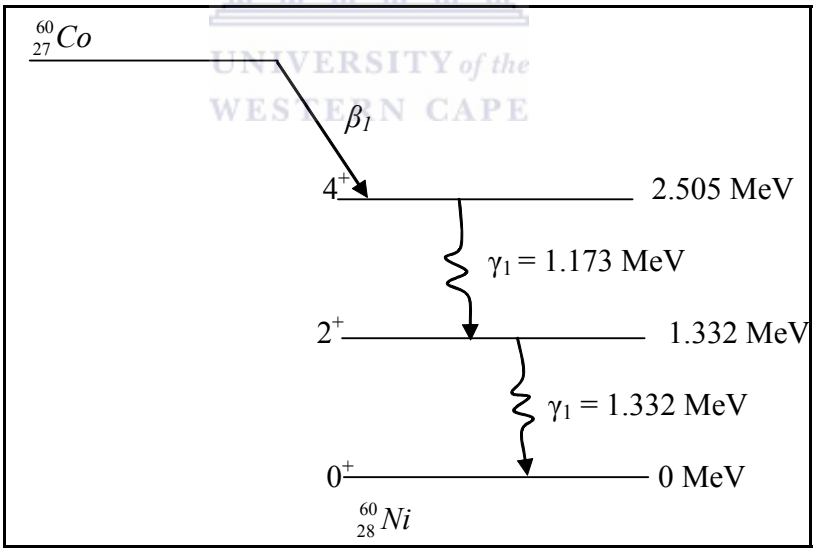

Figure 3.1: Decay scheme of ^{60}Co (Knoll, 1989).

Gamma-rays have energies typically ranging from 0.1 to 10 MeV characteristic of energy difference between nuclear states, and thus corresponding to wavelengths of between 10^4 and 100 fm (Krane, 1988; Hashim, 2000). They are emitted at energies corresponding to the energy state transitions a nuclide may

undergo when in an excited state. The energy, E_γ, of a gamma-ray is described as the difference in energy of nuclear isomers (nuclide in an excited energy state):

$$E_\gamma = h\nu = E_1 - E_2 \qquad (3.5)$$

where $h\nu$ is the energy of electromagnetic radiation and E_1 and E_2 represents the energy levels of nuclear isomers. A diagram summarizing the radioactive decay processes is shown in figure 3.2.

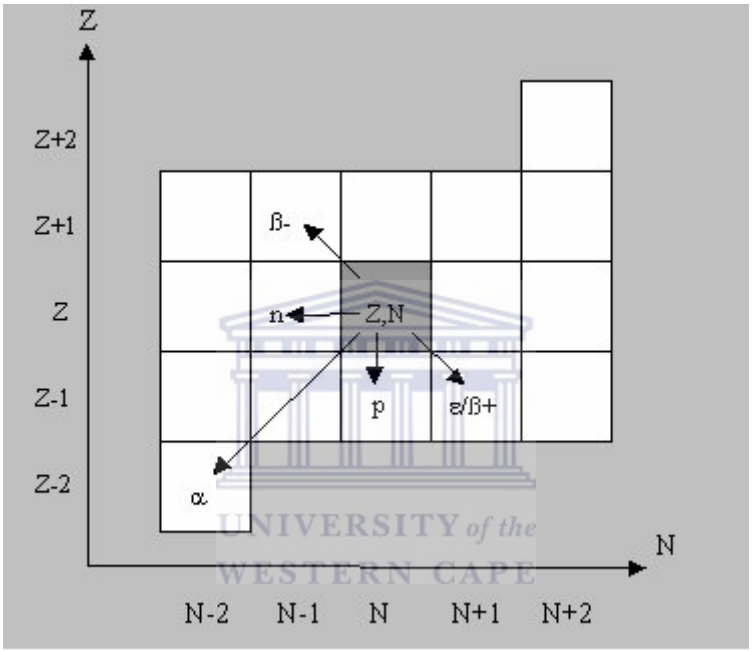

Figure 3.2: Nuclide Chart plot of Z vs. N showing radioactive decay processes. A nuclide with co-ordinates Z and N decays to the position shown depending on the process (Www01).

Radiation is divided into two groups, which are namely ionizing radiation and non-ionizing radiation. Ionizing radiation refers to the ability of the radiation to ionize a gas though which it passes (Tsoulfanidis, 1983). Non-ionizing radiation is the electromagnetic radiation with wavelength λ of about 1 nm or longer, and this includes radiowaves, microwaves, visible light (λ = 770 nm to 390 nm), and ultraviolet light (λ = 390 nm to 1nm) (Tsoulfanidis, 1983). Ionizing radiation is of interest in measurements of radiation because it may cause diverse physical and chemical effects in matter, including ionization, heat generation, electronic excitation of atoms and molecules, atomic displacement, nuclear reactions and breaking of

chemical bonds (Lilley, 2001). Ionizing radiation can damage materials, and thus it is considered dangerous. However, it is also easy to detect and can be controlled (Lilley, 2001).

Radioactive nuclides or so-called radionuclides are nuclei that consist of unstable combinations of protons and neutrons, and disintegrate to other nuclei under the emission of radiation. These nuclides decay continuously, producing more stable nuclides called daughter nuclides. If the daughter is also unstable, the radioactive decay process continues in a decay chain until a stable decay product is reached. Such a chain of decay products is called a decay series (see an example Figure 3.4 and 3.5). Radionuclides can be *anthropogenic* (man-made) or *primordial* (naturally occurring). The unit of radioactivity is Becquerel (Bq), named after Henri Becquerel. The historical unit that was previously used is Curie (Ci) which is 3.70×10^{10} decays per second and 1 Ci was originally the activity of 1 gram of radium. The number of radionuclides in a substance diminishes in time due to radioactivity:

$$N(t) = N_0 e^{-\lambda t} \tag{3.6}$$

where, $N(t)$ is the number of nuclides at time t, N_0 is the number of nuclides present at time t_0 and λ is the decay constant related to the half-life time ($t_{1/2}$) of the radionuclide by:

$$\lambda = \frac{\ln 2}{t_{1/2}} \tag{3.7}$$

The activity A (Bq) is defined as the number of nuclei that disintegrated per unit time:

$$A = -\frac{dN}{dt} = \lambda N \tag{3.8}$$

3.2.1 Half-life ($t_{1/2}$)

Half-life is the term used to express the rates of radionuclide decay (L'Annunziata, 1998). This is the average time, t, required for a given amount of

radioactive nuclide to lose half of its activity. The symbol $t_{1/2}$ is used to denote half-life. Each radionuclide has its own unique half-life that is independent of its chemical or physical state. Half-lives of radionuclides can be as small as in nanoseconds and some can be billions of years (see Table 3.1). An example illustrating the concept of half-life is given in Figure 3.3.

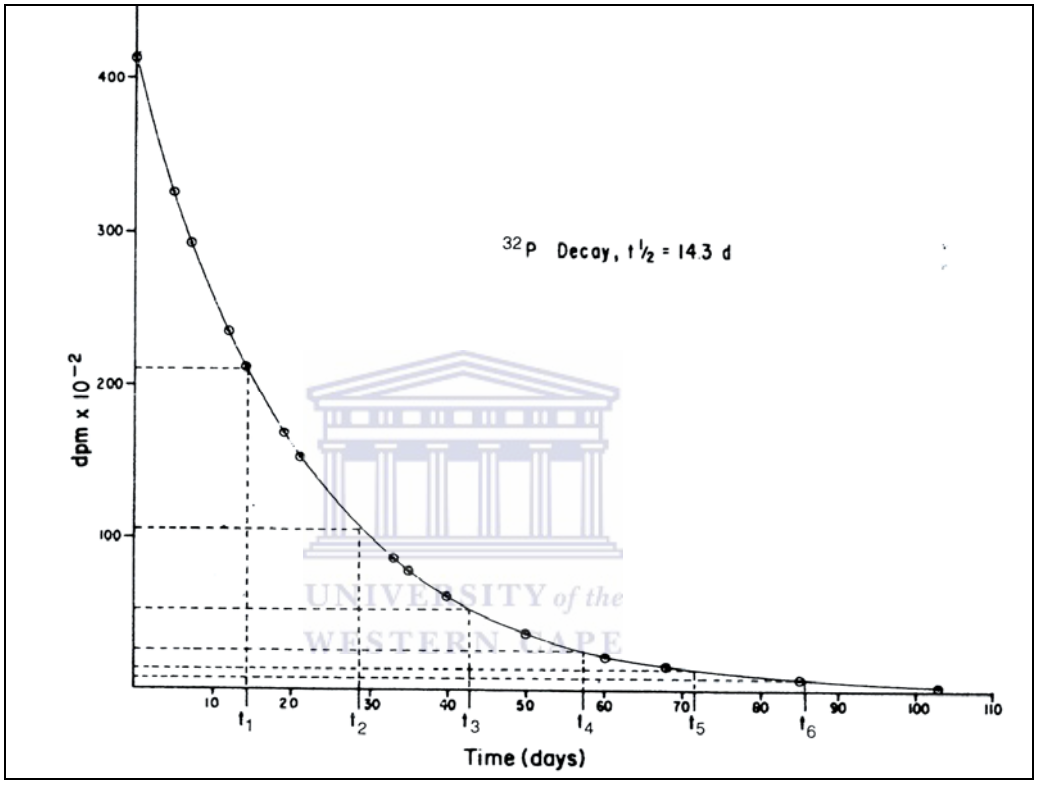

Figure 3.3: Decay of ^{32}P represented as linear plot (L'Annunziata, 1998).

This figure indicates the activity of ^{32}P plotted against time in days. It clearly reflects that after every interval of 14.3 days, the radioactivity of ^{32}P is reduced by half. Therefore, 14.3 days is the half-life ($t_{1/2}$) of ^{32}P.

3.3 Environmental radioactivity

Radioactive materials can be found anywhere in the earth, and they can be categorized into three different types, mainly *primordial*, *cosmic* and *anthropogenic* radionuclides (De Meijer et al., 1997). Primordial are those which have existed since the formation of the earth. Their half-lives are sufficiently long in such a way that

they can be comparable to the age of the earth. Cosmic radionuclides e.g. ^{22}Na, ^{7}Be and ^{14}C are formed by rapid bombardment of the stable atoms in the atmosphere and biosphere by cosmic rays originating from outer space. Anthropogenic radionuclides are man made radionuclides released into the environment through nuclear weapons testing, nuclear accidents which may be similar to the Chernobyl accident and during radio-isotopes manufacturing. In the present study the main focus is on primordial radionuclides and they are described in more detail below.

3.4 *Primordial Radionuclides*

Primordial radionuclides (^{232}Th, ^{238}U, ^{40}K) are of terrestrial origin and are present in the earth's crust over the geologic period. These radionuclides have longer half-lives, sufficiently long that they have survived since their creation and have half-lives at least comparable to the age of the earth (several billion years) and have not substantially decayed. Naturally occurring radionuclides can be found in water, soil and air, even in human bodies.

Examples of primordial radionuclides relevant to this study, with their half-lives and their specific isotopic abundances are shown in Table3.1.

Table 3.1: Primordial radionuclides with their half-lives and abundances.

Nuclide	Half-live(yr)	Abundance
Uranium 235	$7.10x10^{8}$	0.720%
Uranium 238	$4.47x10^{9}$	99.3%
Thorium 232	$1.41x10^{10}$	100%
Potassium 40	$1.28x10^{9}$	0.0117%

Uranium and thorium are parents of three radioactive series (decay chains) headed by naturally occurring unstable nuclei ^{238}U, ^{235}U and ^{232}Th, respectively (Tykva, 1995). These three sets are usually called the uranium series, actinium series and thorium series. Figure 3.4 to Figure 3.6 shows the decay chains of ^{238}U, ^{232}Th and ^{40}K, with the emission of α-particles indicated by vertical lines and β-particles

indicated by diagonal lines. Grey boxes denote the gamma-ray emitters relevant to this study. In the ^{238}U decay chain ^{222}Rn (Radon) is the only daughter radionuclide found in a gaseous state and thus can diffuse through the soil very easily. If this radionuclide is stopped from escaping, its daughter nuclides such as ^{214}Bi and ^{214}Pa are then in secular equilibrium with ^{226}Ra, and thus all the decay products can be used to calculate the activity concentration of ^{238}U (see Appendix A).

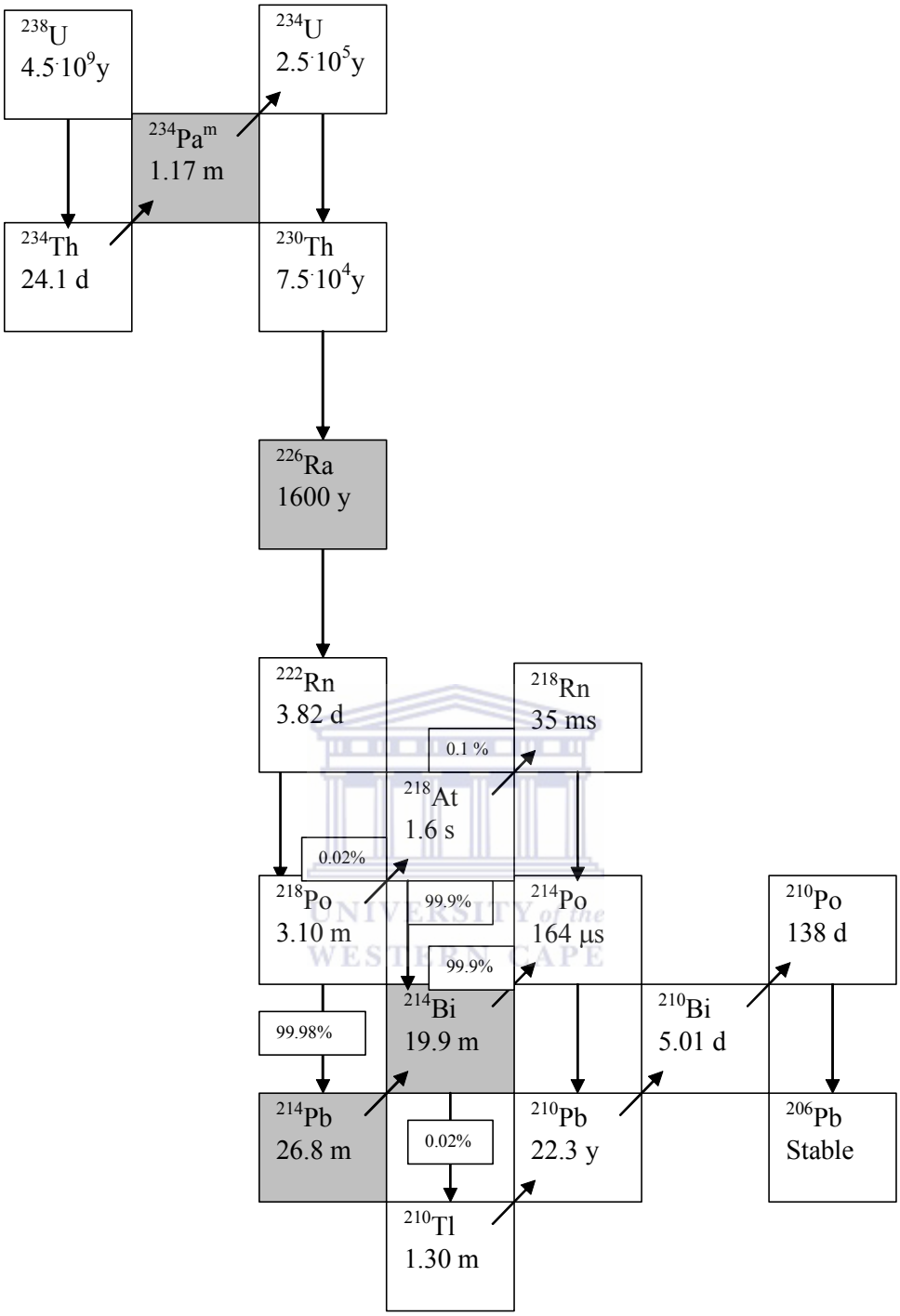

Figure 3.4: Schematic diagram showing the ^{238}U decay chain. The grey boxes represent gamma-rays emitters relevant to this study (Evens, 1969).

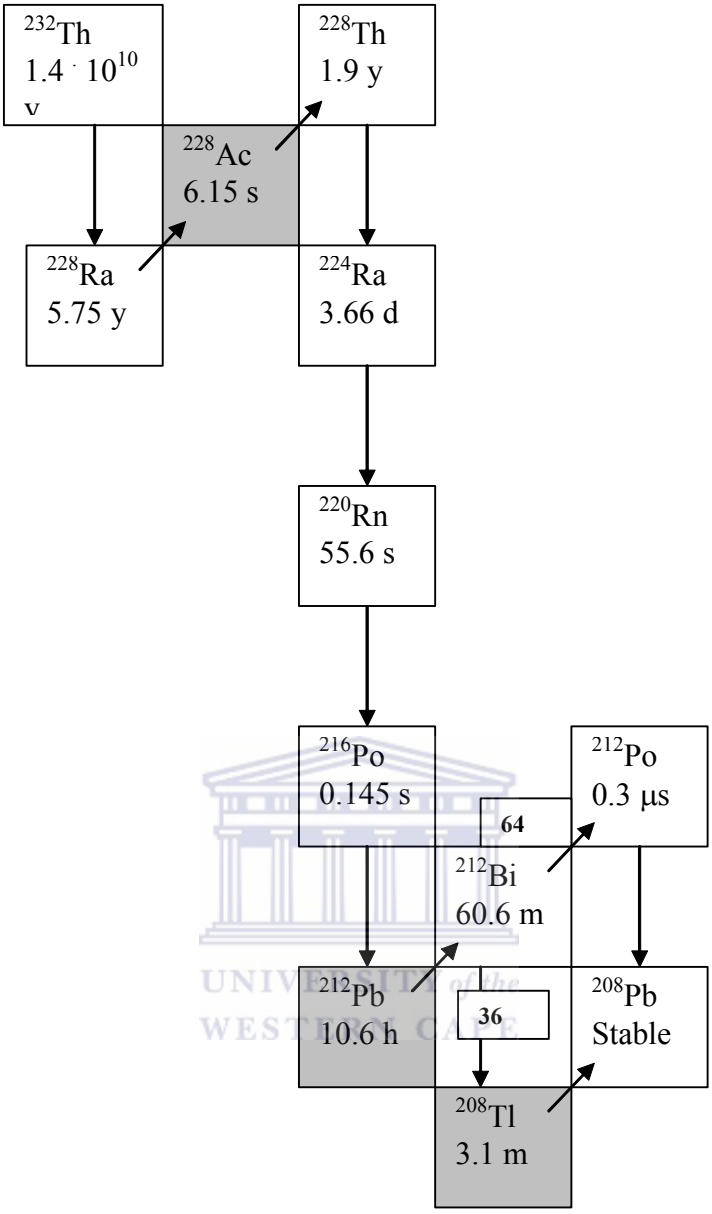

Figure 3.5: Schematic diagram showing the ^{232}Th decay chain. The grey boxes represent the γ-ray emitters of relevance to this study (Evans, 1969).

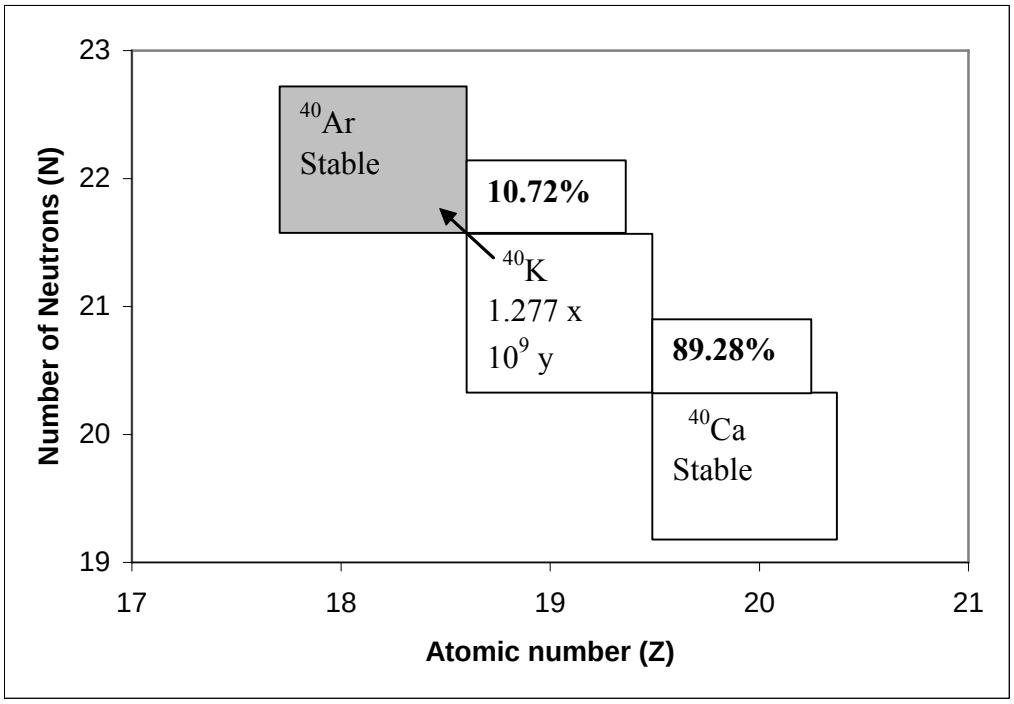

Figure 3.6: Schematic diagram showing the ^{40}K decay chain. The grey box represents the γ-ray emitter (Evans, 1969).

3.5 Interaction of gamma-rays with matter

Gamma-rays are electromagnetic waves produced spontaneously by radioactive elements. Gamma-rays are more efficiently detected by high atomic number (Z) materials. These radioactive particles are very penetrative and have longer range in matter than other radioactive particles such as alphas and beta particles. However, gamma-rays are absorbed by matter, and there are three primary interaction processes by which gamma-rays interacts with matter, namely the *Photoelectric effect*, the *Compton Effect* and *Pair production*. This interaction processes lead to the partial or complete transfer of the gamma-ray photon energy to electron energy.

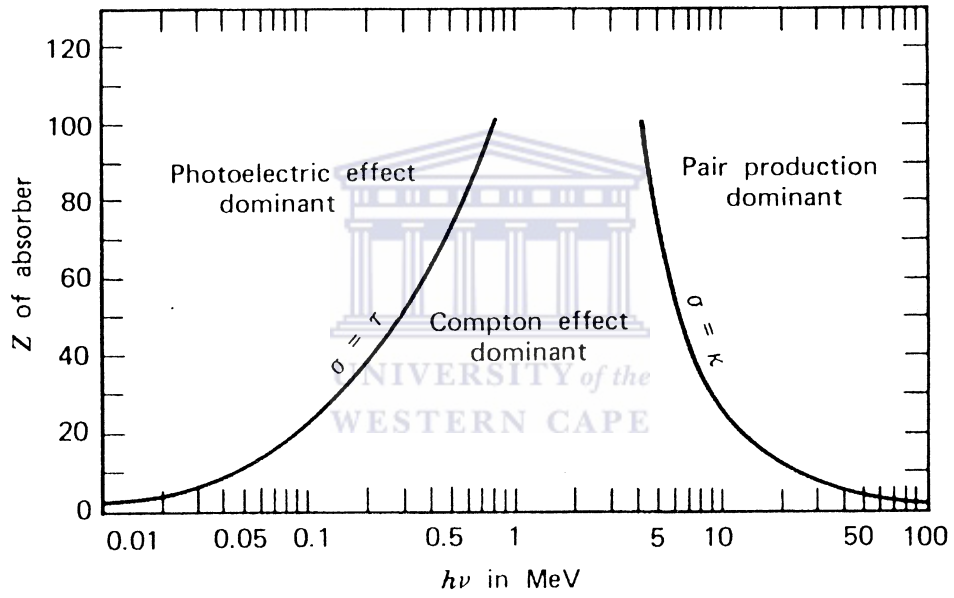

Figure 3.7: A diagrammatic representation of the three-interaction processes (Tsoulfanidis, 1983)

The above figure (Figure 3.7) indicates clearly the relative importance of interaction processes as atomic number Z and gamma-ray energy (E_γ) changes.

3.5.1 Photoelectric Effect

During photoelectric effect interaction there is the absorption of a photon by an atomic electron with subsequent ejection of the electron by the atom from one of its bound shells (see Figure 3.8). The interaction is with the atom as a whole and

cannot take place with free electrons. The formula to calculate the energy of the ejected electron from its shell with a kinetic energy E_e is given by Einstein's photoelectric equation:

$$E_e = hv - E_b \qquad (3.9)$$

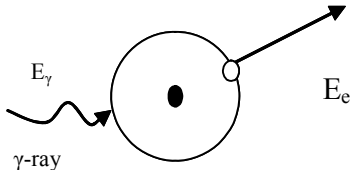

Figure 3.8: The mechanism of photoelectric absorption, where a γ-ray with energy, E_γ, interacts with a bound electron.

where, E_e is the kinetic energy of the ejected electron, hv is the energy of the incident photon, and E_b is the energy required to remove an electron from an atom (binding energy). The atom is left in an excited state with an excess of energy E_b and it recovers its equilibrium by de-exciting and thus redistributing its energy between the remaining electrons in the atom. This could result in a release of further electrons from the atom, and thus causing an Auger cascade (Gilmore, 1995).

3.5.2 Compton Effect

This interaction process is also called Compton scattering and is simply scattering of photons from a free electron. The schematic representation in Figure 3.9 represents the Compton scattering process, whereby an incident gamma-ray photon having energy E_γ is deflected by an atomic electron resulting in a scatted photon of energy $E_\gamma^{/}$ at an angle θ and an electron is deflected at an angle ϕ to the trajectory of the incident gamma-ray photon E_γ. The energy imparted to the recoil electron is given by:

$$E_e = E_\gamma - E_\gamma^{/} \tag{3.10}$$

This process is dominant at energies between 0.5 and 5 MeV as is clearly shown in Figure 3.7. The equation to calculate the energy of a deflected photon is given by:

$$E_\gamma^{/} = \frac{E_\gamma}{1 + \frac{E_\gamma}{m_0 c^2}(1 - \cos\theta)} \tag{3.11}$$

where m_0c^2 is the rest-mass energy of the electron (0.511 MeV) when gamma photon energy values are expressed in MeV (L'Annunziata, 1998). The maximum energy transfer to the electron occurs for a scattering angle of θ = 180º.

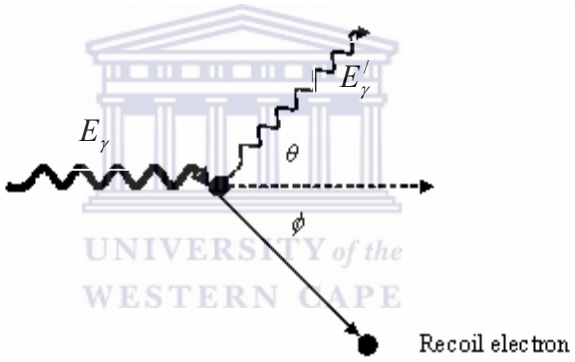

Figure 3.9: Compton Effect diagram. An incident photon collides with an atomic electron and a photon is deflected to angle θ relative to the trajectory of the of the incident photon.

The probability of Compton scattering per atom of the absorber depends on the number of electrons available as scattering targets and therefore increases linearly with the atomic number Z (Knoll, 1989). The angular distribution of scattered gamma-rays determined through a quantum mechanical calculation of the process results in the Klein-Nishina formula (Leo, 1987).

$$\frac{d\sigma}{d\Omega} = Zr_0^2\left(\frac{1}{1+\alpha(1-\cos\theta)}\right)^2\left(\frac{1-\cos^2\theta}{2}\right)\left(1+\frac{\alpha^2(1-\cos\theta)^2}{(1+\cos^2\theta)[1+\alpha(1-\cos\theta)]}\right), \tag{3.12}$$

where $\alpha = hv/m_0c^2$ and r_0 (the classical electron radius) = 2.181 fm. The total Compton scattering cross-section σ is given by (Knoll, 1989):

$$\sigma = const \times E_\gamma^{-1} \tag{3.13}$$

and σ is independent of atomic number Z, hence it is independent on the medium.

3.5.3 Pair production

In this interaction, there is a transformation of a photon in to an electron and a positron. However, for this process to conserve momentum it can only occur in the presence of a third body, usually a nucleus. The process occurs within the coulomb field of the nucleus resulting in the transformation of a gamma-ray into an electron-positron pair. For the pair (electron and positron) to be created the photon must at least have energy of 1.022 MeV (Leo, 1987). When the positron is slowed to the thermal velocity of an atomic electron, it annihilates with an electron and produces two gamma rays each having energy of 511 keV, which will move in opposite directions in order to conserve momentum. A schematic diagram showing the mechanism of pair production is shown in Figure 3.10.

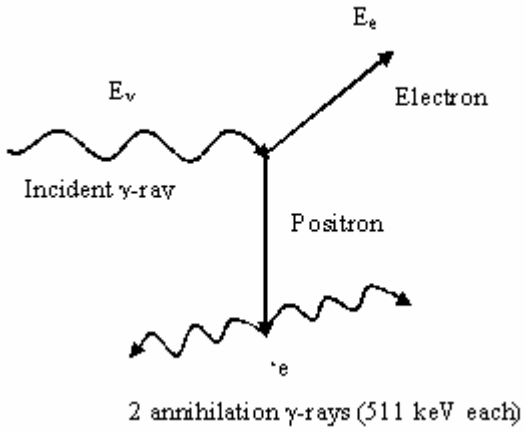

Figure 3.10: Schematic diagram of the mechanism of pair production.

Pair production is not of interest for the study of naturally occurring radionuclides since it is only important for $E_\gamma > 3$ MeV (Hendriks et al., 2001).

3.6 Attenuation of gamma-rays

During attenuation, interaction processes remove gamma-ray photons from the photon beam, which results in the reduction of the beam intensity. If the photon beam is well collimated, all three interactions cause it to be attenuated as it crosses through the absorber material. Photons, which undergo photoelectric absorption or pair production disappear altogether and most of those that are Compton scattered are reflected away from reaching a detector placed in the forward direction (Lilley, 2001). For a well-collimated beam, it is easy to calculate the dependence of photon intensity on the absorber thickness and vice versa.

The total probability for interaction μ (probability of interaction per unit distance), called the total linear attenuation coefficient, is equal to the sum of the three probabilities and is given by:

$$\mu = \tau(photoelectric) + \sigma(compton) + \kappa(pair) \qquad (3.14)$$

and this is the probability per unit length that the photon is removed from the beam. Thus, a well-collimated beam intensity at a depth x of the absorber material can be calculated by:

$$I = I_0 e^{(-\mu x)} \qquad (3.15)$$

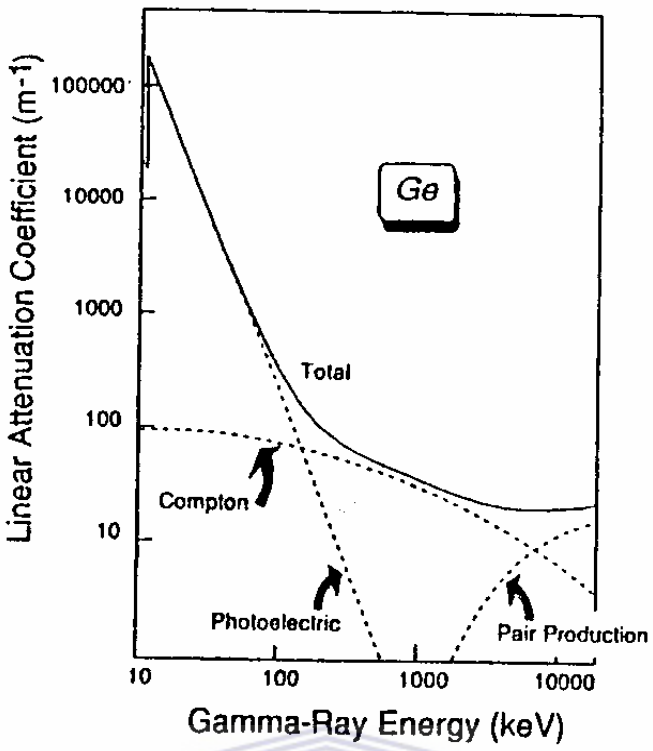

Figure 3.11: Linear attenuation coefficients in germanium. Dashed lines indicate separate contributions due to the photoelectric effect, Compton scattering and pair production (Gilmore, 1995).

The gamma-ray photons can also be characterized by their mean free path λ, defined as the average distance traveled through the absorber before an interaction takes place. It can be obtained from the equation;

$$\lambda = \frac{\int_0^\infty x e^{-\mu x} dx}{\int_0^\infty e^{-\mu x} dx} = \frac{1}{\mu} \tag{3.16}$$

The linear absorption coefficient depends on the state of the absorber or the number of atoms per unit volume of the absorber (L'Annunziata, 1998). Thus, this characteristic limits its use. The mass attenuation coefficient, μ_m, is independent of the physical states of the absorber material and thus is more widely used, and given by:

$$\mu_m = \frac{\mu}{\rho} \tag{3.17}$$

where ρ represents the density of the absorber material. For a given total photon energy, the mass attenuation coefficient does not change with the state of an absorber material. The mass attenuation of any mixture of elements, or chemical compound can be given by:

$$\frac{\mu}{\rho} = \sum \frac{\mu_i}{\rho_i} w_i \tag{3.18}$$

where w_i is the weight fraction of the *ith* element in the material and $\frac{\mu_i}{\rho_i}$ is the total mass or the attenuation coefficient referring to *ith* element. Using the mass attenuation the intensity equation takes the form,

$$I = I_0 e^{(-\mu_m d_m)} \tag{3.19}$$

where μ_m is the mass absorption coefficient which has units $cm^2.g^{-1}$, and $d_m = \rho x$, the mass thickness of the absorber material in units $g.cm^{-2}$.

3.7 Coincidence summing

This is an important source of errors to be considered when performing radiometric measurements using gamma-ray spectrometry. Coincidence summing arises due to simultaneous detection of two or more gamma-rays that are emitted within the resolving time of electronics. Coincidence summing reduces the number of counts from the photo peak (summing-out) and increases the counts in the continuum. In some cases it increases the number of counts (summing in) of some peaks whose energy corresponds to the sum of the lower energy peaks (Knoll, 1989). The probability of coincidence summing is related to the nuclear level scheme, transition probabilities, the probability of internal conversion of transitions, and the detector full-energy peak and total efficiencies (Gehreke et al., 2005). The probability of the real sum peak is given by:

$$P = Ip\varepsilon_1\varepsilon_2 \tag{3.20}$$

where I is the intensity (Bq) of the source, ε_1 and ε_2 are the counting efficiencies for γ_1 and γ_2, respectively, and p is the intensity of the less abundant of the two coincident gamma-rays (L'Annunziata, 1998). If the two counting efficiencies (ε_1 and ε_2) are approximately equal, one can see that the intensity of the sum peak varies roughly as a square of the efficiency.

Coincidence summing depends greatly on the geometry between source and the detector. The reduction of the coincidence summing effect can be accomplished by increasing the source-to-detector distance. Gehreke et al., (2005) recommended a 10 to 20-cm source-to-detector distance for small to medium size (i.e., $\varepsilon_r < 40\%$) detectors and 30-cm or more for source-to-distance for larger (i.e., $\varepsilon_r > 50\%$) detectors to reduce coincidence summing of gamma-rays. However, for measuring low-level environmental samples, it is necessary to reduce the counting time by increasing the efficiency of the detector (high-source volumes and short detector-source distances) (Ramos-Lerate et al., 1997). As a result, coincidence summing corrections can reach values of about 5% in such environmental samples for normal size detectors (Ramos-Lerate et al., 1997; Quintana et al., 1995). And, more significantly, coincidence summing effects can also appear in the detector efficiency measurements, since they must be carried out in the same measuring conditions as for the activity concentration determination (Ramos-Lerate et al., 1997). A method of coincidence summing correction is explained by Ramos-Lerate (Ramos-Lerate et al., 1997).

3.8 Germanium detectors

Germanium detectors are the commonly used detectors in high resolution gamma-ray spectroscopy experiments today. This is due to their excellent energy resolution that gives them the best ability of identifying and differentiating any gamma-ray emitting isotopes. However, a certain disadvantage of germanium detectors exists in the relatively low energy needed to create a hole-electron pair (2.96 eV at 77 K) (Tykva, 1995). At room temperature, due to thermal excitation of electrons, an unacceptable increase of the reverse-current component generated in the detector volume occurs (Tykva, 1995). Thus, germanium detectors have to be cooled with liquid nitrogen.

Earlier production technologies only afforded germanium single crystals with high concentrations of impurities. As a result, Ge (Li)-detectors were used exclusively, in which the acceptors in p-type germanium were compensated by drift lithium ions (Tykva, 1995). These types of detectors are still used, but the more improved production technology of high-purity single crystals (HP crystals) permits the use of germanium alone for preparation of HPGe-detectors (Tykva, 1995). Germanium detectors are available with crystal diameters and lengths up to about 100 mm (Lilley, 2001). Similar to other semiconductor detectors, a germanium detector is a large reverse biased p-n junction diode. The diagram showing basic construction of a germanium detector is shown in Figure 3.12.

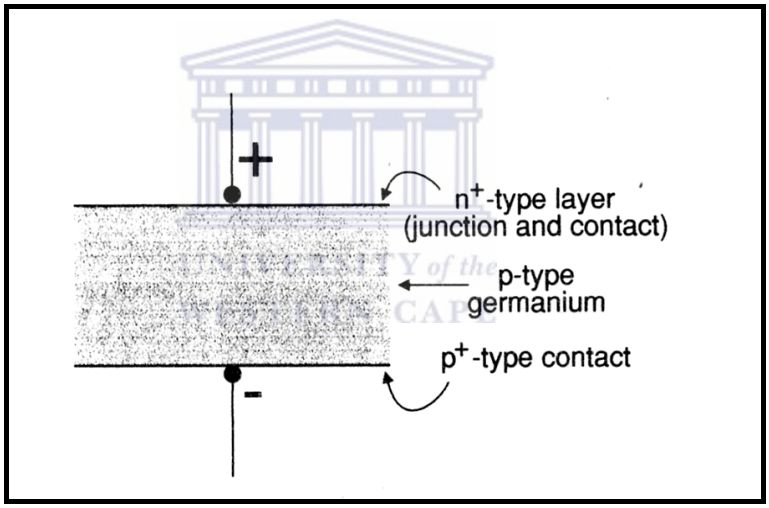

Figure 3.12: Basic construction of a germanium detector (Gilmore, 1995).

Under reverse bias, an electric field extends across the intrinsic or depleted region. The interactions of a photon with the material within the depleted volume of a germanium detector produce charge carriers. These charge carries are swept by the electric field to the P and N electrodes. The number of charge carriers is proportional to the energy deposited in the detector by the incoming photon. They are then converted to a voltage pulse by an integral charge sensitive preamplifier that is connected to the detector.

Today, a variety of HPGe detector types are available from manufacturers (e.g., Canberra, 2003; ORTEC, 2003; Princeton Gamma-Tech. (PGT), 2004). These can be divided into low energy detectors (3 to 100 keV), n- and p-type broad energy detectors (3 keV to 10 MeV) (Gehreke et al., 2005). At The iThemba LABS Environmental Radioactivity Laboratory (ERL), a Canberra type detector is used. Figure 3.13 shows different Ge detector geometries and the energy range they can cover.

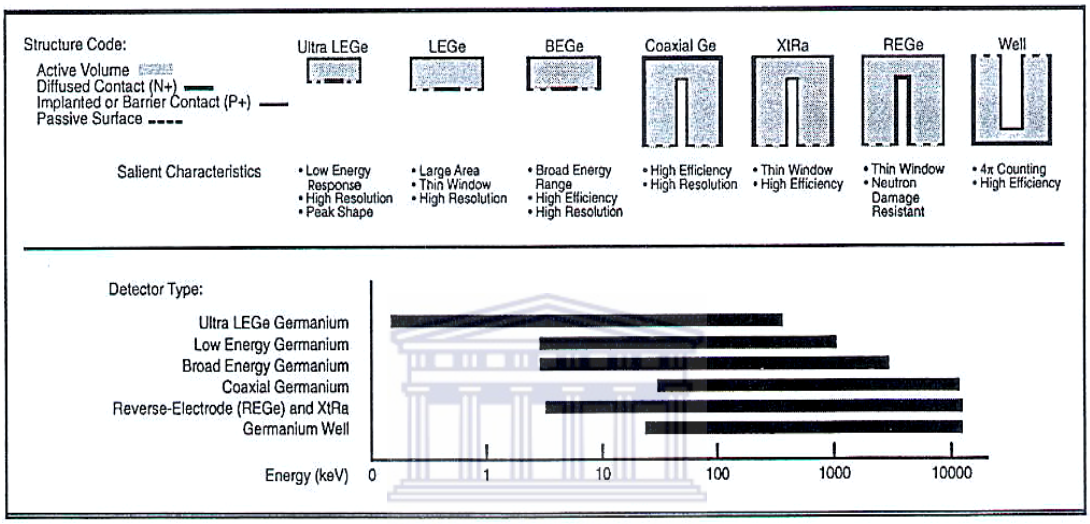

Figure 3.13: Germanium detector geometries (Ge-USR, 1998).

3.9 Technical specifications of the HPGe gamma-ray detector at Environmental Radioactivity Laboratory (ERL), iThemba LABS

The HPGe detector at iThemba LABS (ERL) is a closed-end coaxial Canberra p-type detector (model GC4520) with a built-in preamplifier. This detector has a crystal diameter of 62.5 mm and a length of 59.5 mm and has 45% relative efficiency at 1.33 MeV with 2.1 keV Full Width-at-Half Maximum (FWHM) energy resolution at 1332 keV. The cool-down time is 6 hours and it has a cryostat liquid nitrogen consumption rate of < 1.8 litres per day. Like all other germanium detectors, it has a net impurity level of about 10^{10} atoms/cm^3 so that with the moderate reverse bias the entire volume between the electrodes is depleted and the electric field extends across the region (Ge-USR, 1998).

3.9.1 HPGe gamma-ray detector system set-up at iThemba LABS

The HPGe crystal is set to face upward and mounted to a vertical dipstick cryostat which contains a detector vacuum chamber with a dipstick-like cold finger which is inserted into the neck of the Dewar (double walled vacuum-insulated vessel). A cryostat consists of a vacuum chamber that houses the detector element plus a Dewar for liquid nitrogen cryogen. The liquid nitrogen causes any moisture in the system to freeze. This process helps to maintain the vacuum and is termed cryogenic pumping (Ge-USR, 1998). A capacity of about 20 litres of liquid nitrogen is weekly filled in ERL HPGe detector Dewar, so as to keep the detector operating at liquid nitrogen temperatures. Any increase of the temperature in the system can cause the preamplifier to short out and the semiconductor detector may be harmed.

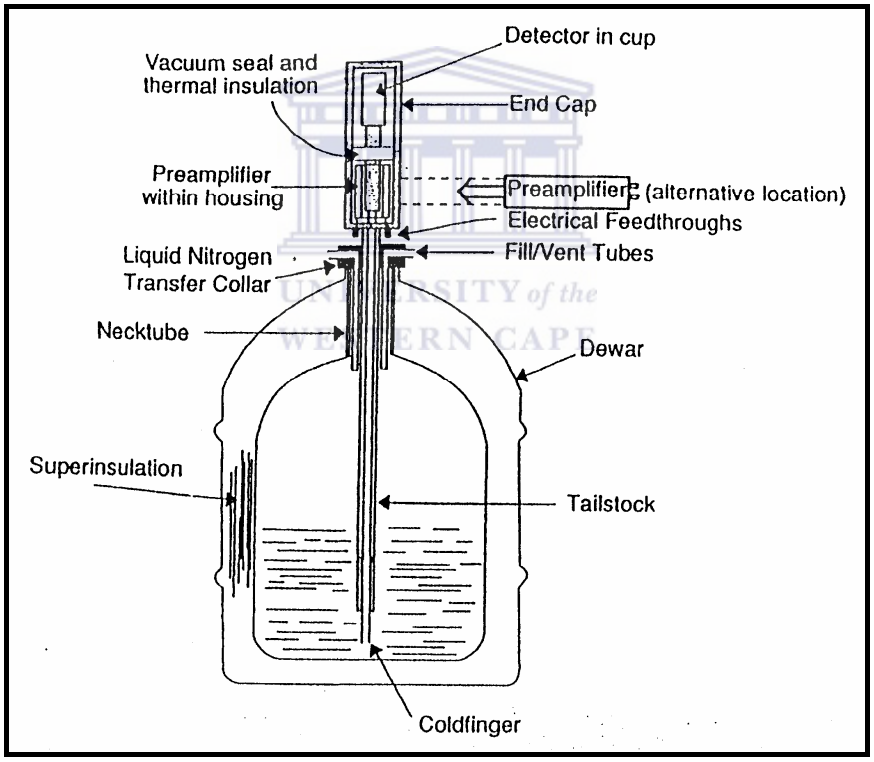

Figure 3.14: A germanium detector, cryostat and liquid nitrogen reservoir (Dewar) (Ge-USR, 1998).

For the purpose of reducing the background radiation during the measuring period, the detector is placed inside a shield comprising of lead (outside, to reduce background radiation from building materials and cosmic rays) and a copper layer

(inside) with ~10 cm and ~2 mm thickness, respectively (see Figure 3.15). Figure 3.17 shows a picture of the HPGe detector system from the outside view, with lead castle around it, and a liquid nitrogen Dewar. Lead is the most used material in shielding of detectors. This is due to its high density and large atomic number and the ease with which it can be stacked. A standard 25% (relative efficiency) detector in a 10 cm thick lead shield can reduce the environmental background by a factor of 100 (Maphoto, 2004). The main function of employing a copper layer inside is to absorb or attenuate any fluorescence X-rays emanating from the lead outer shield and prevent them from reaching the detector. Figure 3.16 shows the HPGe detector with a Marinelli beaker on top of it. A picture showing the experimental setup is shown in Figure 3.18.

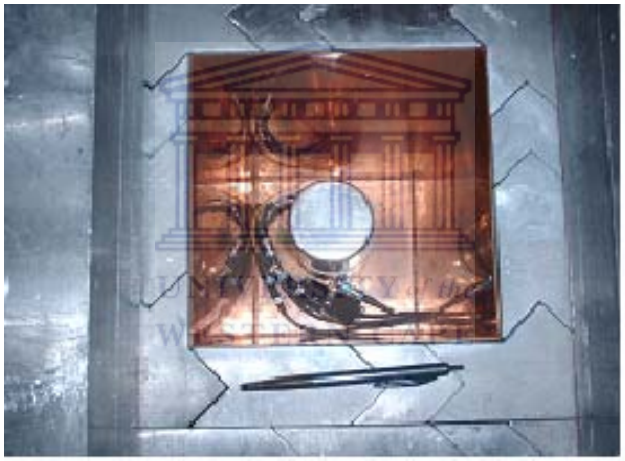

Figure 3.15: Picture showing a top view of HPGe inside the shielding material. The detector is without a Marinelli beaker on top of it.

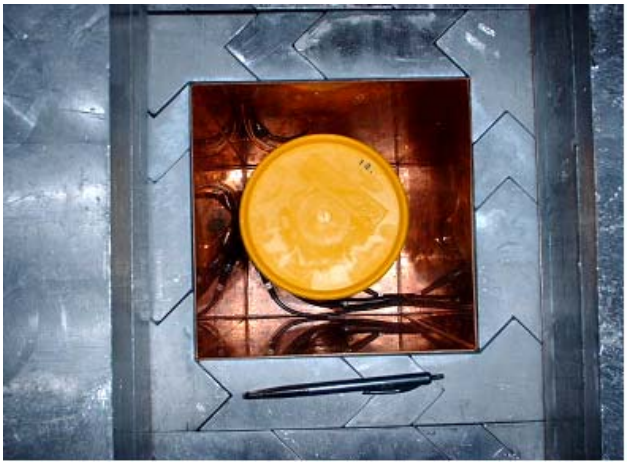

Figure 3.16: Top view picture of HPGe detector with the Marinelli beaker on top of it.

Figure 3.17: A picture showing the HPGe detector from the outside (front view) with lead castle around it and liquid nitrogen Dewar.

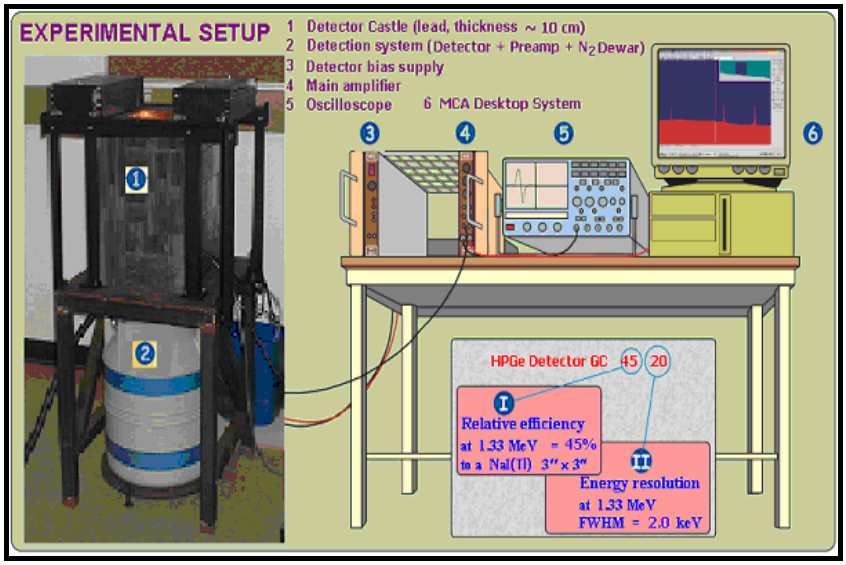

Figure 3.18: Experimental setup of the HPGe gamma-ray spectrometry system at iThemba LABS.

- **Electronics**

The schematic diagram showing electronics of the HPGe γ-ray spectrometer is shown below (Figure 3.19). The system consists of a detector bias supply (SILENA model 7716), preamplifier (model 2002CSL), amplifier (model ORTEC 572), multi-channel analyzer (Oxford-Win) and a desktop computer.

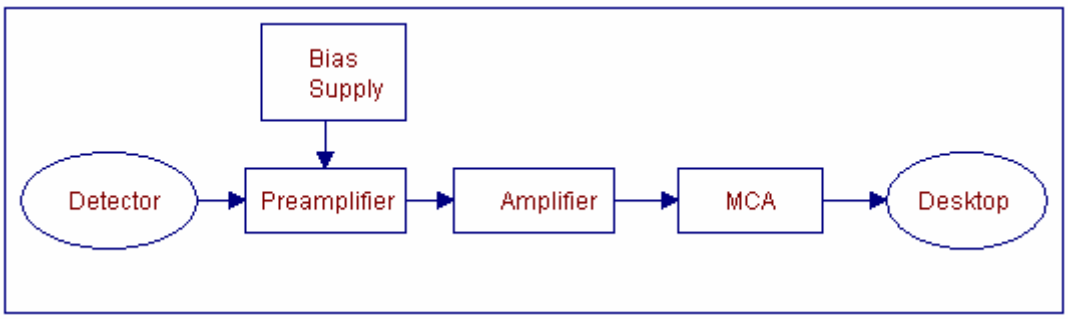

Figure 3.19: Schematic diagram of the electronics of the HPGe detector.

- **Preamplifier**

Before the signal is amplified, it is supplied to the pre-amplifier, whose main function is to interface the detector to the amplifier. It supplies a high impedance load for the detector and low impedance source for the amplifier (Gilmore, 1995). This preamplifier is designed for high-resolution gamma-ray spectroscopy and is a low noise and high-speed preamplifier. Preamplifiers in general can have various modes of operation. The ERL HPGe detector has a built-in preamplifier (model 2002CSL). This is an advantage because the preamplifier is cooled together with the detector, thus reducing the electronic noise and increasing energy resolution.

- **Bias voltage**

The bias voltage supply is connected to the preamplifier and it provides voltage to the detector via the preamplifier. Bias voltage provides the electric field to sweep the charge formed in the detector to be collected by the preamplifier. It is convenient to supply the bias supply to the preamplifier with a coaxial cable as this cable is designed to withstand high voltages (Ge-USR, 1998). The voltage provided by the bias supply to the detector is required to collect all the charges formed in the detector produced by the gamma-rays interacting with the detector material.

- **Amplifier and Multi-Channel analyzer (MCA)**

From the preamplifier, the signal goes to the amplifier (model ORTEC 572), which has a function of shaping pulses coming from the preamplifier and also reducing pile-up. These two functions are important for producing an ideal pulse shape for measurements.

Pulses from the amplifier are supplied to the Oxford Win-Multi-channel analyzer (MCA), which consists of an analog-to-digital convector (ADC), digital spectrum stabilizer (DSS), single channel analyzer (SCA) and multi-channel scalar (Oxf97). The function of the MCA is to sort the linear pulses according to their pulse height, the pulse height being proportional to the gamma energy deposited in the detector. ADC converts pulse heights produced by the amplifier, which are coming in an analog form, to a digital form. Finally, all the digitized pulse heights are stored as a

spectrum containing counts and channels in the OXWIN-MCA software. A diagram describing a basic architecture of a MCA is shown below:

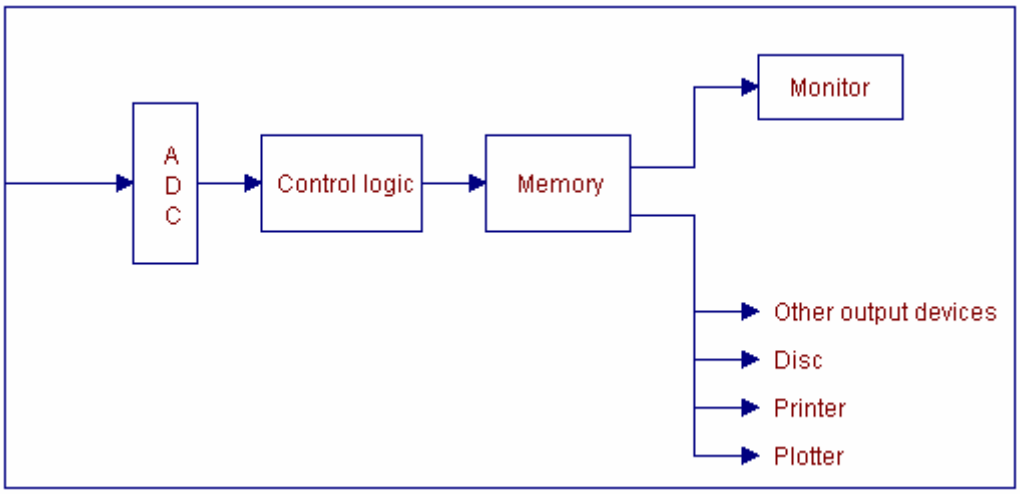

Figure 3.20: Basic architecture of the MCA (Maphoto, 2004).

3.10 Energy line selection

Natural radionuclides of relevance to this work are mainly γ-ray emitting nuclei in the decay series of ^{232}Th and ^{238}U, and ^{40}K. Potassium (^{40}K) was measured from the ^{40}Ar γ-ray: 1460.8 keV (see Figure 3.4 to 3.6). ^{232}Th and ^{238}U are not directly γ-ray emitters, but it is possible to measure γ-rays of their decay products (see the grey boxes in the decay series of ^{232}Th and ^{238}U in Figure. 3.4 and 3.5). Decay products for ^{238}U (^{214}Pb: 295 and 352 keV; ^{214}Bi: 609 and 1120 keV; ^{234}Pa: 1001 keV) and ^{232}Th (^{228}Ac: 338.2 and 911 keV; ^{212}Pb: 239 keV; ^{212}Bi: 727 keV and ^{208}Tl: 583 keV) were used by assuming the decay series to be in secular equilibrium (Firestone, 1996). Weighted averages of several decay products were used to estimate activity concentrations of ^{238}U and ^{232}Th. The natural abundance of ^{235}U is only 0.72% of the total uranium content and hence was not considered in the present study.

3.11 Energy calibration

Energy calibration is often done before the acquisition of the spectrum as part of the setting-up procedure. The main purpose of energy calibration is to derive a

relationship between position of the peak in the Multi-Channel Analyzer (MCA) spectrum and relevant gamma-ray energy. The energy calibration procedure includes

- measuring the spectrum of a gamma-ray emitting source with a precisely known energy,
- deciding which peaks to analyse, and
- using the precisely known gamma-ray energies (for the source).

At iThemba LABS the Environmental Radioactivity Laboratory (ERL) uses Oxford Win-Mutli-channel analyzer (OXWIN-WIN MCA) computer software which is capable of allowing the user to specify the energy associated with each relevant centroid channel corresponding to a particular region of interest. However, to perform energy calibration, a calibration source with enough energies to cover the region of interest required for a specific study is important.

3.11.1 Energy calibration at iThemba LABS

At iThemba LABS the system is calibrated weekly with an IAEA reference material, Thorium Ore (RGTh-1). The photo peak energy (E) is represented as a linear function of channel number (Channel no.)

$$E = B^{*}(\text{Channel no.}) + E_0 \qquad (3.21)$$

The regions of interest (ROI) are manually set on the spectrum. The parameters B and E_0 are determined by using least-squares fit to the calibration points, and corresponding to the gradient and intercept of the calibration line. In the MCA system, one is able to specify the energy associated with each relevant centroid channel corresponding to a particular region of interest

3.12 Activity concentration calculation

The activity concentrations of radionuclides are calculated from the intensity of each gamma-ray line taking into account the mass of the sample, efficiency of the detector, branching ratio of each gamma-ray line (statistical chance that a gamma-ray

is emitted per decaying nucleus) and measuring time. The basic equation used to calculate the activity concentration, $Ac(Bq/kg)$ of a sample in analysis of gamma-ray spectra is given by:

$$Ac = \frac{C_n}{mTB_r\varepsilon_{\det}} \tag{3.22}$$

where, C_n is the photo-peak counts (net counts) associated with the decays of ^{232}Th, ^{238}U and ^{40}K, which is given by subtracting background counts from the sample counts, m is the mass of the sample in kilograms (kg), T is the live time of the spectrum acquisition (in seconds), B_r is the branching ratio (or intensity) associated with each γ-ray decay and $\varepsilon_{\det}$ is the full-energy peak detection efficiency at each specific γ-ray energy. The photo-peak C_n is obtained by setting a window around the peak of interest, which is called the region of interest. Then, the computer uses the Oxford-Win MCA software program to calculate the net counts in a selected photo-peak. And then finally, C_n including the subtraction of background can be calculated using the expression:

$$C_n = (C_g - C_c) - \left(\frac{L_c}{L_b}\right)C_b \tag{3.23}$$

where C_g is the gross counts, C_c is the counts in the continuum and C_b is the background counts; L_c and L_b are live-time of a sample and background live-time, respectively.

Assuming radioactive secular equilibrium between parent and daughter nuclides for (^{232}Th and ^{238}U) in each sample equation (3.22) was used to determine the activity concentration of ^{232}Th and ^{238}U by using lines 238.6 keV (^{212}Pb), 338.2 keV (^{228}Ac), 583 keV (^{208}Tl), 727.3 keV (^{212}Bi) and 911.2 keV (^{228}Ac) for ^{232}Th and 295.1 keV (^{214}Pb), 352 keV (^{214}Pb), 609.3 keV (^{214}Bi), 1001 keV (^{234}Pa) and 1120.3 keV (^{214}Bi) for ^{238}U. These decay products were used to calculate the weighted average activity concentrations of ^{238}U and ^{232}Th.

Since ^{40}K is a gamma-ray emitter, it was identified and quantified through the gamma-ray line 1460.8 keV (^{40}Ar). However ^{228}Ac, a daughter nuclide of ^{232}Th,

produces 1459.2 keV gamma rays, which interferes with ^{40}K (1460.8 keV). In this case, the counts contributed by the ^{228}Ac radionuclide were subtracted, assuming the ^{232}Th series to be in equilibrium. But when thorium content is very high, it becomes difficult to determine the ^{40}K content accurately. The photo-peak (full-energy peak) detection efficiency is very important in determining the activity concentration of a given gamma-ray energy and is discussed below.

3.13 Gamma-ray detection efficiency calibration

Calibration of efficiency is the first step to achieve results that are reliable and have low errors in activity concentration of low-level activity samples. The efficiency (ε_γ) of a detector is the response of a detector when γ-rays emitted by a radioactive material interact with its crystal. Detector efficiency can also be defined as the probability that gamma-ray energy E_γ is completely absorbed in the active volume of the detector. Efficiency varies with energy, and a full calibration of a detector needs the energy/efficiency relationship to be determined (Gilmore, 1995). However, since the main idea in gamma-ray spectroscopy is to relate the peak efficiency in a spectrum to the amount of radioactivity it represents, absolute full-energy peak efficiency is needed. This demonstrates a connection between the number of gamma-rays emitted and the peak area. This depends on the geometrical arrangement of the source and detector.

The energy of a γ-ray that is fully absorbed by the detector results in a peak that appears on the spectrum and is called the full energy peak (FEP). The full energy peak efficiency is the ratio between the number of counts in the net area of the full energy peak to the number of photons of that specific energy emitted by a source with specific characteristics for a given source-to-detector distance. The full-energy-peak efficiency can be calculated by:

$$\varepsilon = R/(S * P_\gamma) \qquad (3.24)$$

where R is the full-energy peak count rate in counts per seconds. P_γ is gamma-ray branching ratio abundance; S is source strength in Becquerel (Bq). The use of Marinelli beakers increases the full-energy peak efficiency. In low-level radioactivity

measurements at close geometry, much care has to be dedicated to efficiency calibration of the spectrometer used. This is because FEP efficiency is a complicated function of many parameters, such as the energy of the gamma-ray, the dimensions of the detector, the dimensions of the source, the geometry arrangement of the detector and the source and the density of the sample (Sharshar et al., 1997).

3.13.1 The KCl Efficiency calibration approach

The detection efficiency was determined by first calculating the relative efficiency using ^{238}U and ^{232}Th lines and plotting the relative efficiency curve. Relative efficiencies were calculated by first assuming radiometric secular equilibrium in the decay chains of ^{238}U and ^{232}Th (Croft et al., 1999). From the activity concentration equation (3.22), for each energy line, C_n/B_r was used to determine relative efficiency while the other terms were kept constant since the activities should be the same for the uranium and thorium lines respectively, and the time and mass is the same.

For uranium, the relative efficiencies were found by normalizing the ratio of the photopeak counts for each gamma-ray line to the associated branching ratios with the 352 keV energy line in the ^{238}U decay chain. And for thorium, the same strategy as in uranium was followed but relative to the 338.2 keV line in the ^{232}Th decay series. Table (3.2) shows the ^{238}Th, ^{238}U and ^{40}K gamma-ray lines used and their branching ratios. The 186 keV line was adjusted to take into account the doublet due to $^{238}U/^{235}U$ and similarly for the 967 keV doublet due to ^{228}Ac.

Table 3.2: The gamma-ray energy lines used to determine the detection efficiency and their associated branching ratios (Firestone, 1996).

^{238}U	keV	Branching ratios
	186.1	0.062[2]
	295.1	0.185
	352.0	0.358
	934.4	0.030
	1238.1	0.059
	1377.7	0.039
	1764.5	0.154
	2204.1	0.049
^{232}Th		
	338.4	0.113
	727.3	0.066
	794.8	0.043
	860.3	0.045
	911.2	0.266
	968.0[3]	0.213
^{40}K		
	1461.0	0.107

Relative efficiencies obtained were fit with the function of the form

$$\varepsilon = a\left(\frac{E}{E_0}\right)^b \tag{3.25}$$

where ε is the efficiency, E is the gamma-ray energy in keV, (E_0 = 1 keV) with a and b being fit parameters. When taking the logarithm of the above equation (3.25) one obtains:

$$\ln\varepsilon = \ln a + b\ln\frac{E}{E_0} \tag{3.26}$$

Using the obtained data for relative efficiency of ^{238}U and ^{232}Th, equation (3.25) was again used to determine the relative efficiencies of all energy lines in Table

[2] Adjusted to take into account doublet at 186 keV due to ^{235}U
[3] The average energy of the 965 and the 969 keV lines (^{228}Ac). The branching ratio was obtained by summing respective branching ratios

3.2 (from ^{238}U, ^{232}Th and (1461 keV) ^{40}K), and parameters *a* and *b* were again determined. At this point the final relative efficiency was obtained.

The second step was to calculate the absolute efficiency value at 1461 keV of ^{40}K from a KCl standard source. The activity concentration of ^{40}K was determined using the formula:

$$A = \lambda N \tag{3.27}$$

where A is the activity, with the decay constant λ and N the number of ^{40}K nuclei in KCl. N is obtained by calculating the number of moles in the KCl and multiplying it with Avogadro's number (N_A = 6.022 x 10^{23} mol^{-1}). This can be symbolically represented as:

$$N = nN_A a \tag{3.28}$$

with a being the abundance, and n given by:

$$n = \frac{m}{M} \tag{3.29}$$

where m is the mass of the KCl (1000 g) source and M is the molar mass (74.551 g/mol) that is contained in 1000 g of KCl (Croft et al., 1999). The decay constant (λ) is given by $\frac{\ln 2}{t_{1/2}}$, where $t_{1/2}$, the half-life of ^{40}K is 1.277 x 10^9 y.

The ^{40}K absolute full-energy peak detection efficiency is then calculated using the expression,

$$\varepsilon_{1461} = \frac{C_{1461}}{mTB_r Ac} \tag{3.30}$$

where C_{1461} is the net count in the 1461.0 keV peak (with the background counts subtracted).

The absolute detection efficiency obtained is then divided by the relative efficiency at 1461.0 keV, so as to yield a numerical factor required to convert relative

efficiencies from ^{232}Th and ^{238}U to absolute efficiencies. After the above procedure, the energy versus absolute efficiency curve is plotted and parameters *a* and *b* produced in the plot. A figure summarizing the steps that are followed when calculating absolute efficiency using the above procedure is presented below (Modisane, 2005).

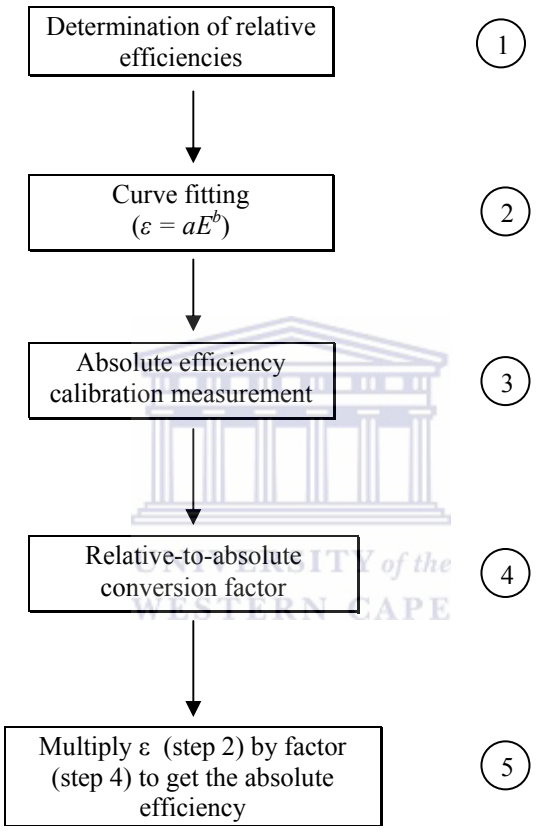

Figure 3.21: Flow Chart showing the gamma-ray detection efficiency determination procedure (Modisane, 2005).

The procedure above was carried out for ten so as to obtain more parameters (*a* and *b*), and their average was then used during the calculation of the activity concentration. Examples illustrating the determination of absolute efficiencies are shown below. The first example is the determination of absolute efficiencies using the Marinelli beaker that has a mass of approximately 180 grams. The efficiencies obtained were used for calculation of the activity concentrations of the bulk sand samples. The second example is the calculation of the absolute efficiencies using a

smaller vial with a volume of approximately 93.7 cm^3. This smaller container was used for measuring activity concentration of different grain-size fractions.

3.13.1.1 Determination of the Absolute detection efficiency of a sample measured using a Marinelli beaker

A sample from Melkbosstrand beach (Mbs depth) was measured with an HPGe detector and relative efficiencies were determined using equation 3.22. Using equation (3.26), the fit parameters (*a* and *b*) were determined. A straight line graph of ln(Energy) versus ln(Relative efficiency) with parameters ln (*a)* and *b* is presented in the figures below (Figure 3.21 and 3.24) for energy lines associated with ^{238}U and ^{232}Th, respectively. The parameters together with efficiencies of thorium were used to find a factor required to join thorium relative efficiencies to uranium relative efficiencies. Figure 3.25 shows the plot of energy (keV) versus relative efficiency curve of ^{238}U + ^{232}Th with a set of parameters, respectively.

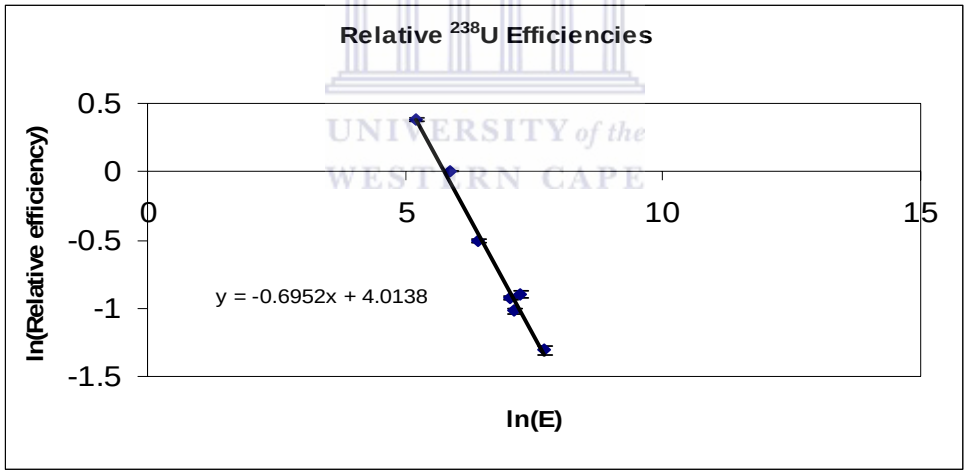

Figure 3.22: Linear graph showing the relative efficiency determined from ^{238}U lines and parameters ln(a) and b, (-0.6952) and (4.0138), respectively, for the Melkbosstrand sand sample (Mbs depth). Values were normalized relative to the 352.0 keV value.

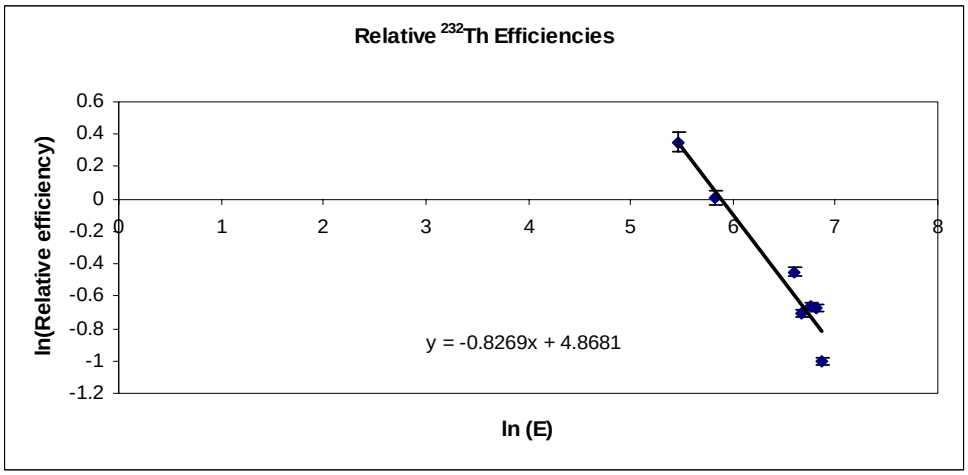

Figure 3.23: Linear graph showing the relative efficiency determined from ^{232}Th lines and parameters ln(a) and b, (-0.8269) and (4.8681), respectively, for the Melkbosstrand sand sample (Mbs depth). Values were normalized relative to a 338.0 keV value.

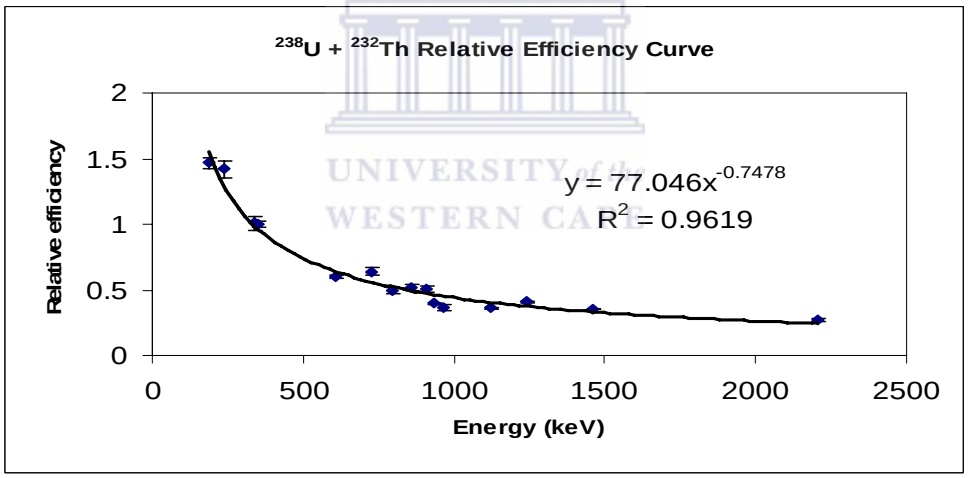

Figure 3.24: Relative efficiency curve determined from ^{238}U + ^{232}Th lines with parameters a and b given as 77.046 and -0.7478, respectively, from the Melkbosstrand sand sample (Mbs depth).

Following the last step from Figure 3.21, the KCl standard source of mass 1.2908 kg was measured in a 1 litre Marinelli beaker. The value for activity concentration of KCl was obtained to be 20983 Bq/kg. The absolute efficiency of the 1461 keV energy line and the conversion factor were obtained. Figure 3.25 shows a typical absolute efficiency curve plotted for sample Mbs depth.

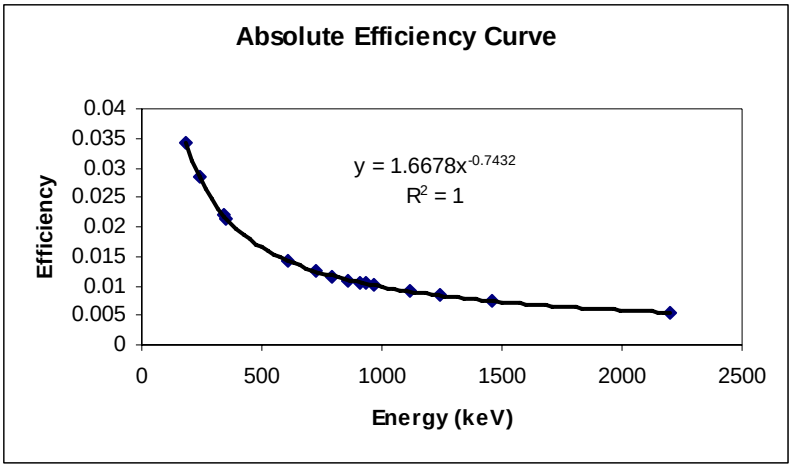

Figure 3.25: Graph showing absolute efficiency curve for the energy lines associated with ^{238}U, ^{232}Th and ^{40}K decay found for the Malkbosstrand sample (Mbs depth). The parameters a and b are (1.6678) and (-0.7432).

3.13.1.2 Determination of Absolute detection efficiency of a sample measured using a filled medium vial

Efficiency calibration of a medium vial was performed using the same procedure as for the Marinelli. The vial was filled with a sand sample and sealed properly and then measured with an HPGe detector for 55642.23 seconds. Relative efficiencies were obtained using the same formulas, energy lines and procedure as in the above example. Linear graphs of ln (Energy) versus ln (Relative efficiency) with parameters *a* and *b* are presented in the figures below (Figure 3.26 and 3.27) for energy lines associated with ^{238}U and ^{232}Th, respectively. Figure 3.28 shows the plot of energy (keV) versus relative efficiency curve determined from ^{238}U + ^{232}Th energy lines, with a set of parameters, respectively.

A KCl standard source was filled in the medium vial so that it can have the same geometry as the sample, and it was measured with the HPGe detector for 64939.92 seconds. The mass of the KCl in the medium vial was measured to be 0.11 kg. Since the activity concentration of KCl mass of 1.29 kg measured win a Marinelli was calculated, it was then easy to calculate the activity of the KCl measured using the medium vial. Using equation 3.30, the absolute efficiency was calculated. The obtained absolute detection efficiency was then divided by the relative efficiency at 1460.8 keV, so as to yield a factor required to convert relative efficiencies from ^{232}Th

and ^{238}U to absolute efficiencies. After the above procedure, the energy versus absolute efficiency curve was plotted and parameters *a* and *b* were produced in the plot.

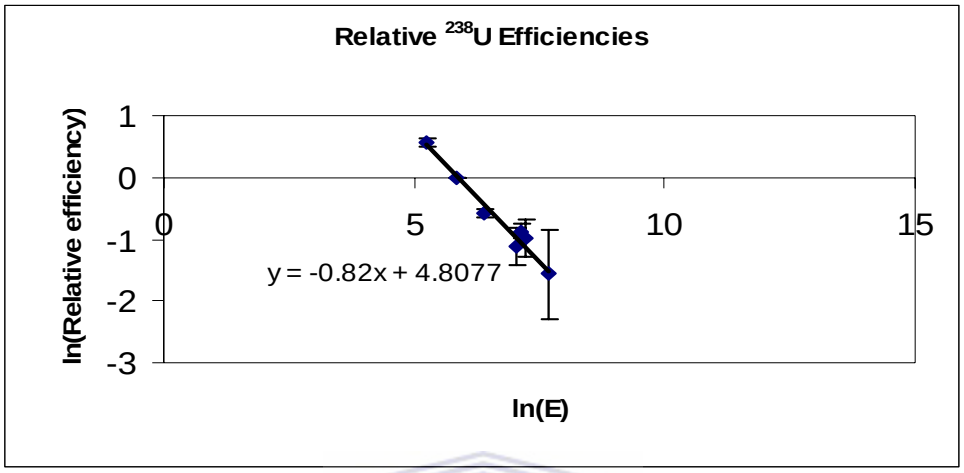

Figure 3.26: Linear graph showing the relative efficiencies for the medium vial determined from ^{238}U lines and parameters ln(a) and b, (-0.82) and (4.8077), respectively, for the Melkbosstrand sand sample (Mbs 3). Values were normalised relative to a 352.0 keV value.

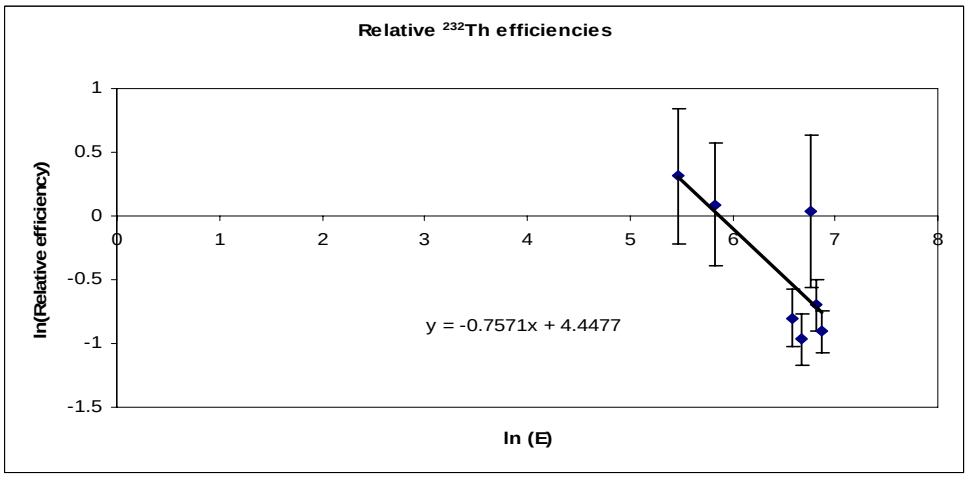

Figure 3.27: Linear graph showing the relative efficiencies for the medium vial determined from ^{232}Th and parameters ln(a) and b, (-0.757) and (4.4477), respectively, for the Melkbosstrand sand sample (Mbs 3). Values were normalised relative to a 338.0 keV value.

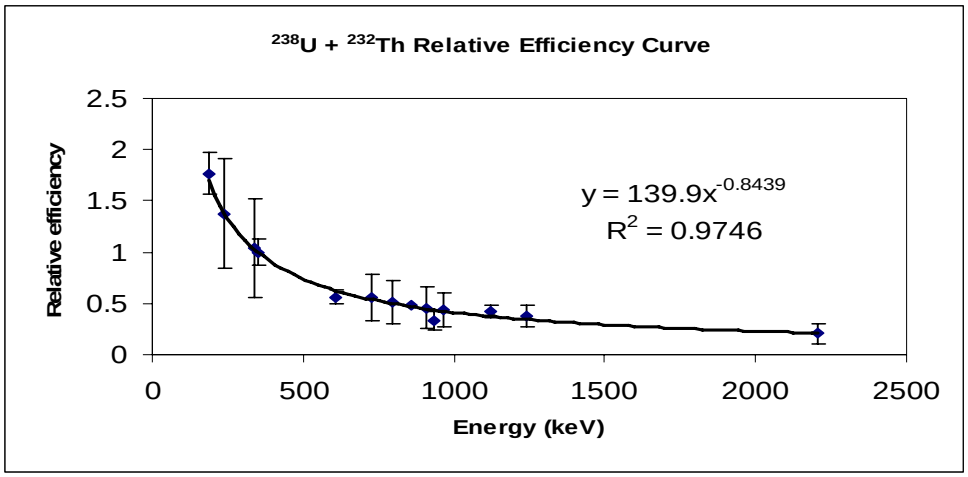

Figure 3.28: Relative efficiency curve for the medium vial determined from (^{238}U + ^{232}Th) lines with parameters a and b given as 139.9 and -0.8439, respectively, from the Melkbosstrand sand sample (Mbs 3).

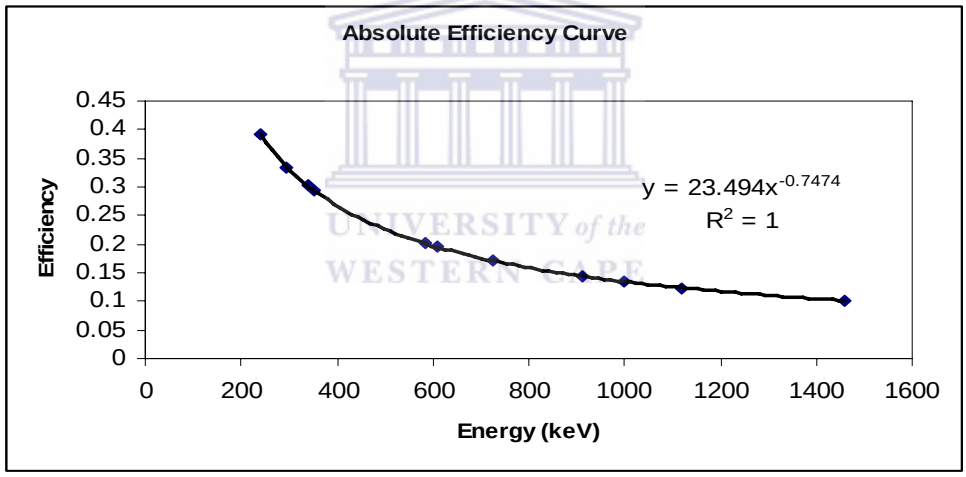

Figure 3.29: Absolute efficiency curve for the medium vial for (^{238}U + ^{232}Th + ^{40}K) lines with parameters a and b given as 23.49 and 0.7474, respectively, calculated from sample (Mbs 3).

The uncertainties in the curves plotted for a smaller container are very large (see Fig. 3.26 to 3.28) compared to the bigger container (Marinelli beaker). This is because a Marinelli beaker was designed to cover the largest part of the active volume of the detector and thus gives good detection efficiency, while the smaller container can only be placed on top of the detector.

3.13.1.3 Determination of Absolute detection efficiency of a sample measured using small vial which is not filled

The determination of absolute detection efficiency of a small vial was determined using a different method from the one used in the Marinelli beaker and medium vial. These efficiencies were used to determine the activity concentration of 90 μm grain-size due to its smaller quantity. When performing grain-size separation of a sand sample with the mass of approximately 2.5 kg, one was able to get only a very small quantity (~ 9.5 grams) of 90 μm grain-size fraction. Thus, a small container (see Figure 2.9) was used to measure this gain-size fraction.

A sample Mbs 3 was used to calculate the absolute efficiency of a small vial. Since the activity concentration of this sample (measured with a Marinelli beaker) is known, it was then assumed that the sand sample (Mbs 3) placed in the small vial contains the same activity concentration as the one in the Marinelli beaker. The equation 3.22 was used to calculate absolute efficiencies of energy lines in table 3.2, with *m* and *T* being the mass and live time of a sample measured using a small vial. The graph showing the absolute efficiency curve is shown in Figure 3.30.

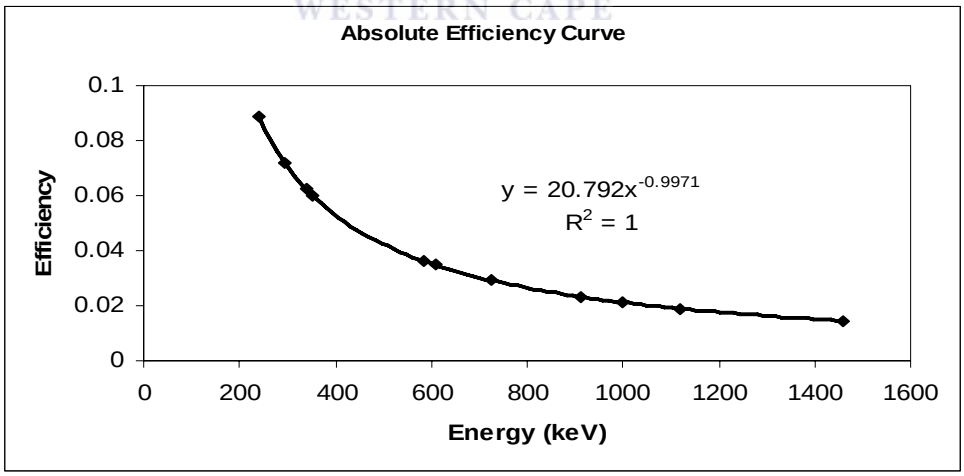

Figure 3.30: Graph showing the absolute efficiency curve for the small vial for ^{232}Th, ^{238}U and ^{40}K radionuclides energies found for the Melkbosstrand sample (Mbs 3). The parameters a and b are 20.792 and -0.9971, respectively.

CHAPTER 4

RESULTS AND DISCUSSIONS

In this chapter the results and its interpretation are discussed. The results for the samples, which were collected parallel and along transects to the coastline are presented. Also, the radiometric analyses of various grain-size fractions obtained by sieving are presented. The provenance characteristics and the associated depositional environment for the Melkbosstrand (MBS) and Ouskip (OSK) group of sand samples are discussed on the basis of radionuclide concentrations.

4.1 HPGe gamma-ray measurements

The energy spectrums shown below (Figure 4.1 to 4.3) were obtained for Background (Marinelli beaker filled with 1 litre tap water), sample Mbs 9 (some of sample with low activity concentration) and Mbs depth (sample with high activity concentration). These spectrums are an example of a typical spectrum obtained from HPGe gamma-ray spectrometry. The labeled energy peaks are 238.6 keV (^{212}Pb), 338.2 keV (^{228}Ac), 583 keV (^{208}Tl), 727.3 keV (^{212}Bi) and 911.2 keV (^{228}Ac) from a parent radionuclide (^{232}Th) and 295.1 keV (^{214}Pb), 352 keV (^{214}Pb), 609.3 keV (^{214}Bi), 1001 keV (^{234}Pa), 1120.3 keV (^{214}Bi) from a parent radionuclide (^{238}U) and 1460.8 (^{40}K).

There is noticeable difference between the three spectrums. The background spectrum shows a very law count rate (range 0 – 0.03 counts/s) due to very low activity concentration. The count rate for sample Mbs 9 (some of sand sample with low activity concentration) ranges from 0 – 0.09 counts/s. Sample Mbs depth contains a very high count rate (range = 0 – 3.18 counts/s) due to high activity concentration. The results showing the activity concentration of ^{232}Th, ^{238}U and ^{40}K are show in Table 4.3 and 4.4.

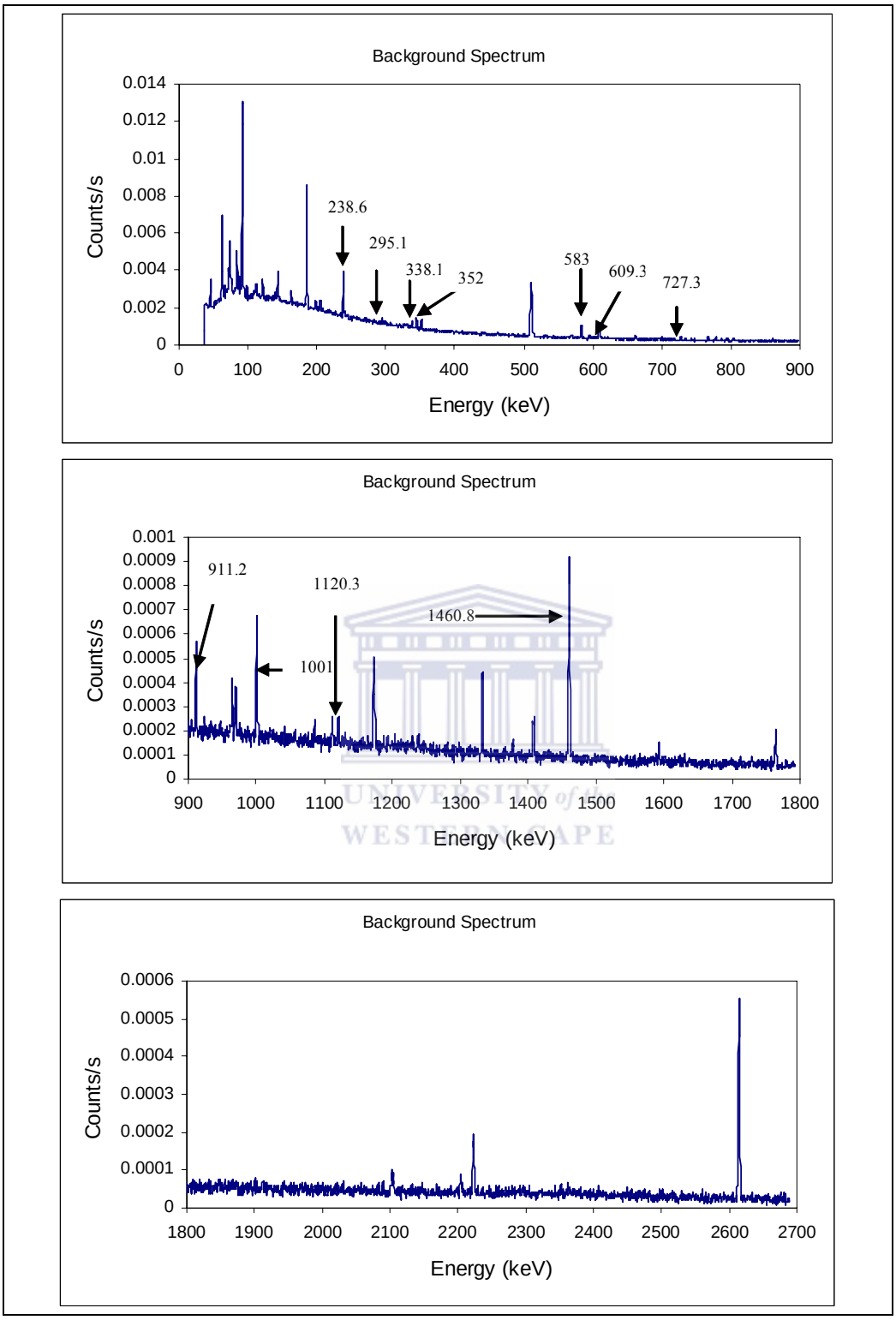

Figure 4.1: The background spectrum (range = 0 - 2700) measured using a Marinelli filled with 1litre tap water. In this spectrum, some of energy peaks associated with daughter radionuclides and nuclei in the decay series of ^{232}Th, ^{238}U and ^{40}K are labeled. The spectrum was measure for 591992 seconds.

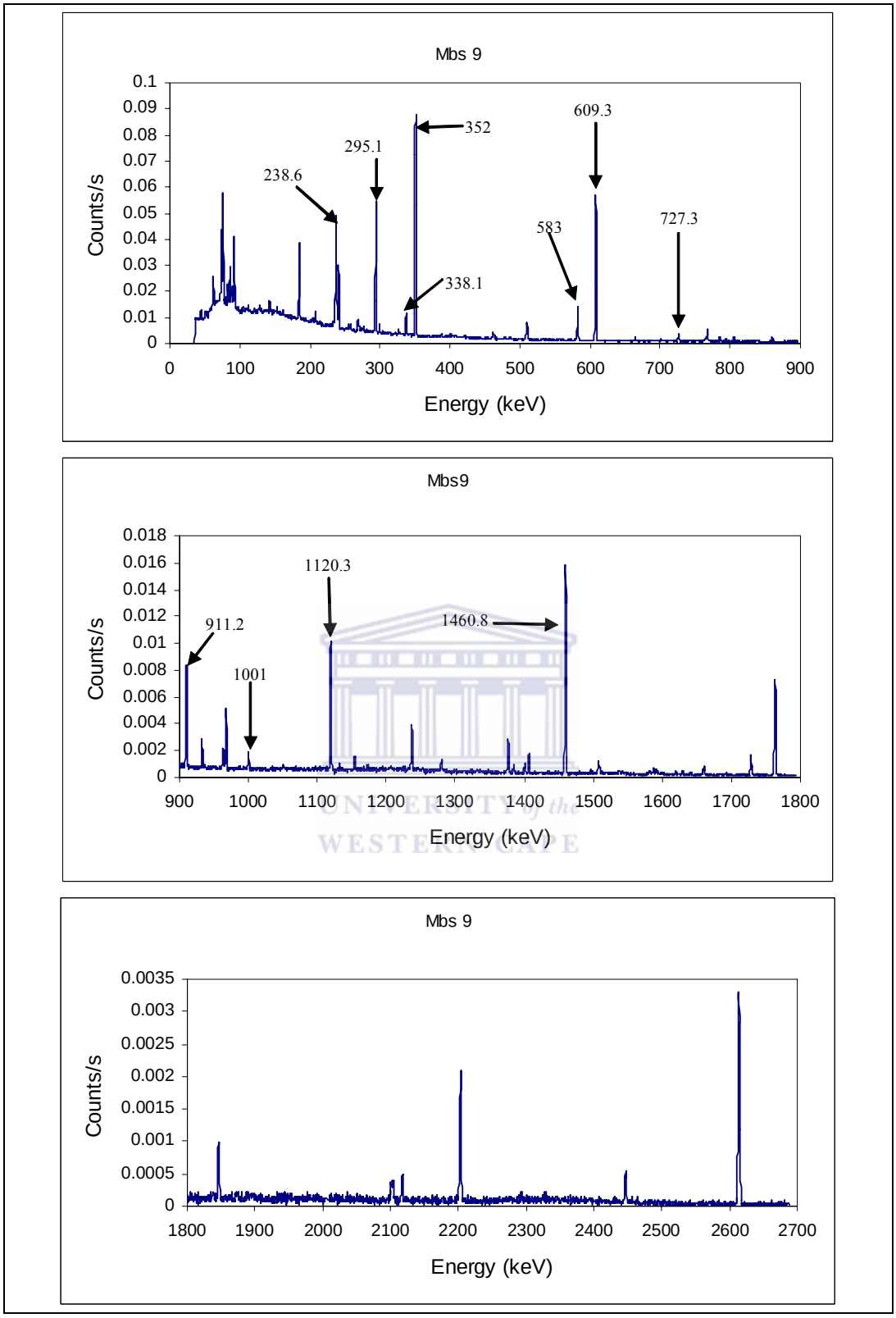

Figure 4.2: The spectrum (range= 0 - 2700) of sand sample (Mbs 9) collected from Melkbosstrand. In this spectrum, some of gamma-ray energy peaks associated with daughter radionuclides and nuclei in the decay series of ^{232}Th, ^{238}U and ^{40}K are labeled. The spectrum was measured for 78044 seconds.

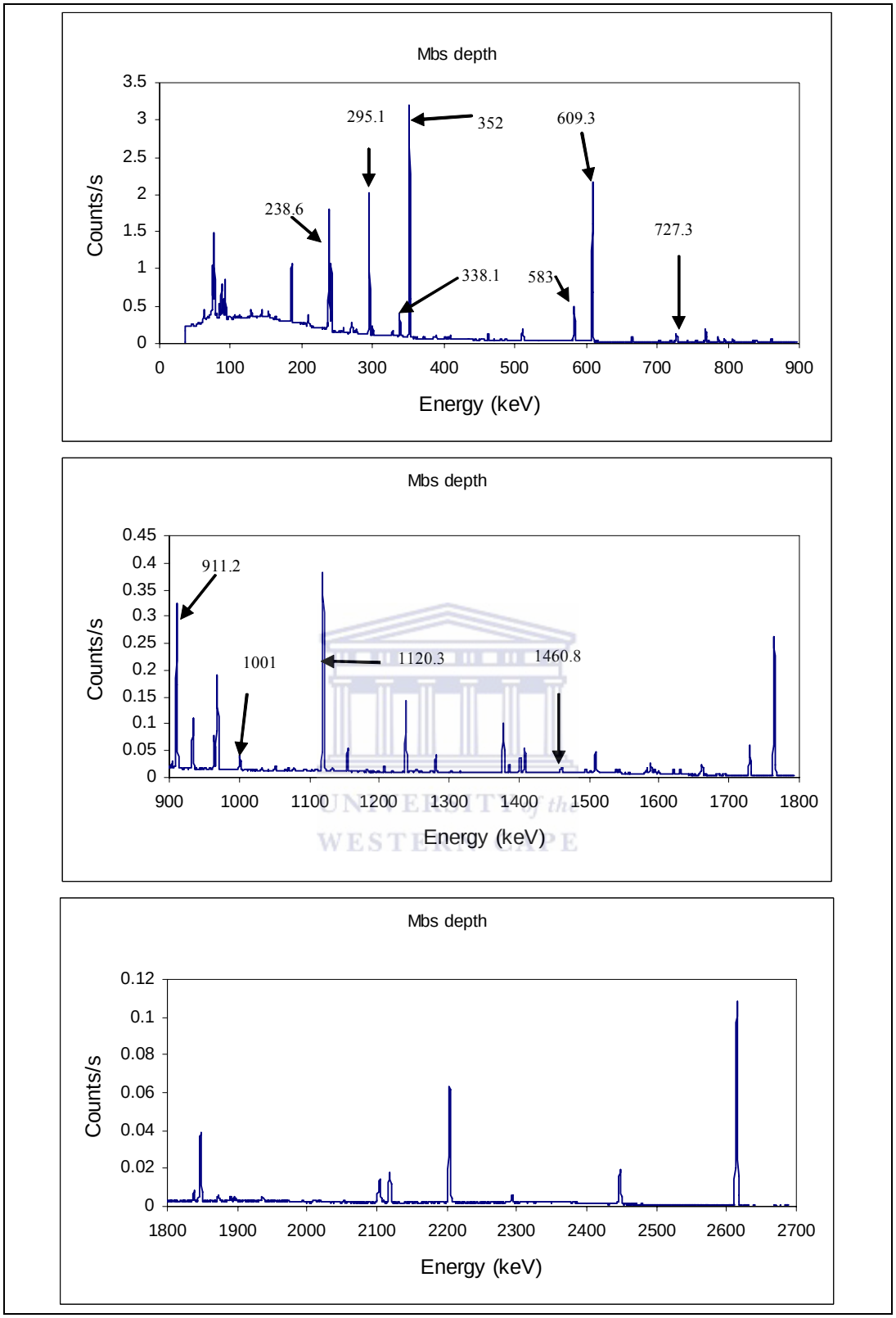

Figure 4.3: The spectrum (range = 0 - 2700) of sand sample (Mbs depth) collected from Melkbosstrand. In this spectrum, some of gamma-ray energy peaks associated with daughter radionuclides and nuclei in the decay series of ^{232}Th, ^{238}U and ^{40}K are labeled. The spectrum was measured for 102703 seconds.

4.2 Inter-comparison of results

For inter-comparison of result the system was calibrated with three IAEA reference materials, such as Thorium Ore (RGTh-1), Uranium Ore (RGU-1) and Soil (Soil-375) and the results were found within the limit of experimental error and shown in (Table 4.1 and 4.2). The IAEA standard reference soil material (Soil-375) has a certified ^{232}Th, ^{238}U and ^{40}K content (95% confidence) of 20.5 ± 1.4 Bq.kg^{-1} 24.4 ± 5.4 Bq.kg^{-1} and 424.0 ± 8.0 Bq.kg^{-1}, respectively (IAEA, 2000). The activity concentrations of the sample materials were calculated using the efficiencies calculated using the relative efficiency method (REF) used in this study.

Table 4.1: Inter-comparisons between activity concentrations calculated using REF method and certified activity concentration of the IAEA soil sample.

Radionuclide	**Recommended Value (Bq.kg^{-1})**	**95% Confidence Interval (Bq.kg^{-1})**	**Present study (Bq.kg^{-1})**
^{232}Th	20.5	19.2 – 21.9	20.9 ± 1.9
^{226}Ra	20.0	18.0 – 22.0	19.9 ± 1.5
^{40}K	424.0	417.0 – 432.0	424.3 ± 6.0

Table 4.2: Inter-comparison results for the IAEA standard samples

Sample	**ERL Results**			**IAEA Results**		
Name	^{232}Th (Bq.kg^{-1})	^{238}U (Bq.kg^{-1})	^{40}K (Bq.kg^{-1})	^{232}Th (Bq.kg^{-1})	^{238}U (Bq.kg^{-1})	^{40}K (Bq.kg^{-1})
RGTh-1	3288 ± 268	81.11 ± 10	-	3250 (3160-3340)	78 (72 - 84)	-
RGU-1	-	5300 ± 425	-	-	4940 (4910 - 4970)	-

In table 4.2 the numbers in the brackets represents the standard deviation associated with the sample concentration and can be estimated from the 95% confidence interval. The analyses of the IAEA-375 standard reference material and

IAEA standard samples (RGTh-1 and RGU-1) (see Table 4.1 and 4.2) show a good agreement between certified values and the values calculated using the REF method.

4.3 Radiometric analyses of samples collected parallel to the coastline

The activity concentrations of bulk sand samples from the Melkbosstrand (MBS) and Ouskip (OSK) beach are presented in the Table 4.3. The activity concentrations of ^{232}Th in units Bq.kg^{-1} varies from 5.5 ± 0.2 to 14.7 ± 0.3 with a weighted mean and standard deviation (w_i mean ± $w_{i\ STDEV}$) of 7.7 ± 3.4 for the MBS beach; and 3.2 ± 0.2 to 4.2 ± 0.3, with a weighted mean and standard deviation (w_i mean ± $w_{i\ STDEV}$) of 3.5 ± 0.3 for the OSK beach, respectively. Figure 4.4 shows that MBS beach samples have higher levels of ^{232}Th concentrations than the OSK samples. The activity concentration of ^{238}U in units Bq.kg^{-1} varies from 19.7 ± 0.9 to 48.6 ± 1.0 with a weighted mean and standard deviation (w_i mean ± $w_{i\ STDEV}$) of 28.4 ± 10.4 for the MBS beach; and 11.1 ± 0.8 to 14.9 ± 1.0 with a weighted mean and standard deviation (w_i mean ± $w_{i\ STDEV}$) of 12.3 ± 1.4 for the OSK beach, respectively. Figure 4.5 shows that MBS beach samples have higher levels of ^{238}U concentrations than the OSK samples. The activity concentration of ^{40}K in units Bq.kg^{-1} varies from 41.1 ± 2.6 to 48.3 ± 3.4 with a weighted mean and standard deviation (w_i mean ± $w_{i\ STDEV}$) of 44.5 ± 2.5 for the MBS beach; and 53.2 ± 4.3 to 64.9 ± 5.6 with a weighted mean and standard deviation (w_i mean ± $w_{i\ STDEV}$) of 58.3 ± 4.2 for the OSK beach, respectively. Figure 4.6 show that OSK beach samples have higher levels of ^{40}K concentrations than the MBS samples.

The Chi-square per degree of freedom (χ_R^2)[4] value for the ^{232}Th, ^{238}U and ^{40}K are 110.7, 95.1 and 0.8 for the MBS beach samples and 2.0, 2.1 and 0.9 for the OSK beach samples. The low χ_R^2 value for the OSK beach samples indicates the distributions of radionuclide concentration are nearly uniform. The higher χ_R^2 value

[4] χ_R^2 (Chi-square per degree of freedom or reduced Chi-square) is the measure of the goodness of fit to the data. In this study χ_R^2 is used to asses the statistical variation of activity concentration in MBS and OSK .The formula to calculate χ_R^2 is given in Appendix B (equation 5B).

for the radionuclides in MBS beach indicates wide distribution of radionuclides activity concentrations. The higher level of uranium concentration indicates possibly more enrichment of heavy minerals and the possible presence of significant concentrations of zircons along the west coast (Macdonald et al., 1997). The ratios of activity concentrations ($^{232}Th/^{238}U$) for the bulk samples yield means (± SD) of 0.29 ± 0.02 and 0.30 ± 0.01 for the MBS and OSK beach, respectively.

The cross plot results for the ^{232}Th, ^{238}U and ^{40}K are presented for the MBS and OSK beach samples. There is a strong correlation between ^{232}Th and ^{238}U in the MBS samples ($R^2 = 0.992$) and a very weak correlation exists between ^{232}Th and ^{238}U in the OSK samples ($R^2 = 0.7931$) (see Figure 4.7). This clearly indicates that radionuclides such as ^{232}Th and ^{238}U are interdependent in MBS samples. The correlation between ^{40}K and ^{238}U is weak ($R^2 = 0.6046$) in the MBS samples, while there is a poor correlation ($R^2 = 0.2893$) in OSK samples (see Figure 4.8). Also, a weak correlation exists between ^{40}K and ^{232}Th in MBS samples ($R^2 = 0.5402$), while there is a very poor correlation in the OSK samples ($R^2 = 0.3308$) (see Figure 4.9). The poor correlation between ^{40}K and ^{232}Th indicates that ^{40}K concentrations may not be related to the presence of ^{232}Th bearing minerals and the results are not dependent on each other. The higher values for the MBS beach samples indicate significant thorium concentrations may be due to the presence of more heavy minerals than in the OSK beach samples.

The higher level of ^{40}K activity concentration observed in OSK group shows more enrichment of lighter minerals such as potash feldspars and quartz sands. The average elemental concentrations of K (%) are 0.15% for the MBS samples and 0.19% for the OSK beach samples, respectively. The elemental ratios such as eTh/eU and eTh/K are 0.88 and 14.34 for the MBS beach and 0.93 and 4.60 for the OSK beach, respectively. The Th/K values are indicative of the presence of heavy minerals in the sand samples (Anjos et al., 2006). This study indicates that the MBS beach has higher concentrations of heavy minerals than the OSK beach samples.

Table 4.3: Radionuclides concentrations of samples collected from Melkbosstrand and Ouskip beach, which are parallel to the shoreline.

Sample Code	^{232}Th (Bq.kg^{-1})	^{238}U (Bq.kg^{-1})	^{40}K (Bq.kg^{-1})	Ratio (^{232}Th/^{238}U)
Samples from Melkbosstrand beach				
Mbs1	8.3 ± 0.4	29.9 ± 1.5	43.3 ± 2.3	0.28 ± 0.02
Mbs2	10.6 ± 0.5	34.5 ± 1.5	46.9 ± 3.7	0.31 ± 0.02
Mbs3	14.7 ± 0.3	48.6 ± 1.0	41.4 ± 2.5	0.30 ± 0.01
Mbs4	14.4 ± 0.4	47.3 ± 1.3	41.1 ± 2.6	0.30 ± 0.01
Mbs5	7.6 ± 0.3	26.7 ± 1.0	47.4 ± 3.2	0.28 ± 0.01
Mbs6	7.0 ± 0.3	24.1 ± 1.1	46.6 ± 3.3	0.29 ± 0.02
Mbs7	6.6 ± 0.3	25.0 ± 1.1	45.1 ± 3.3	0.26 ± 0.02
Mbs8	6.6 ± 0.3	23.1 ± 1.0	48.3 ± 3.4	0.29 ± 0.02
Mbs9	5.5 ± 0.2	19.7 ± 0.9	45.7 ± 3.3	0.28 ± 0.02
Mbs10	5.5 ± 0.2	21.1 ± 0.9	45.5 ± 3.2	0.26 ± 0.02
w_i mean ± Sd	7.7 ± 3.4	28.4 ± 10.4	44.5 ± 2.5	0.29 ± 0.02
Chi-square	110.7	95.1	0.8	
MBS (depth)	210 ± 4	680 ± 10	23.3 ± 1.4	0.31 ± 0.01
Samples from Ouskip beach				
Osk1	3.5 ± 0.2	11.7 ± 0.3	63.5 ± 5.3	0.29 ± 0.03
Osk2	3.3 ± 0.2	11.2 ± 0.8	59.9 ± 4.7	0.30 ± 0.03
Osk3	4.1 ± 0.3	13.8 ± 1.0	59.3 ± 5.1	0.30 ± 0.03
Osk4	3.2 ± 0.2	11.5 ± 0.9	62.7 ± 5.0	0.28 ± 0.03
Osk5	3.6 ± 0.2	11.6 ± 0.8	53.7 ± 4.1	0.31 ± 0.03
Osk6	3.3 ± 0.2	11.1 ± 0.8	64.9 ± 5.6	0.29 ± 0.03
Osk7	4.2 ± 0.3	14.9 ± 1.0	53.2 ± 4.3	0.29 ± 0.03
Osk8	3.6 ± 0.2	13.8 ± 0.9	54.3 ± 4.5	0.26 ± 0.02
Osk9	3.3 ± 0.3	11.7 ± 0.9	57.9 ± 5.3	0.28 ± 0.03
Osk10	3.6 ± 0.3	13.6 ± 0.9	61.4 ± 5.7	0.27 ± 0.03
w_i mean ± Sd	3.5 ± 0.3	12.3 ± 1.4	58.3 ± 4.2	0.30 ± 0.01
Chi-square	2.0	2.1	0.9	

In the sampling spots where samples Mbs1, Mbs2 and Mbs3 were sampled, the sand was observed to be darker than all other sampling spots. In these sand samples, higher activity concentrations of ^{232}Th and ^{238}U were observed (see Fig. 4.4 and 4.5). The darker surface is an indication of the presence of more heavy minerals, which can be proved by a higher activity concentration of ^{232}Th and ^{238}U.

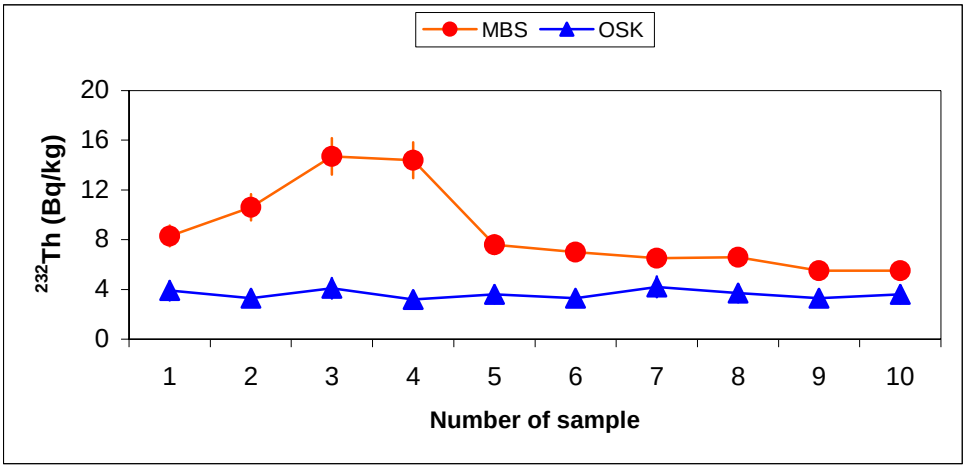

Figure 4.4: The MBS group of samples showing higher levels of ^{232}Th concentrations than the OSK group of sand samples.

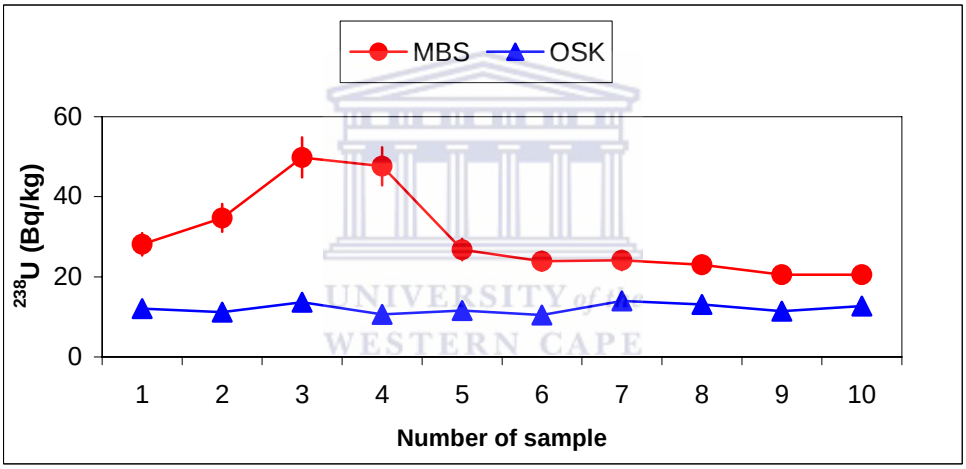

Figure 4.5: MBS group of sand samples showing higher levels of ^{238}U concentrations than the OSK group of sand samples.

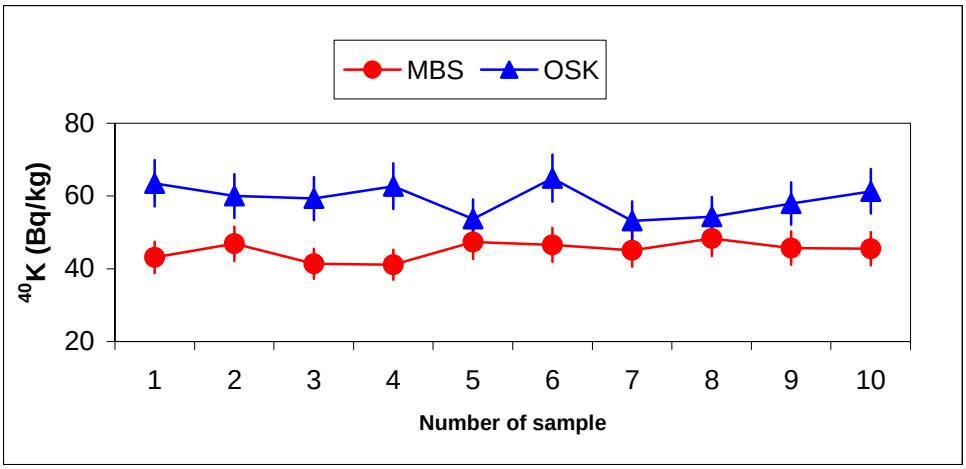

Figure 4.6: OSK group of samples showing higher levels of ^{40}K concentrations than the MBS group of sand samples.

.

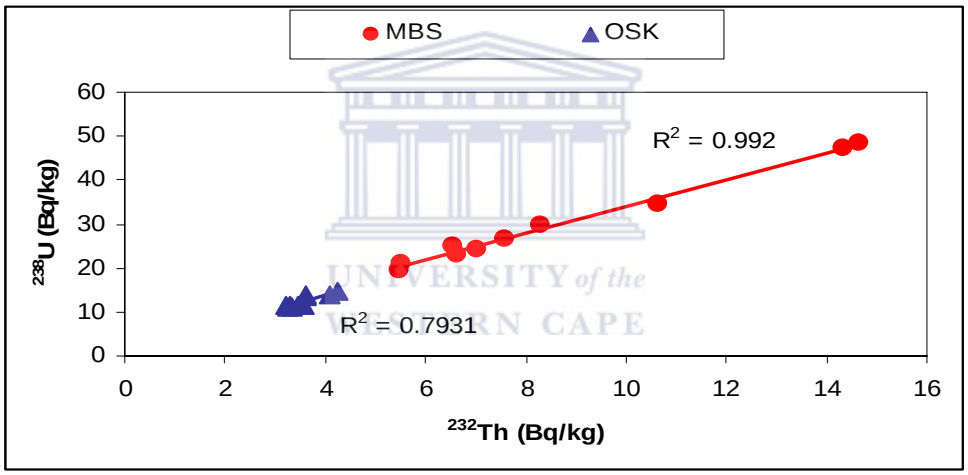

Figure 4.7: Correlations between ^{232}Th and ^{238}U in MBS and OSK samples.

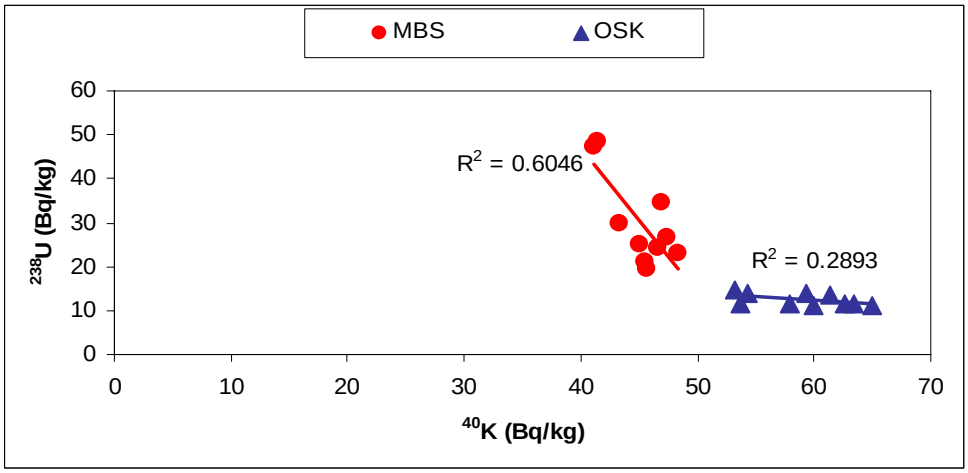

Figure 4.8: Correlations between ^{40}K and ^{238}U in MBS and OSK samples.

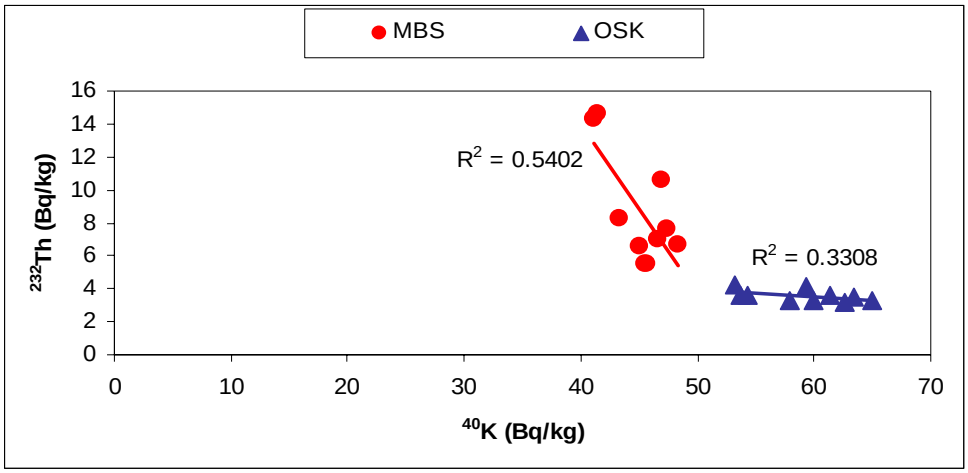

Figure 4.9: Correlations between ^{40}K and ^{232}Th in MBS and OSK samples.

The Salt River enters the sea at the OSK beach and it continuously supplies sediments from the hinterland areas. The analyses of the mean values of potassium content from the MBS and OSK beach indicates that K content vary maximally up to 0.2 %. These values were observed in similar type of beaches along the coast of Brazil (Anjos et al., 2006). The low concentrations of potassium indicate that sediments were derived from the sedimentary strata of the nearby hinterland areas. The hinterland area consists of coastal plains of the Malmesbury Group and the Silurian Table Mountain group (Dingle et al., 1983; Haughton, 1993).

Thorium, uranium and potassium concentrations of granitic rocks are intimately related to its mineral compositions and petrologic features (Rogers and Ragland, 1961; Doventon and Prensky, 1992). According to these authors, thorium, uranium and potassium contents tend to be high in felsic rocks and to increase with alkalinity or acidity. Potassium is usually found in potash feldspars, such as microcline and orthoclase, or in micas, like muscovite and biotite. Rocks that are free of these minerals have very low K-activity. The low K-activity (0.12 to 0.19 %) in the beach sediments shows that, the sand particles are not derived from high grade igneous terrains.

Based on the ratios of Th/K, Th/U and K concentrations, the results suggests, a difference in mineral compositions and the transport processes of beach sediments along the MBS and OSK beach zones. The slightly higher levels of ^{40}K concentrations

in the OSK beach zone are due to the draining of the Salt River which continuously supplies fresh sediments to the beach zone. Also based on the low potassium concentrations in the above sediments, it can be inferred that the sediments are derived from the sedimentary provinces (Dingle, 1989). The beach sediments were possibly derived from Miocene, Pliocene and Quaternary transgressive sediments from the Malmesbury Group, the Cape Super Group and the Silurian sandstones of the Table Mountain Group which occur in close proximity to the West Coast and are the possible source of these mineral sands. The above information shows evidence that sediments were originally derived from sedimentary and meta-sedimentary rocks.

4.4 Radiometric analyses of transect samples

The radiometric results of transect samples for the Melkbosstrand (MBS) and Ouskip (OSK) beach for ^{232}Th, ^{238}U and ^{40}K, together with their weighted mean values and standard deviations are presented in the Table 4.4. The activity concentrations of ^{232}Th in units Bq.kg^{-1} varies from 3.1 ± 0.2 to 7.6 ± 0.3 with a weighted mean and standard deviation (w_i mean ± $w_{i\ STDEV}$) of 4.3 ± 1.9 for the MBS beach; and 3.2 ± 0.2 to 4.0 ± 0.2 with a weighted mean and standard deviation (w_i mean ± $w_{i\ STDEV}$) of 3.4 ± 0.5 for the OSK beach, respectively. The activity concentration of ^{238}U in units Bq.kg^{-1} varies from 9.4 ± 0.9 to 26.7 ± 1.0 with a weighted mean and standard deviation (w_i mean ± $w_{i\ STDEV}$) of 14.8 ± 7.2 for the MBS beach; and 8.9 ± 0.9 to 14.8 ± 1.2 with a weighted mean and standard deviation (w_i mean ± $w_{i\ STDEV}$) of 10.7 ± 2.4 for the OSK beach, respectively. The activity concentration of ^{40}K in units Bq.kg^{-1} varies from 47.39 ± 3.19 to 96.39 ± 7.26 with a weighted mean and standard deviation (w_i mean ± $w_{i\ STDEV}$) of 58.9 ± 20.3 for the MBS beach; and 53.5 ± 4.2 to 87.1 ± 7.9 with a weighted mean and standard deviation (w_i mean ± $w_{i\ STDEV}$) of 61.6 ± 15.6 for the OSK beach, respectively.

The activity concentrations of ^{232}Th and ^{238}U increases, while ^{40}K concentrations decrease from shoreline to the coast, as observed in the MBS and OSK beach samples and shown in Figure 4.10 and 4.11. The result shows that, there is a

distribution of heavy minerals deposition towards the coastline and lighter minerals towards the shorelines in the MBS beach zone. There is a little variation in the radionuclide distributions along the transect profile in the OSK beach, presumably due to the continuous supply of fresh sediments from the Salt River which changes the distribution pattern of sediments. From the analyses of these samples, it may be possible to evaluate the distribution of the radionuclide concentrations as it varies with the distance from the shoreline for each beach. The radiometric analyses also allow evaluating the mean behavior of the natural radionuclide distribution for each beach zone. Both the coastal zones present a radiometric signature with a stable $^{232}Th/^{238}U$ mean value of 0.29 ± 0.02 and 0.30 ± 0.03 for the MBS and OSK beach, respectively. The χ_R^2 value for the ^{232}Th, ^{238}U and ^{40}K concentrations are 48.3, 209.7 and 185.9 for the MBS beach zone and 5.2, 4.6 and 6.1 for the OSK beach samples. The χ_R^2 results, indicates that ^{232}Th and ^{238}U concentrations in MBS beach zone are widely distributed and ^{40}K is less distributed. Some sampling spots have very high ^{232}Th and ^{238}U activity concentrations (e.g. Mbs 3) and some have low (e.g. Mbs 10).

Table 4.4: Radionuclide concentrations of transect samples collected from Melkbosstrand and Ouskip beach.

Sample Code	^{232}Th (Bq.kg^{-1})	^{238}U (Bq.kg^{-1})	^{40}K (Bq.kg^{-1})	Ratio (^{232}Th/^{238}U)
Transect sand samples from Melkbosstrand beach				
Mbs(ts)1	3.1 ± 0.2	9.4 ± 0.9	96.4 ± 7.3	0.33 ± 0.03
Mbs(ts)2	3.5 ± 0.3	11.1 ± 0.7	68.4 ± 5.3	0.32 ± 0.03
Mbs(ts)3	4.2 ± 0.2	14.4 ± 0.8	53.6 ± 4.1	0.29 ± 0.02
Mbs(ts)4	6.1 ± 0.5	21.2 ± 0.9	49.8 ± 3.5	0.29 ± 0.02
Mbs(ts)5	7.6 ± 0.3	26.7 ± 1.0	47.4 ± 3.2	0.28 ± 0.01
w_i mean ± Sd	4.3 ± 1.9	14.8 ± 7.2	58.9 ± 20.3	0.29 ± 0.02
Chi-square	48.3	209.7	185.9	
Transect sand samples from Ouskip beach				
Osk(ts)1	3.3 ± 0.2	9.4 ± 0.9	81.5 ± 6.7	0.34 ± 0.04
Osk(ts)2	2.8 ± 0.2	8.9 ± 0.9	87.1 ± 7.9	0.31 ± 0.04
Osk(ts)3	4.0 ± 0.2	14.8 ± 1.2	56.3 ± 4.5	0.27 ± 0.03
Osk(ts)4	3.8 ± 0.2	11.7 ± 1.2	53.5 ± 4.2	0.33 ± 0.04
Osk(ts)5	3.2 ± 0.2	10.6 ± 0.7	59.2 ± 4.5	0.30 ± 0.03
w_i mean ± Sd	3.36 ± 0.5	10.7 ± 2.4	61.6 ± 15.6	0.30 ± 0.03
Chi-square	5.2	4.6	6.1	

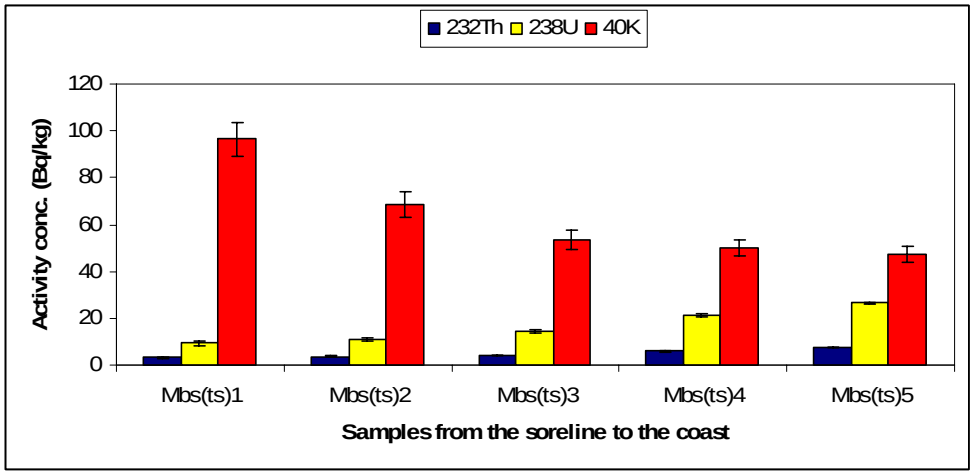

Figure 4.10: Variation of radionuclides along transects to the coastline at MBS beach. Mbs(ts)1 is a sample from closest to shoreline, and the sample Mbs(ts)5 is taken closest to the coastline.

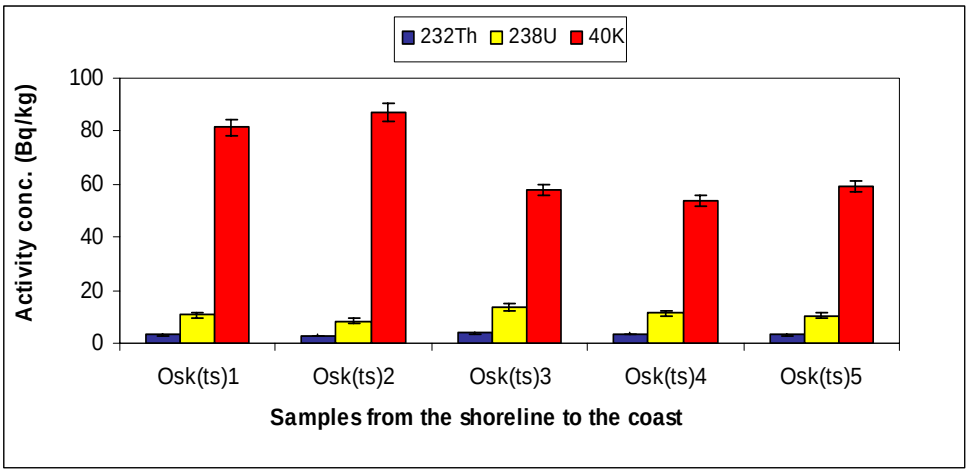

Figure 4.11: Variation of radionuclides along transect to the coastline at OSK beach. Osk(ts)1 is a sample from closest to shoreline, and the sample Osk(ts)5 is taken closest to the coastline..

The shorelines are continuously subjected to tidal wave actions, longshore movement of currents and intense activity of wind. There is strong evidence of sediment transport and possibly lighter minerals are more affected, due to the density and surface area effects than heavy minerals on the shorelines (as opposed to the coast).

4.5 Radiometric analyses of grain-size fractions

The grain-size separation was carried out in order to investigate whether the radiometric technique can be used as an alternative method to provide provenance characteristics of the sand deposits. In this method, the radiometric values for the different grain-size fractions from the MBS and OSK beach sand samples are compared. Two samples from MBS beach (Mbs1 and 3) and one sample from OSK (Osk7) was used for the grain-size analyses.

Grain-size separation was made using a mechanical sieve shaker and different sieve sets, so as to verify the radionuclide concentrations in various grain-size fractions obtained. In the present analyses, only grain-size fractions of 180, 125 and 90 μm were taken for the radiometric measurements. Other grain-size fractions did not yield enough material for radiometric analyses. The results of ^{232}Th and ^{40}K activity concentration for the above samples are presented in Table 4.5 (a, b and c).

Table 4.5a: Radiometric analyses of various grain-size fractions from Mbs1 sample.

Phi (ϕ)	size (μm)	Radiometric values (Bq. kg^{-1}) ^{232}Th	^{40}K
2.5	180	3.0 ± 0.2	43.5 ± 2.2
3.0	125	3.9 ± 0.2	38.9 ± 3.5
3.5	90	72.8 ± 6.1	48.2 ± 9.7

Table 4.5b: Radiometric analyses of various grain-size fractions from Mbs3 sample.

Phi (ϕ)	size (μm)	Radiometric values (Bq. kg^{-1}) ^{232}Th	^{40}K
2.5	180	2.3 ± 0.2	49.1 ± 6.2
3.0	125	4.3 ± 0.7	33.1 ± 2.2
3.5	90	289.1 ± 10.5	45.7 ± 39.5

Table 4.5c: Radiometric analyses of various grain-size fractions from Osk7 sample.

Phi (ϕ)	size (μm)	Radiometric values (Bq. kg^{-1}) ^{232}Th	^{40}K
2.5	180	2.4 ± 0.4	81.2 ± 3.4
3.0	125	2.6 ± 0.2	47.4 ± 3.0
3.5	90	8.1 ± 1.3	48.9 ± 15.0

The result shows that, ^{40}K content varies only slightly with the grain-size, while values of ^{232}Th increases strongly with a decrease in grain-size. This behavior agrees with the same type of study carried out in the Brazilian coast, by Anjos (Anjos et al., 2006). It is also seen that 90 μm fractions shows an order of magnitude larger

^{232}Th concentration, which indicates significant presence of heavy minerals. The heavy mineral fractions in MBS beach shows higher level of thorium content, which may possibly be due to the presence of zircons as it is prominent along the west coast sand (Macdonald et al., 1997). However, there is a large uncertainty in the ^{40}K activity concentration of grain-size fraction 90 μm from MBS sample (Mbs 3) which is due to the high levels of ^{232}Th activity concentration.

4.6 Depositional environment characteristics

Based on the gamma-ray measurements of coastal sand deposits, it is possible to observe a strong relationship between natural radionuclide distribution and the geological evolution of the coastal zone (Anjos et al., 2006). A correlation was found between thorium, uranium and potassium with the provenance and transport mechanism of sediments and its mineral composition.

Since the correlations between Th, U and K are usually given in equivalent ground concentrations, the concentrations of ^{232}Th and ^{238}U were expressed in parts per million and ^{40}K in percents, so that the specific parent activity of a sample containing 1 ppm of ^{232}Th and 1 ppm of natural U is 4.08 Bq/kg and 12.3 Bq/kg, respectively. And for natural potassium, a concentration of 1% by weight of a sample corresponds to a ^{40}K specific activity of 317 Bq/kg (Anjos et al., 2006). Radiometric results for samples (parallel to the shoreline) were plotted in the same manner as shown in Figure 1.1. The cross plot of eTh/eU and eTh/K is presented for the compositional changes related to potassium, as well as implications concerning redox potential, which were derived from the Table 4.3 and shown in Figure 4.12. The potassium-thorium cross plot is widely used for the recognition of clay mineral associations and the discrimination of micas and feldspars in granitic rocks (Macfarlane et al., 1989). As both thorium (by adsorption) and potassium (chemical composition) are associated with clay minerals, the ratio eTh/K express relative potassium enrichment as an indicator of clay-mineral species, as well as a diagnostic of other minerals (Doveton and Prensky, 1992). The horizontal divisions were obtained from the elemental eTh/K ratios, for various mineral associations. The eTh/K ratio varies from 9.23 to 25.01 for the MBS beach and 3.93 to 5.03 for the OSK beach, respectively. The high eTh/K ratio (Figure. 4.12) represents heavy minerals, and signifies that the MBS group of sands has more heavy minerals and less light

particles such as K-bearing feldspars, as compared to OSK samples. One depth sample (Mbs depth) from MBS beach shows much higher eTh/K ratio (605.85). It indicates significant concentrations of heavy minerals present.

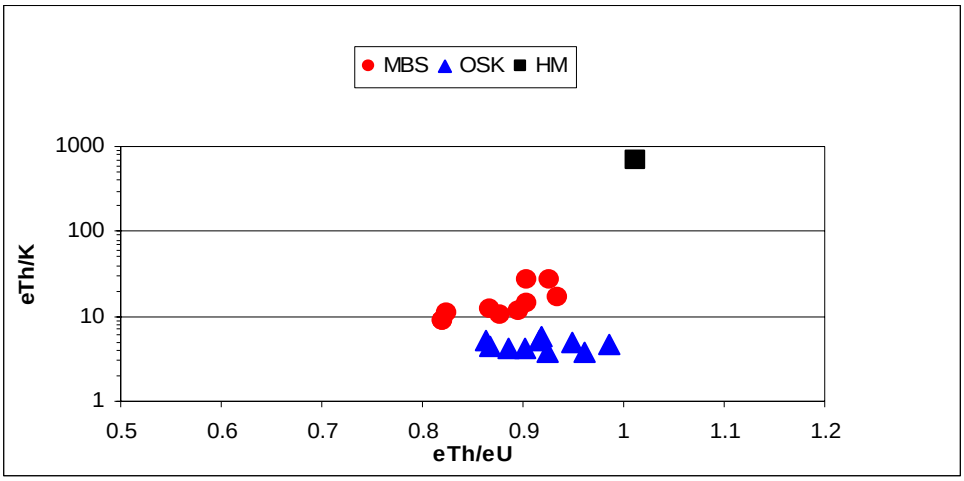

Figure 4.12: Cross plot of eTh/eU vs. eTh/K of sand samples collected from MBS and OSK. The black dot represents a depth sample (Mbs depth), which shows heavy mineral characteristics.

The eTh/eU ratio varies from 0.82 to 0.94 for the MBS beach and 0.87 to 1.0 for the OSK beach, respectively. Based on the eTh/eU ratios and the diagnostic values suggested by Adams and Weaver (Adams and Weaver, 1958), an oxidizing environment is indicated for the MBS and OSK beach samples. These two beach zones are characterized by distinct eTh/eU values that can be associated with differentiated transport of sediments along the coastline of the west coast. The OSK group falls under micas and feldspars, while the MBS group of samples falls under clay mineral groups. A sample from the MBS group (Mbs depth) falls under the heavy mineral group. Based on the cross plot of eTh/eU and eTh/K, the sand samples of MBS and OSK beach were presumably deposited in a fixed uranium environment and an oxidizing environment.

CHAPTER 5

CONCLUSION

This chapter presents the summary and conclusions of this study and a few suggestions are made for the future.

5.1 Summary

A radiometric study of beach sand deposits along the west coast of South Africa was carried out. The samples were collected at the Melkbosstrand (MBS) and the Ouskip (OSK) beaches, parallel to the shoreline, and also some were collected perpendicular to the shoreline. Samples were washed, dried and cooled to room temperature and placed in Marinelli beaker for more than 3 weeks in order to achieve the radioactive secular equilibrium between ^{238}U and ^{232}Th series and their respective progeny. The activity concentrations of radionuclides such as ^{232}Th, ^{238}U and ^{40}K were determined by using a hyper-pure germanium (HPGe) detector.

The Melkbosstrand (MBS) beach samples show higher levels of thorium and uranium concentrations as compared to the Ouskip (OSK) beach samples. The higher levels of ^{232}Th and ^{238}U are present due to the presence of heavy minerals fraction in the MBS beach as compared to the OSK beach. There are higher level of ^{40}K activity concentrations observed in OSK group which shows more enrichment of lighter minerals such as potash feldspars and quartz sands. The Salt River drains on to the OSK beach and draining the area, continuously supplies fresh sediments from the hinterland areas. Based on the low potassium concentrations in both the beach zones, it can be inferred that the sediments were possibly derived from the sedimentary provinces.

Samples collected perpendicular to the shoreline show lateral variation of radionuclides from shorelines to the coast in each beach zone. Thorium and uranium

concentrations are gradually increasing, while the potassium concentration is decreasing from shorelines to the coast. The shorelines are continuously subjected to tidal-wave actions, longshore movement of currents and intense activity of wind. There is strong evidence of sediment transport and possibly lighter minerals are more affected due to the density and surface area effects as compared to heavy minerals.

The radiometric analysis of grain-size fractions shows that, ^{40}K content varies only slightly with the grain-size, while ^{232}Th increases with the decrease in grain-size. Heavy mineral fractions from MBS beach show higher levels of thorium content which may possibly be due to the presence of zircons as it is a prominent radioactive mineral along the west coast. Even though grain-size results were obtained and were interpretable, it was observed to be essential to sieve carefully (to reduce contribution of other grain-sizes to the grain-size of interest). And also, there were higher uncertainties associated with in detection efficiencies for the smaller container than for the Marinelli beaker.

Based on the ^{40}K concentrations in the two beach zones, it can be inferred that the sand particles were derived from the sedimentary provinces. The sedimentary provinces such as Cape Supergroup and the Table Mountain Group, which are occurring close in a proximity to the West Coast, are the possible source of these mineral sands. The above inferences, shows the evidence of sediments originally derived from sedimentary and meta-sedimentary rocks.

Based on the cross plot of eTh/eU and eTh/K, it can be inferred that the sand samples were deposited in a fixed uranium environment and an oxidizing environment, respectively. The OSK group falls under micas and feldspars, while MBS group of samples falls under clay mineral groups. The high Th/K ratio in MBS samples signifies that MBS beach sand samples have more heavy minerals and less lighter particles such as K-bearing feldspars as compared to OSK beach sand samples.

The radiometric technique can be broadly applied to sedimentological studies such as textural, mineralogical, provenance investigations, transport history and depositional environment studies for the beach sediments based on radionuclide activity concentrations such as for ^{232}Th, ^{238}U, ^{40}K and Th/U and Th/K ratios.

5.2 Possible follow-up studies

The radiometric analyses results of beach sands from Western Cape coast (Melkbosstrand and Ouskip beach) proved to be very useful in the investigation of the mineralogy, grain-size distribution, provenance, transport and depositional history of the Western Cape coast. Thus, in future for follow-up studies the following are suggested:

- perform similar studies to this along further stretches of the South African coastline in order to assess variability and reasons for the variation (e.g. Western Cape geology map(see Figure 1.1)),
- perform more depth sampling to assess the variation in the radiometric signatures with depth,
- study seasonal variation in radionuclide concentrations,
- perform chemical analyses of sand samples for further understanding of the geochemistry and relationship with parent rock, and provenance.

APPENDIX A: RADIOACTIVE EQUILIBRIUM

The occurrence of radioactive equilibrium takes place when each radionuclide decays at the same rate it is produced. However, radioactive equilibrium depends on the half-life of the decay product. If the half-life of the daughter radionuclide is much longer than that of the parent radionuclide, the equilibrium does not occur.

Suppose, radionuclide N_1 disintegrates and produces a radioactive decay chain, whereby a nuclide decays into another unstable daughter nuclide N_2 which itself disintegrates to another unstable nuclide and eventually reaches a stable nuclide N_3. The application of the radioactive decay law can describe this system as:

$$\frac{dN_1}{dt} = -\lambda_1 N_1 \tag{1A}$$

$$\frac{dN_2}{dt} = \lambda_1 N_1 - \lambda_2 N_2 \tag{2A}$$

$$\frac{dN_3}{dt} = \lambda_2 N_2 \tag{3A}$$

with initial conditions

$$N_1(t=0) = N_1(0) \tag{4A}$$

$$N_2(t=0) = 0 \tag{5A}$$

$$N_3(t=0) = 0 \tag{6A}$$

Solving these equations leads to the solution,

$$N_1(t) = N_1(0)\exp(-\lambda_1 t) \tag{7A}$$

$$N_2(t) = N_1(0)\left(\frac{\lambda_1}{\lambda_2 - \lambda_1}\right)\left[\exp(-\lambda_1 t) - \exp(-\lambda_2 t)\right] \tag{8A}$$

$$N_3(t) = N_1(0)\left[1 + \left(\frac{\lambda_1}{\lambda_2 - \lambda_1}\right)\exp(-\lambda_2 t) - \left(\frac{\lambda_2}{\lambda_2 - \lambda_1}\right)\exp(-\lambda_1 t)\right] \tag{9A}$$

Because activity $A_i(t) = \lambda N_i(t)$, the activities of the 3 isotopes are given by:

$$A_1(t) = A_1(0)\exp(-\lambda_1 t) \tag{10A}$$

$$A_2(t) = A_2(0)\left(\frac{\lambda_2}{\lambda_2 - \lambda_1}\right)\left[\exp(-\lambda_1 t) - \exp(-\lambda_2 t)\right] \tag{11A}$$

$$A_3(t) = 0 \tag{12A}$$

where λ_1, λ_2 and λ_3 are the corresponding decay constants of a parent and its daughter nuclides, respectively.

From the above equations, secular and transient equilibrium can be achieved depending on the half-life of the parent nuclide and the daughter nuclides in the respective decay chain. Radiometric secular equilibrium is established when the parent nuclide has a half-life much longer than any of the daughter nuclides in the decay series. And sufficiently long period of time must have elapsed to allow the in-growth of the decay product. The activity of the daughter nuclide "grows in" to reach the activity of the parent nuclide and both activities will be equal and decrease at the same rate. The criterion for secular equilibrium is $\frac{\lambda_a}{\lambda_b} \leq\sim 10^{-4}$, i.e. $\lambda_b >> \lambda_a$, where λ_a, λ_b are decay constants of parent and daughter nuclides (L'Annunziata, 1998).

For example, one sample with ERL code S06-itl-inh-ts-0035 was measured with the HPGe detector at iThemba LABS. Eight measurements were performed every after three days starting immediately after sealing. The measuring time varied between 48,097s and 235,487s. The ^{238}U gamma-ray lines used for activity calculation were 295 keV and 352 keV from ^{214}Pb, 1120 keV and 2204 keV from ^{214}Bi together with 1001 keV from ^{234m}Pa.

For justification of results obtained experimentally, the equation

$$\frac{\lambda_b N_b}{\lambda_a N_a} = \frac{\lambda_b}{\lambda_b - \lambda_a}\left\{1 - \exp\left[-(\lambda_b - \lambda_a)t\right]\right\} \tag{13A}$$

was used for modelling using the Excel Software package see Figure 3A. Figure 1A indicates that the concentrations of radon daughters (^{214}Pb and ^{214}Bi) increase with time until it becomes equal at the 19th day.

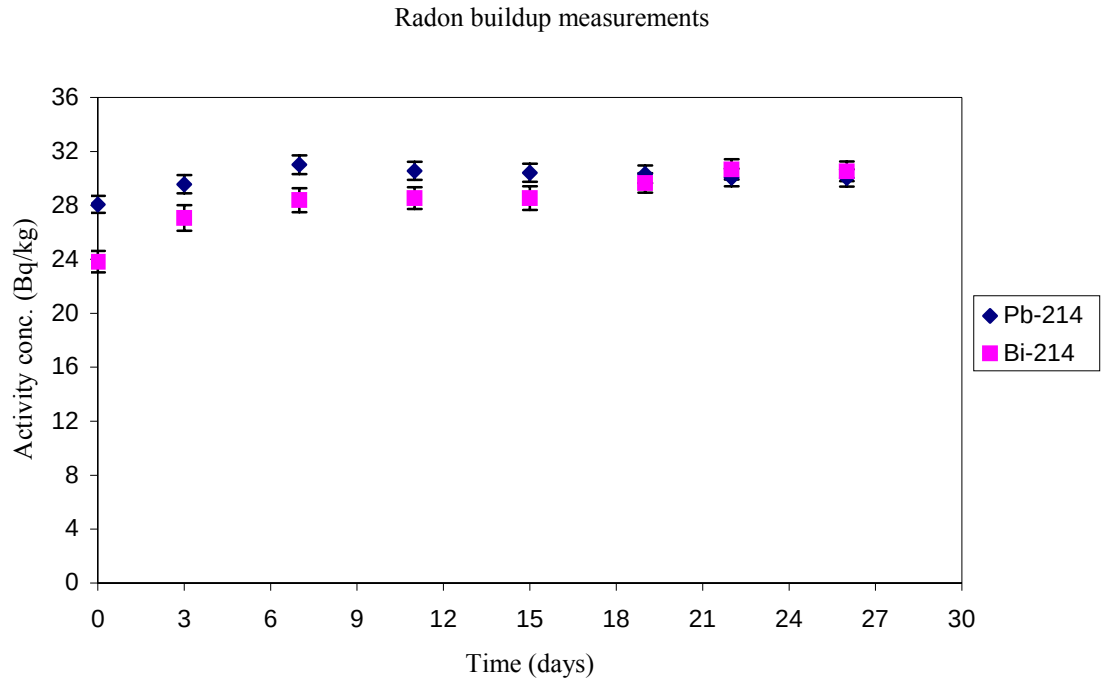

Figure 1A: In-growth of radon daughters (^{214}Pb and ^{214}Bi).

From the decay products of ^{238}U, ^{234m}Pa has a short half-life of 1.17m, and thus it ensures radiometric secular equilibrium in a few minutes after the sealing of the sample. The activity concentration of this nuclide is expected to be constant as time changes. However, this nuclide has small gamma-ray branching ratio (emission probability) of 0.0884 and thus the uncertainty in its activity concentration is relatively large.

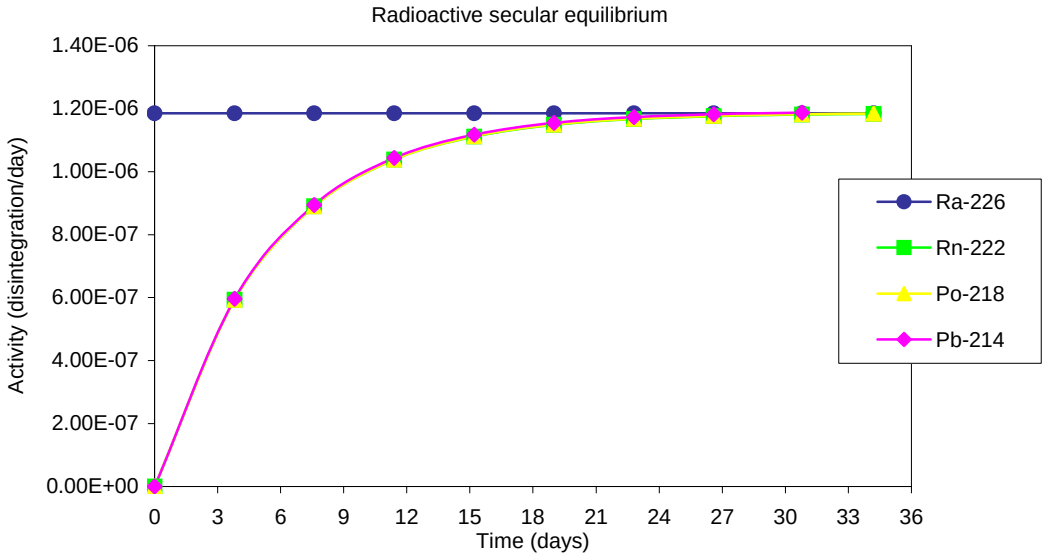

Figure 2A: Secular equilibrium modelling for a parent ^{226}Ra and its daughters.

APPENDIX B: STATISTICAL FORMULAE

B-1.1: Mean

The arithmetic mean value $\bar{x}$ of a sample of n measured responses x_i *(i = 1,2,...n)* is given by;

$$\bar{x} = \frac{1}{n}\sum_{i=1}^{n} x_1 \qquad (1B)$$

and for only one measurement made, the arithmetic mean is obviously that value. The arithmetic mean can also be given as the weighted mean:

$$\bar{x} = \left(\frac{\sum_{i=1}^{n} w_i x_i}{\sum_{i=1}^{n} w_i} \right) \qquad (2B)$$

where w_i is the weighting factor.

B- 1.2: Variance and Standard deviation

The variance S^2 of a sample of measurements x_i *(i = 1,2,...n)* is the sum of the square of the differences of between the measurements and their mean $\bar{x}$, divided by $n - 1$. This can be symbolically represented as:

$$s^2(x) = \frac{1}{n-1}\sum_{i=1}^{n} (x_i - \bar{x})^2 \qquad (3B)$$

The standard deviation is described as the degree of deviation of fluctuation of the data set about the mean, and it is very useful descriptor of a statistical data set. It is mathematically defined as the square root of the variance; that is:

$$s = \sqrt{s^2} \qquad (4B)$$

For a set of values x_i each which has an associated variance s_i^2 and if these variances are not equal, the weighted mean defined in (1B) is a better estimate for

variance then the arithmetic mean. The weighted factor w_i, to be assigned to each measurement is given by $w_i = \frac{1}{s_i^2}$.

The operation of a counting system can be tested by comparing the distribution of a series of results from repeated measurements with the expected distribution. One measure of performance is the reduced chi-square statistic, χ_R^2 (Chi-square per degree of freedom). The chi-square per degree of freedom is the measure of a goodness of fit to the data, and it is given by;

$$\chi_R^2 = \frac{1}{n-1} \frac{\sum_{i=1}^{n} (x_i - \bar{x})^2}{(\Delta x_i)^2} \qquad (5B)$$

where n is the number of data points Δx_i is the uncertainty in the each value of measurement.

B-2: Useful formulas for calculation the uncertainties

Table 2B: Table showing the algebraic expressions used to calculate the uncertainty ΔX, derived from (Knoll, 1979).

Equation from which results *X* is to be calculated	**Formula for calculating the uncertainty ΔX**
$X = AB$ or $X = \frac{A}{B}$	$\Delta X = X\sqrt{\left(\frac{\Delta A}{A}\right)^2 + \left(\frac{\Delta B}{B}\right)^2}$
$X = A \pm B$	$\Delta X = \sqrt{(\Delta A)^2 + (\Delta B)^2}$
$X = A^n$ where n is a constant	$\frac{\Delta X}{X} = n\frac{\Delta A}{A}$
$X = kA + B$ or $X = kA - B$ where k is a constant	$\Delta X = \sqrt{(k\Delta A)^2 + (\Delta B)^2}$
$X = kAB$ or $X = k\frac{A}{B}$ where k is a constant	$\frac{\Delta X}{X} = \sqrt{\left(\frac{\Delta A}{A}\right)^2 + \left(\frac{\Delta B}{B}\right)^2}$
$X = \frac{A \times B}{C \times D}$	$\frac{\Delta X}{X} = \sqrt{\left(\frac{\Delta A}{A}\right)^2 + \left(\frac{\Delta B}{B}\right)^2 + \left(\frac{\Delta C}{C}\right)^2 + \left(\frac{\Delta D}{D}\right)^2}$

REFERENCES

Adams, J.A.S., and Weaver, C.E., (1958). *Thorium to uranium ratios as indications of sedimentary processes: Example of concept of geochemical facies*: American Association of Petroleum Geologists Bulletin, V. 42, 387-430.

Alencar, A.S and Freitas A.C., (2005). *Reference levels of natural radioactivity for the beach sands in a Brazilian southeastern coastal region*. Radiation Measurements, 40, 76-83.

Asadov, A., Krofceck, D., and Gregory, M., (2001). *Applications of γ-ray spectrometry to the study of grain size distribution of beach and river sands*. Marine Geology, 179, 203-211.

Anjos, R.M., Veiga, R., Macario, K., Carvalho, C., Sanches, N., Bastos, J. and Gomes, P.R.S., (2006). *Radiometric analysis of Quaternary deposits from the southern Brazilian coast*. Marine Geology, 229, 29 - 43.

Broquet, C.A.M., 1992. *The sedimentary record of the Cape Supergroup:* A review. In: de Wit, M.J., Ransome, I.G.D. (Eds.), Inversion Tectonics of the Cape Fold Belts, Karoo and Cretaceous Basins of Southern Africa. A.A. Balkema, Rotterdam, pp. 159-183.

Coetzee, C.B., (1957). *Ilmeniethoudende sand langs die Weskus in die Distrik Vanrhynsdrop*. Bulletin of Geological Survey of South Africa, 25, 17.

Croft, S., Hutchinson, I.G., (1999). *The measurement of U, Th and K concentrations in building material*. Applied Radiation an Isotopes. 51, 483-492

De Beer, C.H., (1992). *Structural evolution of the Cape Fold Belt syntaxes and its influence on syntectonic sedimentation in the SW Karoo Basin*. In: de Wit, M.J., Ransome, I.G. D. (Eds.), Inversion tectonics of the Cape Fold Belt, karoo and Cretaceous Basins of the South Africa. A.A. Balkema, Rotterdam, pp. 197-206.

De Meijer, R.J., Lesscher, H.M.E., Schuiling, R.D., and Elburg, M.E., (1990). *Estimates of heavy mineral content in sand and its provenance by radiometric methods*. Nuclear Geophysics, 4, 455-460.

De Meijer, R.J., and Donoghue, J.F., (1995). *Radiometric Fingerprinting of Sediments on the Dutch, German and Danish Coast*. Quaternary International, 26, 43-47.

De Meijer, R.J., Stapel, C., Jones, D.G., Roberts, P.D., Rozendaal, A. and Macdonald, W.G. (1997). *Improved and new uses of natural radioactivity in mineral exploration and processing*. Exploration and Mining Geology, 6, 105-117.

De Meijer, R.J., (1998). *Heavy minerals from Eldelstein to Einstein*. Journal of Geochemical Exploration, 62, 81-103.

De Meijer, R.J., Jams, I.R., Jennings, P.J. and Koyers, J.E., (2001). *Cluster analysis of radionuclide concentrations in beach sand*. Applied Radiation and Isotopes, 54, 535-542.

De Swardt, A.M.J., Roswell, D.M., 1974. *Note of the relationship between diagenesis and deformation in the Cape Fold Belt. Transactions of the Geological Society of South Africa* 77, 239-245.

Dingle, R.V., Siesser, W.G. and Newton, A.R., (1983). *Mesozoic and Tertiary geology of Southern Africa*. Balkema, Rotterdam, 375 pp.

Doveton, J.H., Prensky, S.E., (1992). *Geology Applications of Wireline Logs*: a Synopsis of Developments and Trends The Log Analyst, 33, 286-303.

Firestone, R.B., (1996). *Table of isotopes, eighth edition*. (Ed. Shirley V.S) John Wiley & sons, New York.

Gehreke, R.J., Davidson, J.R., (2005). *Acquisition of quality γ-ray spectra with HPGe spectrometers*. Applied Radiation and Isotopes, 62, 479-499.

Gilmore, G., Hemingway, J.D., (1995). *Practical Gamma-ray Spectrometry*. John Wiley & Son Ltd, Chichester, New York, Brisbane, Toronto, Singapore.

Haughton, S.H., (1931). *The late Tertiary and Recent deposits of the west coast of South Africa*. Transactions of the Geological Society of South Africa, 34, 19-58.

Hendriks, P.H.G.M., Limburg, J., de Meijer, R.J., (2001). *Full-spectrum analyses of natural gamma-ray spectra*. Journal of Environmental Radioactivity, 53, 365-380.

Jones, D.G., (2001). *Development and application of marine gamma-ray measurements: a review*. Journal of Environmental Radioactivity, Vol. 53, 3, 313-333.

Kannan, V., Rajan, M.P., Iyenger, M.A.R., Ramesh, R., (2002). *Distribution of natural and anthropogenic radionuclides in soil and beach sand samples of Kalpakkam (India) using hyper pure germanium (HPGe) gamma ray spectrometry*. Appl. Radiat. Isot. 57, 109-119.

Knoll, G.F., (1979). *Radiation detection and measurement*. John Wiley & Sons Inc, New York USA.

Knoll, G.F., (1989). *Radiation detection and measurement. (Second edition)*. John Wiley & Sons Inc, New York USA.

Kogan, R.M., Nazarov, L.M., Fridman, S. D., (1969). *Gamma spectrometry of natural environments and formations*. Moskva Atomizdat, Moscow, 337 pp.

Komar, P.D., (1989). *Physical processes of waves and currents and the formation of marine placers*. Aquatic Science, 1, 393-423.

Krane, K.S., (1988). *Introductory Nuclear Physics*. John Wiley & Son Inc, New York USA.

L'Annunziata, M.F., (1998). *Handbook of RADIOACTIVITY ANALYSIS*. International Atomic Energy Agency.

Leo, W.R., (1987). *Techniques fro Nuclear and Particle Physics Experiments*. Springer-Verlag Berlin Heidelberg.

Lilley, J., (2001). *Nuclear Physics Principles and Applications*. John Wiley & Son Ltd, England.

Macdonald, P.D. and Rozendaal, A., (1995). *The Geelwal Karoo heavy beach sand deposit: a modern day heavy mineral placer*. Journal of African Earth Sciences, 21, 1, 187-200.

Macdonald, P.D., Rozendaal, A and De Meijer, R.J., (1997)., *Radiometric characteristics of heavy mineral deposits along the West Coast of South Africa*. Mineralium Deposita, 32, 371-381.

Macfarlane P. A., Whittemore D.O., Townsend M.A., Doveton J.H., Hamilton V. J., Coyle III, W.G., Wade A., Macpherson G.L. and Black R.D., (1989). *The Dakota Aquifer Program Annual Report, FY89*. Appendix B. Kansas Geological Survey, Open-File Report. 90-27. http://www.kgs.ukans.edu/Dakota/vol3/fy89/index.htm

Maleka, P.P., (2001). *Calibration of germanium detectors for applications of radiometric methods in South Africa*. M.Sc thesis, unpublished, University of the Western Cape.

Maphoto, K.P., (2004). *Determination of Natural Radioactivity Concentrations is Soil: a comparison study of windows and Full Spectrum Analyses*. M.Sc thesis, unpublished, University of the Western Cape.

Modisane, T.J., (2005). *Correlations between Natural Radionuclide Concentration in Soils and Vine-growth Potential*. M.Sc thesis, unpublished, North West University, Mafikeng.

Mohanty, A.K., Sengupta, D., Das, S.K., Vijayan, V., Saha, S.K., (2004*). Natural radioactivity in newly discovered high background radiation area on the east coast of Orissa, India*. Radiation Measurements. 38, 153-165.

Nicholas, T., (1983). *Measurement and Detection of Radiation*. McGRAW-HILL BOOK CAMPANY.

Oak Ridge Associated universities, Marinelli (ca 1950), Donated by Ron Katherin, www.orau.org/ptp/collection/Miscellaneouse/marinelli.htm, (1999).

Radhakrishna, A.P., Somashekarappa, H.M., Narayana, Y., Siddappa, K., 1993. *A new natural background radiation area on the southwest coast of India*. Health Phys. 65, 390-395.

Lapp, Ralph, E., and Andrews., Howard, L., (1972). *Nuclear Radiation Physics*. Fourth edition, Prentice-Hall Inc, Englewood Cliffs, New Jersey.

Ramos-Lerate, I., Barrera, M., Ligero, R.A., Casaa-Ruiz, M., (1997). *A new summing-correction method for gamma-efficiency calibration with multi-gamma-ray radionuclides*. Nuclear Instruments and Methods in Physics Research A, 395,202-206.

Rozendaal, A., and Scheeper, R., (1995). Magnetic and related mineral deposits of the Pan-African Saldania belt in the Western Cape Province, South Africa. Journal of African Earth Sciences, 21,107-126.

Sharshar, T., Elnimr, T., El-HUSSEINY, F.A., EL-ABD, A., (1997). *Efficiency Calibration of HPGe Detector for Volume-source Geometries*. Applied Radiation and Isotopes, 48, 695-697.

Theron, J.N., (1992). *The geology of the Cape Town area*. Kopiereg voorbehou.

Toerien, D.K. and Groeneveld, D., (1957). Ilmeniethoudende sand langs die weskus in die distrik Vanrhynsdorp. Bulletin of Geological Survey of South Africa, 25, 17.

Tsoulfanidis, N.T., (1983). *Measurement and Detection of Radiation*. McGRAW-HILL BOOK CAMPANY.

Tykva, R., Sabol, J., (1995). *Low Level Environmental Radioactivity Sources and Evaluation*. Technomic Publishing Company, Lancaster, Pennsylvania.

(Ge-USR) *Germanium Detectors*, User's Manual, Copyright 1998, Canberra Industries.

(IAEA) International Atomic Energy Agency, Analytical Quality Control Services, Reference Sheet, Reference Material IAEA-375, radionuclides and trace elements, (2000).

(Oxf97) Oxford Instruments Inc, Instructional Manual, Third Generation Personal Computer Analyser, PPC 300F010197, USA, (1997).

(Www01) www.nuclides.net/applets/about_radioactive_decay.htm.